OPTICAL SIGNAL PROCESSING FOR MANIPULATING AND CHARACTERIZING TIME-FREQUENCY ENTANGLED PHOTONS

A Dissertation

Submitted to the Faculty

of

Purdue University

by

Ogaga D. Odele

In Partial Fulfillment of the

Requirements for the Degree

of

Doctor of Philosophy

May 2018

Purdue University

West Lafayette, Indiana

This dissertation is dedicated to the memory of my father,

William I. K. Odele

(1949–2011).

ACKNOWLEDGMENTS

The Advisory Committee

First and foremost, I would like to express my utmost gratitude to Prof. Andrew M. Weiner for the opportunity to study under his tutelage. Prof. Weiner has been a role model and even in some ways, a father figure to me over the last five years—I owe my research accomplishments to him and I hope to continue to make him proud beyond life at Purdue. I am also thankful to Prof. Daniel Elliott, Prof. Peter Bermel and Prof. Zubin Jacob for serving on my doctoral committee and providing me with constructive feedback at different points during my studies.

The Ultrafast Optics Team

Dr. Daniel Leaird was invaluable over the course of our research as he supported the lab with his technical expertise. Dr. Joseph Lukens introduced me to the field of quantum optics; his mentorship, exceptional communication skills and attention to detail helped in my development as a researcher. Dr. Jose Jaramillo-Villegas, Poolad Imany and Hsuan-Hao (Peach) Lu were fabulous collaborators and friends, with whom I had some of the most intellectually stimulating conversations. Other (previous and current) members of the lab, including Dr. Xiaoxiao Xue, Dr. Amir Rashidinejad, Dr. Andrew Metcalf, Bohao Liu, Oscar Sandoval, Navin Lingaraju, Mohammed Al Alshaykh, and Keith McKinzie, also contributed to an enjoyable academic experience.

Stanford Collaborators

Thanks to Dr. Carsten Langrock and Prof. Martin Fejer for their contributions as research collaborators.

Family and Friends

To my mother, Bessie Odele, thank you for supporting my dreams, and for your prayers, encouragement and unconditional love. Also, many thanks to my siblings: Faith, Richmond, Raymond, Priye, Efe, Tega, Coker, Oshare and Nikari. Lastly, my sincerest thanks go to several families and mentors who have assisted me in numerous ways, and friends whose support for me never depended on my success as an individual: The Adeola, Anokwute, Ayewah, Ladapo, Ogbe, and Oji families, Prof. Krishna Madhavan, Prof. Ebenezer Gnanamanickam, Prof. Cordelia Brown, Prof. Caleb Brooks, Angela Rainwater, Obehi Ukpebor, GiJey Gilliam, Ibhade Eigbobo, Othniel Usifo, Chukwuneku Ekeruche, Jarrad Crutcher, Jayla Wheeler, Kenneth Idem, Mark Pengitore, Olivia Smith, Jeff Wojcicki, Jonathan Bernhard, Oby Omenogor, Eugene Anane, Sayan Roy, Zurum Okereke, Chibuzor Ezeamaku and Olumide Awofeso.

TABLE OF CONTENTS

Page

LIST OF FIGURES

Figure Page

Figure Page

ABBREVIATIONS

AWG	arbitrary waveform generator
CFBG	chirped fiber Bragg grating
CW	continuous-wave
FTM	frequency-to-time mapping
FWHM	full-width at half-maximum
M-sequence	maximal length sequence
OSA	optical spectrum analyzer
PM	phase modulator
PPLN	periodically poled lithium niobate
QPM	quasi-phase-matched
SFG	sum-frequency generation
SHG	second-harmonic generation
SMF	single-mode fiber
SPAD	single-photon avalanche diode
SPDC	spontaneous parametric downconversion

ABSTRACT

Odele, Ogaga D. Ph.D., Purdue University, May 2018. Optical Signal Processing for Manipulating and Characterizing Time-Frequency Entangled Photons. Major Professor: Andrew M. Weiner.

Time-frequency entangled photons ("biphotons") exhibit joint spectral and temporal correlations that are unattainable with classical light. Besides being deployed for tests of quantum nonlocality, these photonic states are desirable for a unique range of applications that can significantly impact communications and computation. In this dissertation, we describe novel schemes based on spectral and temporal domain processing for manipulating and characterizing broadband biphotons. Implementing frequency-dependent filters, first, we present and demonstrate a technique for controlling the relative delay between a pair of entangled photons, relying on pump frequency tuning and the quantum concept of nonlocal dispersion cancellation. Next, we demonstrate near-field frequency-to-time mapping, a technique adopted from classical photonics, for arbitrary control of biphoton temporal correlations. Subsequently, we generate temporal correlation trains by creating biphoton frequency combs through programmable spectral amplitude shaping and demonstrate the temporal Talbot effect with entangled photons for the first time. Moreover, in the absence of fast single-photon detectors, we show how electro-optic phase modulation (originally a time-dependent operation) can be used to examine the coherence of biphoton frequency combs. Lastly, we introduce a scheme based on electro-optic intensity modulation, another time-domain operation, for improving the resolution in biphoton temporal correlation measurements. Overall, our body of work could provide additional insight into the manipulation and characterization of biphoton states, as well as contribute towards the improvement of quantum technologies.

1. INTRODUCTION

Richard Feynman once said that "The word 'quantum' refers to this peculiar aspect of nature that goes against common sense." At its onset, the establishment of a means to explain several phenomena that were incompatible with the wave and particle picture of light and matter, respectively, would fuel the development of quantum theory. Some notable successes over the 20th century include Einstein's explanation of the photoelectric effect, understanding the motion of electrons around a nucleus, photon statistics, and experimental tests of nonlocal realism. Today, the study of quantum science is motivated not only by a quest for understanding nature's "weirdness" but also by a set of unprecedented technologies: quantum computation could provide an avenue for solving some computationally hard problems [1, 2], quantum communication could allow the secure transfer of quantum states/information [3–5], and quantum metrology could enable the highest precision allowable in measurements [6, 7].

While there are several physical systems in contention for advancing quantum technologies, light is appealing because of its transmission speed and ability to maintain coherence over long distances [8]. In this regard, there has been interest in controlling quantum states of light, such as single photons and entangled photon-pairs. More specifically, entangled photons can exhibit nonclassical correlations in various degrees of freedom—for example, polarization, spatial, spectral and temporal. With respect to the spectral and temporal degrees of freedom, in recent times, there has been tremendous progress in developing optical signal processing techniques for manipulating time-frequency entangled photons (or "biphotons"). Control schemes enabled by the use of dispersive media [9–12], Fourier-transform pulse shapers [13–19], electro-optic modulators [20–24] have been demonstrated, and have even inspired new protocols for quantum information processing [25–28].

In this dissertation, we will present newly developed optical signal processing techniques—hinged on spectro-temporal amplitude and phase control—for characterizing and manipulating biphotons in ways that can contribute to the advancement of quantum technologies. In the next section, we will provide a brief theory on time-frequency entangled photons while describing our source, and show how spectral- and temporal- amplitude and phase manipulations transform the biphoton wavepacket. Then the remainder of this document will be structured as follows: in Chapter 2, we will discuss our work on delay control between a pair of entangled photons; in Chapter 3, we will present our experiments on near-field frequency-to-time mapping for arbitrary shaping of biphoton temporal correlations; in Chapter 4, we will introduce programmable spectral filtering with spatial light modulators for generating biphoton correlation trains, allowing us subsequently to implement the first verification of the temporal Talbot effect using entangled photons; in Chapter 5, we will describe a phase-modulation scheme which we developed to examine the coherence of biphoton frequency combs; in Chapter 6, we will discuss an approach with intensity modulators for improving the resolution of temporal correlation measurements using standard single-photon detectors; and in Chapter 7, we will present a summary of the accomplished work.

1.1 Time-Frequency Entangled Photons

Time-frequency entangled photon pairs exhibit strong correlations in both the spectral and temporal degrees of freedom. While biphotons can be generated in a variety of materials and structures, we will only concern ourselves with type-0 (degenerate, collinear, same polarization) spontaneous parametric downconversion (SPDC) of a continuous-wave (CW) laser, where a single frequency pump photon (at $\omega_{\mathrm{p}} = 2\omega_0$) decays into two *daughter* photons (the biphoton)—usually one is referred

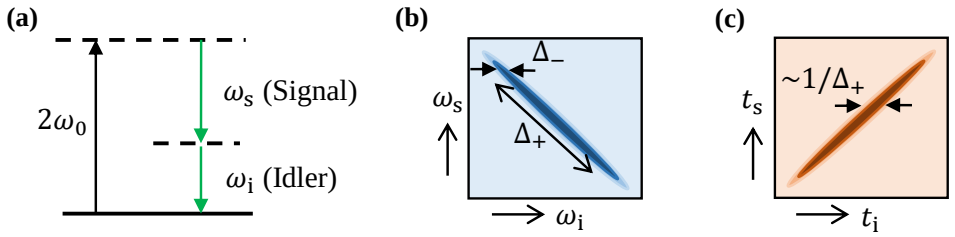

Fig. 1.1. Time-Frequency Entangled Photons. (a) Illustration of Spontaneous Parametric Down Conversion. (b) Spectral anticorrelation of biphoton; Δ_- and Δ_+ denote the pump linewidth and biphoton bandwidth, respectively (c) Temporal correlation of biphoton.

to as the signal photon, and the other as the idler photon [Fig. 1.1(a)]. The generated biphoton state can be written as [29, 30]

$$|\Psi\rangle = M|\text{vac}\rangle_\text{s}|\text{vac}\rangle_\text{i} + \int_{-\omega_0}^{\omega_0} d\Omega\, \phi(\Omega)\, |\omega_0 + \Omega\rangle_\text{s}\, |\omega_0 - \Omega\rangle_\text{i} \tag{1.1}$$

where the signal-idler photons are in a joint superposition of continuous frequency modes—the frequencies of each mode pair sum up to the pump frequency to satisfy conservation of energy—and weighted by the biphoton spectral amplitude, $\phi(\Omega)$, which depends on the phasematching properties of the crystal. In Eq. 1.1, $M \approx 1$, denoting almost unity probability for unsuccessful conversion of the pump photon into signal and idler photons, and ω_0 is the center frequency, half the frequency of the pump. Therefore, if the frequency of a photon in the signal mode is measured, the frequency of the photon in the idler mode will be known—in practice, the idler mode will be known within a deviation given by the pump linewidth [Fig. 1.1(b)].

In addition to frequency correlation, the birth of signal and idler photons occurs at approximately the same time, and this can be observed through an intensity cross-correlation measurement for single photons. Following the seminal approach of Glauber [31], the probability that one photon is recorded at time t and another photon at time t' is formally described by

$$G^{(2)}(t, t') = |\langle \text{vac}|\hat{E}_\text{i}^{(+)}(t)\hat{E}_\text{s}^{(+)}(t')|\Psi\rangle|^2 \tag{1.2}$$

It is also useful to define an effective biphoton wavepacket (or wavefunction) [29], $\psi(\tau)$, such that $G^{(2)}(t,t') = |\psi(t,t')|^2$, which implies that

$$\psi(t,t') = \langle \text{vac}|\hat{E}_{\text{i}}^{(+)}(t)\hat{E}_{\text{s}}^{(+)}(t')|\Psi\rangle \tag{1.3}$$

In Eqs. 1.2 and 1.3, $\hat{E}_{\text{s}}^{(+)}(t')$ and $\hat{E}_{\text{i}}^{(+)}(t)$ are the positive electric field operators associated with the absorption or annihilation of a signal photon at time t' and its partner idler photon at time t, respectively, and they are represented as follows:

$$\hat{E}_{\text{s}}^{(+)}(t') = \int_0^\infty d\omega_{\text{s}}\, \hat{a}_{\text{s}}(\omega_{\text{s}})\, e^{-i\omega_{\text{s}}t'} \tag{1.4}$$

$$\hat{E}_{\text{i}}^{(+)}(t) = \int_0^\infty d\omega_{\text{i}}\, \hat{a}_{\text{i}}(\omega_{\text{i}})\, e^{-i\omega_{\text{i}}t} \tag{1.5}$$

where we have omitted constants and slow (square root) functions of ω [29, 31]. The terms, $\hat{a}_{\text{s}}(\omega_{\text{s}})$ and $\hat{a}_{\text{i}}(\omega_{\text{i}})$, are annihilation operators for destroying a signal photon at frequency ω_{s} and an idler photon at frequency ω_{i}, respectively; for a single photon at frequency ω, the annihilation operator satisfies the form:

$$\hat{a}(\omega)|\omega'\rangle = \delta(\omega - \omega')|\text{vac}\rangle \tag{1.6}$$

Therefore, using the biphoton state in Eq. 1.1 along with Eqs. 1.3–1.6, and taking $t' = t + \tau$, the resulting biphoton wavepacket can be expressed as:

$$\psi(t, t+\tau) = \int_{-\omega_0}^{\omega_0} d\Omega \int_0^\infty d\omega_{\text{i}} \int_0^\infty d\omega_{\text{s}}\, \phi(\Omega)\, \delta(\omega_s - \omega_0 - \Omega)\, \delta(\omega_i - \omega_0 + \Omega)\, e^{-i[(\omega_s+\omega_{\text{i}})t + \omega_{\text{s}}\tau]} \tag{1.7}$$

Eq. 1.7 can be simplified further using the fundamental property of the delta function: the integral under ω_s is nontrivial only when $\omega_{\text{s}} = \omega_0 + \Omega$, and the integral under ω_{i} is nontrivial only when $\omega_{\text{i}} = \omega_0 - \Omega$. Hence the biphoton wavepacket becomes

$$\psi(t, t+\tau) = e^{-i\omega_0(2t+\tau)} \int_{-\infty}^{\infty} d\Omega\, \phi(\Omega)\, e^{-i\Omega\tau} \tag{1.8}$$

This shows that if the arrival time of the signal photon is measured, the arrival time of the idler photon can be predicted correctly up to a precision that is proportional to

the square-modulus of the *Fourier* transform of the biphoton spectral amplitude—see illustration in Fig. 1.1(c).

A general schematic of the setup we use for generating entangled photons is depicted in Fig. 1.2(a). We couple a CW pump into a periodically poled lithium niobate (PPLN) waveguide [32, 33] to generate degenerate biphotons centered around 1550 nm—the efficiency of the conversion process is $\sim 10^{-5}$. (The waveguides we use in all of our experiments come from our collaborations with Prof. Martin Fejer's group at Stanford University—see Appendix.) Unconverted pump photons are removed with a series of colored glass filters, and using a collimator, we couple the generated biphotons into fiber, after which we can apply spectral and/or temporal operations to the signal and idler photons. Figure 1.2(b) is a typical spectrum of the biphoton we obtained using an optical spectrum analyzer at a resolution of 250 GHz. Since the photon pairs are collinear and have the same polarization, we are left with two options to separate them. The first option is to distinguish them by frequency, whereby we define the signal mode to have frequencies greater than the center frequency (ω_0) and the idler to have frequencies less than ω_0. The other option is to use a 50/50 beamsplitter, such that 50% of the time, the signal and idler photons exit in different output ports. In the experiments discussed throughout this dissertation, we ensure

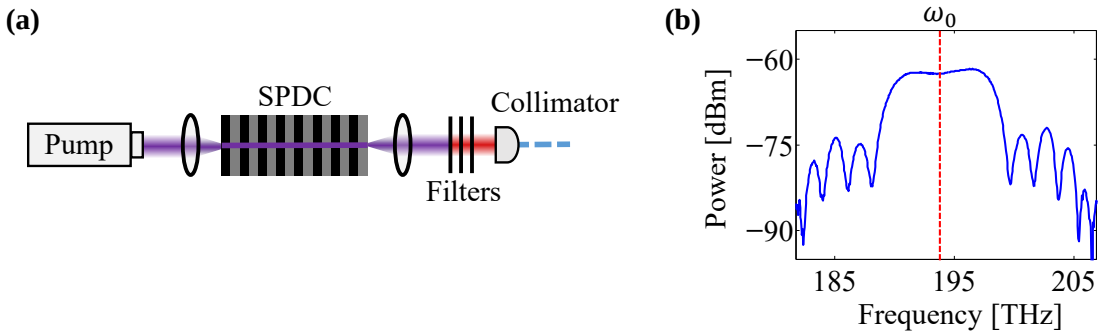

Fig. 1.2. (a) General schematic for generating biphotons. (b) Measured spectrum of the biphotons with center frequency around 193.5 THz (1550 nm) and bandwidth $\sim$ 5 THz (40 nm).

to specify the option chosen for distinguishing between the pairs of photons. Now we will set up some expressions that describe the implications of applying spectral and temporal operations to the biphoton.

1.2 Spectral domain manipulation of biphotons

Applying linear, time-invariant spectral filters, $H_{\mathrm{s}}(\omega_s)$ to the signal mode and $H_{\mathrm{i}}(\omega_i)$ to the idler mode, transforms the field operators in Eqs. 1.4 and 1.5 as

$$\hat{E}_{\mathrm{s}}^{(+)}(t+\tau) = \int_0^\infty d\omega_{\mathrm{s}}\, H_{\mathrm{s}}(\omega_s)\, \hat{a}_{\mathrm{s}}(\omega_{\mathrm{s}})\, e^{-i\omega_{\mathrm{s}}(t+\tau)} \tag{1.9}$$

$$\hat{E}_{\mathrm{i}}^{(+)}(t) = \int_0^\infty d\omega_{\mathrm{i}}\, H_{\mathrm{i}}(\omega_i)\, \hat{a}_{\mathrm{i}}(\omega_{\mathrm{i}})\, e^{-i\omega_{\mathrm{i}}t} \tag{1.10}$$

Now, the effect of spectral filtering on the biphoton wavepacket can be seen by using Eqs. 1.9 and 1.10 to evaluate Eq. 1.3. This will yield the following expression:

$$\psi(t, t+\tau) = e^{-i\omega_0(2t+\tau)} \int_{-\infty}^\infty d\Omega\, \phi(\Omega)\, H_{\mathrm{s}}(\omega_0+\Omega)\, H_{\mathrm{i}}(\omega_0-\Omega)\, e^{-i\Omega\tau} \tag{1.11}$$

which shows that the filters applied to the signal and idler photons are multiplied at complimentary frequencies. The consequence of this multiplication will become apparent in Chapters 2, 3 and 4.

1.3 Temporal domain manipulation of biphotons

The application of time-domain modulation functions, $m_{\mathrm{s}}(t)$ to the signal photon and $m_{\mathrm{i}}(t)$ to the idler photons, transforms the field-operators as

$$\hat{E}_{\mathrm{s}}^{(+)}(t+\tau) = m_{\mathrm{s}}(t+\tau) \int_0^\infty d\omega_{\mathrm{s}}\, \hat{a}_{\mathrm{s}}(\omega_{\mathrm{s}})\, e^{-i\omega_{\mathrm{s}}(t+\tau)} \tag{1.12}$$

$$\hat{E}_{\mathrm{i}}^{(+)}(t) = m_{\mathrm{i}}(t) \int_0^\infty d\omega_{\mathrm{i}}\, \hat{a}_{\mathrm{i}}(\omega_{\mathrm{i}})\, e^{-i\omega_{\mathrm{i}}t} \tag{1.13}$$

By inserting Eqs. 1.12 and 1.13 into Eq. 1.3, we can evaluate the biphoton wavepacket after time-domain modulation to be

$$\psi(t, t+\tau) = m_{\mathrm{s}}(t+\tau)\, m_{\mathrm{i}}(t)\, \psi_0(t, t+\tau) \tag{1.14}$$

where $\psi_0(t, t+\tau)$ is the biphoton wavepacket before modulation (Eq. 1.8). Here we see that temporal correlation $G^{(2)}(t, t+\tau) = |\psi(t, t+\tau)|^2$ can be shaped if the amplitude of the modulation function varies as a function of time; this forms the basis for our work in Chapter 6. However, if the modulation functions consist of only temporal phase, $G^{(2)}(t, t+\tau)$ is incapable of revealing any features from the phase modulation. Still the effect of phase modulation can be observed in the frequency domain, as will be discussed in Chapter 5.

2. TUNABLE DELAY CONTROL OF ENTANGLED PHOTONS BASED ON DISPERSION CANCELLATION

2.1 Background

The spectral and temporal correlations of entangled photons are desirable in a wide range of applications. For example, large-alphabet quantum key distribution based on arrival-time measurements of entangled photons has been proposed and demonstrated in multiple configurations [25,26,36,37]. And the tendency of biphotons to be detected in coincidence—even though individual arrival times are random—has been used directly to synchronize distant clocks with high precision [6, 38, 39]. However, the availability of reconfigurable optical delay lines would enhance complete control over timing measurements using entangled photons.

High-speed delay switching schemes have already received significant attention in the scene of classical photonics [40, 41]. In its most basic form, delay control can be realized by varying the optical path length traversed by the field through the system. Unfortunately, the switching speed of this approach is limited to the ∼kHz range by the mechanical motion of a delay stage or mirror. Alternatively, drastically faster modulation is possible through a setup using wavelength conversion followed by dispersion [42]. Since different frequencies propagate at distinct group velocities through a dispersive medium, the amount of wavelength shift applied to the input field (either through electro-optic modulation or nonlinear mixing) maps directly to the delay of the output; thus, by tuning the frequency shift, it is possible to modulate the applied delay, in some cases with GHz switching speeds [40]. Nevertheless, this delay comes at a price: dispersion not only shifts the arrival time, but also causes the pulse to spread. Therefore compensation is typically achieved by propagating through

The results of this chapter have been published in Refs. [34] and [35].

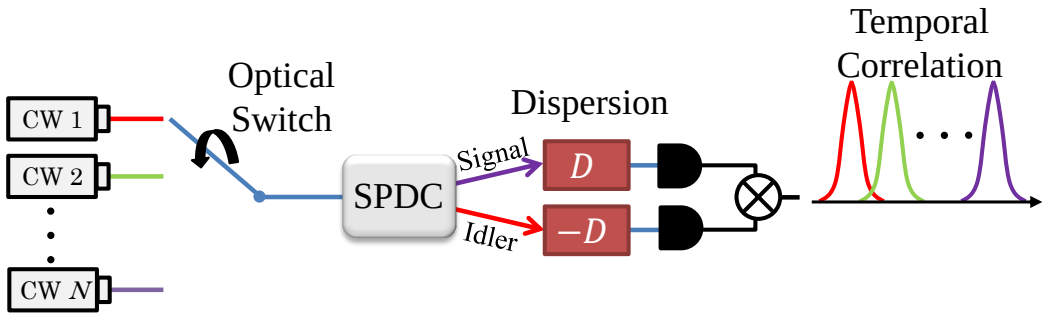

Fig. 2.1. General scheme for delay control of time-frequency entangled photons through pump frequency tuning and propagation in dispersive media. The signal and idler photons, generated through spontaneous parametric downconversion (SPDC), propagate in separate media with opposite signs of dispersion (D) to achieve nonlocal dispersion cancellation. Subsequently, frequency tuning of the pump—depicted as switching between multiple continuous-wave (CW) lasers—leads to shift in the delay between signal and idler photons.

equal and opposite group velocity dispersion before shifting the original wavelength or after shifting the output wavelength back to its original value [42–44].

Building on these classical systems, we propose and demonstrate tunable delay control of nonclassical time-frequency entangled photons for the first time, through pump-frequency detuning and propagating the generated biphotons through optical dispersion. In related past experiments [10, 11], the frequency-dependent group delay of dispersive fiber was combined with spectral filtering to modify the arrival time of heralded single photons. Yet such passive filtering not only eliminates large fractions of the photon flux but, by reducing the total bandwidth, also lengthens the bandlimited correlation time, an undesirable consequence especially relevant to experiments resolving ultrafast correlations. Here we instead consider pump-frequency modulation, a previously underutilized degree of freedom in biphoton manipulation experiments offering the potential advantages of rapid delay tuning and the ability to shift the delay of nearly the full biphoton spectrum. Temporal spreading is minimized in our proposed scheme by exploiting nonlocal dispersion cancellation—an

effect whereby applying equal and opposite dispersion to the signal and idler photons leaves the biphoton correlation function unaltered [18, 45–47]. This allows us to compensate for the broadening which would otherwise degrade the sharpness of the temporal correlations. A schematic for this tunable delay control is shown in Fig. 2.1. We note that this new method for entangled photon control represents a quantum-optical analogue of classical pulse-position modulation.

2.2 Theory

Nonlocal Cancellation of Dispersion

A dispersive medium imparts frequency-dependent phase on photons propagating through it. Mathematically, this can be represented by a spectral filter function,

$$H(\omega) = e^{i\alpha(\omega)} \tag{2.1}$$

where $\alpha(\omega)$ can further be expanded as $\alpha(\omega) = \alpha(\omega_0) + \frac{\partial\alpha}{\partial\omega}(\omega-\omega_0) + \frac{\partial^2\alpha}{\partial\omega^2}(\omega-\omega_0)^2 + ...$ The consequence of introducing such spectral phase terms to Eq. (1.11) is broadening of the temporal correlation [9]. However, if spectral filters H_s and H_i are pure-phase and antisymmetric with respect to each other, dispersion cancellation (net zero spectral phase) can be achieved [18, 45]. Hence, if we consider only second-order dispersion to the biphotons by setting $H_\mathrm{s}(\omega) = \exp[iA_\mathrm{s}(\omega-\omega_0)^2/2]$ and $H_\mathrm{i}(\omega) = \exp[iA_\mathrm{i}(\omega-\omega_0)^2/2]$, then there will be spectral phase cancellation $[H_\mathrm{s}(\omega_0+\Omega)H_\mathrm{i}(\omega_0-\Omega) = 1]$ when $A_\mathrm{s} = -A_\mathrm{i} = A$. In this case, the wavepacket in Eq. (1.11) can now be written as

$$\psi(\tau) \propto \int d\Omega\, \phi(\Omega) e^{-i\Omega\tau} \tag{2.2}$$

as if the biphoton never experienced any dispersion.

Tunable Delay Control

As examined in [18], opposite signs of dispersion give cancellation only for even spectral phase orders; for odd orders, opposite signs add cumulatively. This implies

an important distinction between delay (first-order spectral phase) and second-order dispersion, for if we detune the center frequency of the biphotons relative to the quadratic dispersion by $\delta\omega$ such that $\omega_0' = \omega_0 + \delta\omega$ is the new center frequency, the fixed filters H_s and H_i now introduce additional phase terms linear in frequency, which because of the opposite signs of the coefficients ($A_\mathrm{s} = -A_\mathrm{i}$), *add* rather than cancel. Specifically, $H_\mathrm{s}(\omega_0' + \Omega)H_\mathrm{i}(\omega_0' - \Omega) = \exp(i2A\Omega\delta\omega)$ and the resulting biphoton wavepacket is of the form

$$\psi(\tau) \propto \int d\Omega\, \phi(\Omega) e^{-i\Omega(\tau - 2A\delta\omega)} \tag{2.3}$$

By the time-shift Fourier transform property, the phase term $\exp(i2A\Omega\delta\omega)$ corresponds to a temporal delay of $2A\delta\omega$, directly proportional to both the strength of the dispersion and magnitude of the frequency tuning. In this way the delays imparted by the signal and idler dispersive media are retained, while the associated wavepacket spreading is removed, a fortuitous situation made possible by the spectral anticorrelation of the entangled state. Such a finding indicates that by shifting the pump laser frequency, one can modulate the relative arrival times of entangled photons with minimal impact on the shape of their correlation. In contrast to tunable optical delay lines requiring mechanical adjustment, the filters here are fixed, so that our scheme could in principle be implemented rapidly by simply switching between pump lasers along a fixed frequency grid.

2.3 Experimental Demonstration

Our experimental work is divided into three parts: ps-scale delay control, ns-scale delay control, and high-speed delay switching between entangled photon pairs.

2.3.1 ps-scale Delay Control

We first demonstrate delay control in the range of a few ps, using the experimental setup depicted in Fig. 2.2. Biphotons generated through spontaneous parametric

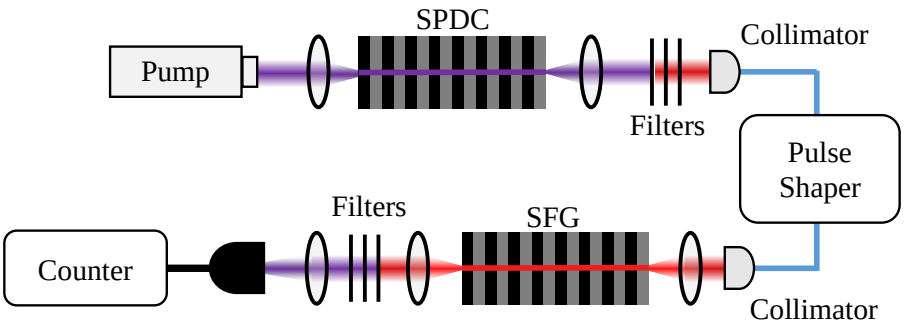

Fig. 2.2. Experimental setup. Pump photons decay into signal and idler photons in a periodically poled lithium niobate (PPLN) waveguide. The pulse shaper is used to apply antisymmetric dispersion to the filtered signal and idler photons, and then they recombine in another PPLN waveguide through sum-frequency generation (SFG). The coincidence rate is measured using a single-photon counter while the delay steps are determined by applying linear spectral phase on the pulse shaper.

downconversion (SPDC) of a pump around 775 nm are fiber-coupled into a programmable pulse shaper [48] (Finisar WaveShaper 1000S), where the antisymmetric quadratic spectral phase, i.e., dispersion, is applied to the biphoton spectrum. Here we define the signal (idler) photon as having frequency greater (less) than one-half that of the pump (as discussed in Section 1.1). The pulse shaper here gives us access to the biphoton spectrum in the frequency range from 191.250 to 196.275 THz ($\sim$ 5 THz bandwidth) with a specified resolution of 10 GHz. It also applies additional phase to compensate for the dispersion from the optical fibers connecting the collimators to the pulse shaper. Another PPLN waveguide, the phase-matching peak of which is aligned with the first waveguide through temperature control, is then used to perform sum-frequency generation (SFG) on the spectrally shaped biphotons. Unlike correlation measurements with a pair of single-photon detectors, SFG permits direct measurement of the temporal correlations with a single detector and on an ultrafast timescale [13, 14], necessary to resolve the picosecond delay shifts in this experiment. After filtering out the unconverted biphotons, we detect the SFG photons

on a silicon single-photon avalanche diode (PicoQuant τ-SPAD). The second-order correlation function $G^{(2)}(\tau) = |\psi(\tau)|^2$ can then be measured by sweeping additional linear spectral-phase terms (equivalent to delay in time) on the pulse shaper and recording the SFG rate at each step [13, 18]. Since we send both photons through the same fiber and recombine them via SFG for detection, this proof-of-concept experiment is in some sense "local," rather than an example of truly nonlocal dispersion cancellation. However, whereas background-free classical analogues of dispersion cancellation [49] *require* local nonlinear detection to realize the effect, in our case we use SFG only as a *tool* to achieve the necessary subpicosecond timing resolution. The proposed concept applies just as well to truly nonlocal systems such as the schematic in Fig. 2.1, and we will realize this in Section 2.3.2.

In the proposed arrangement above, we assume fixed dispersion and a tunable pump laser; this is most compatible with previous classical approaches and rapid switching capabilities. Yet the basic physics is based only on modulation of the *relative* frequency spacing between the dispersion and the SPDC center frequency, so in our first demonstration, the dispersion profile on the pulse shaper is shifted relative to a fixed pump frequency, as shown in Fig. 2.3(a). In this case, we do not require a nonlinear medium phase-matched for SPDC at multiple pump wavelengths, and so we can employ a PPLN waveguide with a uniform poling pattern to give maximum efficiency, generating biphotons with a center wavelength of 1547.20 nm (193.9 THz). Figure 2.3(b) shows the phase-matching curve of such PPLN waveguide (measured second-harmonic-generation conversion efficiency as a function of pump frequency and normalized to the input power [32]). From this measurement, we glean that pump wavelengths in a narrow band around 773.6 nm should be phase-matched for parametric downconversion. We mention, though, that the bandwidth of the generated biphotons—i.e., the spectral width of $\phi(\Omega)$ [Fig. 1.2(b)]—is much wider than that of the curve in Fig. 2.3(b), since the signal and idler fields need not have the same frequency, only a fixed sum. Accordingly, an accurate classical measure of the SPDC bandwidth is instead that of difference-frequency mixing [33].

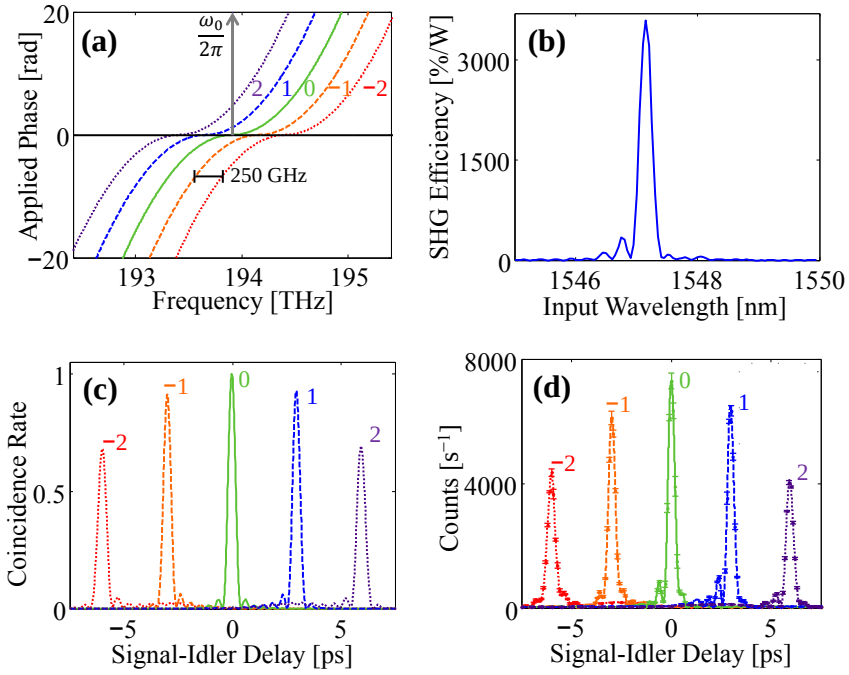

Fig. 2.3. Experiments with fixed pump. (a) Schematic of a fixed pump with shifts in the antisymmetric dispersion curve displayed over 3 THz of the 5 THz pulse shaper window. (b) Phase-matching curve for PPLN waveguide with a uniform poling pattern. (c) Theoretical and (d) experimental results showing delay control of the biphoton correlation function. The numbers [−2 −1 0 1 2] correspond to the amount the dispersion curve is shifted in each case, in units of 250 GHz.

Setting the dispersion constant at $A = 3/\pi$ ps^2 and the center of the antisymmetric quadratic dispersion curve (zero-crossing) at 193.9 THz, we measure a single correlation peak around zero delay as expected for perfect dispersion cancellation [peak labeled "0" in Fig. 2.3(d)]. Subsequently, when we move the center of the antisymmetric curve by integer multiples of 250 GHz, we obtain the results shown in Fig. 2.3(d)—temporal delays of −6, −3, 3, and 6 ps are measured for −500, −250, 250, and 500 GHz shifts in the center of the antisymmetric curve, respectively. Our experimental results [Fig. 2.3(d)] are in excellent agreement with theory [Fig. 2.3(c)]. We point out that the reduction in the peak number of counts for our delayed correlations

is a consequence of designating our signal and idler photons by frequency. Thus, when we shift the antisymmetric dispersion, there is a portion of the biphoton spectrum (in a $2\delta\omega$-wide bandwidth) where the signal and idler photons both experience the same sign of dispersion. The result of this uncompensated dispersion is evident in tails that develop in the shifted correlations, particularly visible in the two exterior curves in Figs. 2.3(c) and 2.3(d). Nonetheless, the displaced peaks themselves show minimal temporal spreading, confirming our ability to shift and compensate nearly the entire biphoton. Moreover, we emphasize that these nonidealities stem only from the nature of the entangled photons here, which can only be distinguished by frequency, and is not inherent to the method itself. For example, in situations where it is possible to spatially separate signal and idler for all pump frequencies (e.g., in noncollinear or type-II downconversion), one could ensure that the entire spectrum of each photon sees the desired dispersion, giving perfect cancellation—in terms of both width and shape—at all delay shifts.

We now move on to our main technique for biphoton tunable delay: by tuning the pump frequency relative to a fixed antisymmetric dispersion profile. PPLN waveguides with uniform quasi-phase-matched (QPM) patterns offer exceptionally high conversion efficiency but, for lengths of several centimeters, accept only a small range of pump wavelengths ($\sim$0.1 nm) for phase-matched down-conversion. So in order to permit a series of discrete pump frequencies with wider separations, we utilize a QPM grating with a phase-modulated poling pattern designed to give roughly equal down-conversion efficiency and bandwidth at five distinct pump wavelengths [50]. Figure 2.4(b) shows the measured SHG phase-matching curve of such grating, suggesting comparable down-converted power at each frequency. Therefore, we replace the uniformly poled lithium niobate waveguides in our setup, for both SPDC and SFG, with ones that have such a modulated poling pattern. Our pump wavelength is set to 774 nm (193.8 THz), corresponding to the middle peak of the phase-matching curve, in order to generate biphotons with a center wavelength at 1548 nm, and we position the center of the antisymmetric quadratic dispersion to match this wavelength with

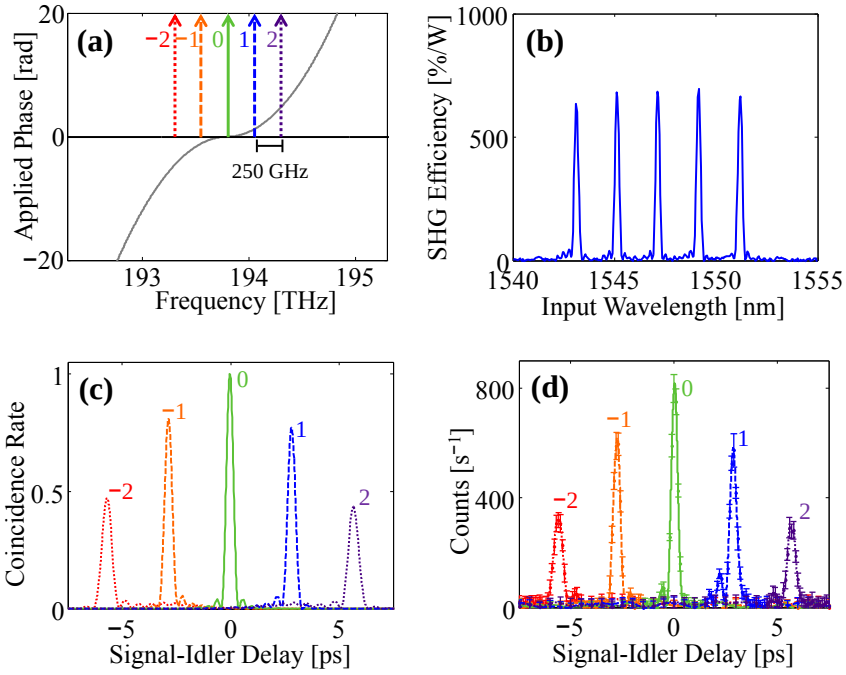

Fig. 2.4. Experiments with fixed dispersion. (a) Schematic of a fixed anti-symmetric dispersion curve with shifts in pump frequency displayed over 3 THz of the 5 THz pulse shaper window. (b) Phase-matching curve for PPLN waveguide with a non-uniform poling pattern. (c) Theoretical and (d) experimental results showing delay control of the biphoton correlation function. The numbers [−2 −1 0 1 2] correspond to the amount the center frequency of the biphoton is shifted in each case, in units of 250 GHz.

$A = 3/\pi$ ps^2. As anticipated, there is a sharp correlation peak at zero delay due to dispersion cancellation [Fig. 2.4(d)]. Detuning the wavelength of our laser by 2, 1, −1, and −2 nm—giving rise to −500, −250, 250, and 500 GHz shifts in the biphoton center frequency—we are able to measure correlation functions with single peaks around −6, −3, 3, and 6 ps, respectively, as shown in Fig. 2.4(d). Again, our experimental results [Fig. 2.4(d)] are in very good agreement with theory [Fig. 2.4(c)]. The total count rate is reduced by a factor of about 10 compared to the results of Fig. 2.3(d) due to the reduced efficiency of the phase-modulated waveguides. We also note that there is an additional drop in the relative peak amplitude for our delayed

correlations in this demonstration compared to the first. Recall that our pulse shaper can only access frequencies between 191.250 and 196.725 THz and hence, as we move the center frequency of the biphotons, we decrease the fraction of the biphoton spectrum transmitted through the pulse shaper—an effect also included in simulation to obtain Fig. 2.4(c). This explains the additional reduction in the delayed coincidence counts, over and above that caused by biphotons that experience the same sign of dispersion (mentioned earlier).

An ideal delay line should have a capacity for high-speed switching over a wide range of delays. Next, we will show that delay tuning can be achieved over a much longer range by using dispersive elements possessing significantly larger values of the constant A, and implement a high-speed biphoton delay switch.

2.3.2 ns-scale Delay Control

Here we target much longer delays which are resolvable even with high-jitter single-photon detectors, thus allowing for truly nonlocal measurements, unlike the delays in the previous experiment that were limited to a few picoseconds and relied on a local detection scheme to measure the correlation function. Using chirped fiber Bragg gratings (CFBGs) to supply the dispersion in our experiment, we can produce a delay range spanning several tens of nanoseconds, five orders of magnitude longer than the initial biphoton correlation width and two orders of magnitude beyond the jitter-limited temporal resolution. Additionally, we report the largest observed spreading-to-despreading factor for a stretched and compressed biphoton temporal correlation time (> 100).

The general framework of this experiment is presented in Fig. 2.5. A pump beam—either from a single tunable CW laser or a wavelength switch between two CW lasers operating around 1550 nm—is coupled into a 67-mm-long QPM lithium niobate waveguide for frequency doubling. Again, we make use of a QPM grating with continuous phase modulated poling to yield roughly equal up-conversion at five dis-

tinct bands. Unconverted pump photons are filtered out and the frequency-doubled beam is coupled into another QPM waveguide for SPDC, producing entangled photons with a center frequency equal to that of the pump laser. The phase-matching peaks of the first waveguide are spectrally aligned with those of the second waveguide through temperature control. After filtering the residual frequency-doubled beam, the biphotons are coupled into optical fiber and then separated into two arms with a 50/50 beamsplitter; 50% of the time, the photons will exit along different paths and can contribute to coincident arrivals. (As mentioned previously, such postselection could be avoided, e.g., with a type-II or noncollinear source; our delay method applies equally well to any spectrally entangled source, regardless of preparation.)

One of the output arms of the beamsplitter is linked to CFBG 1 with a dispersion parameter of +2 ns/nm ($A = 2580$ ps^2), while the other output arm is connected to

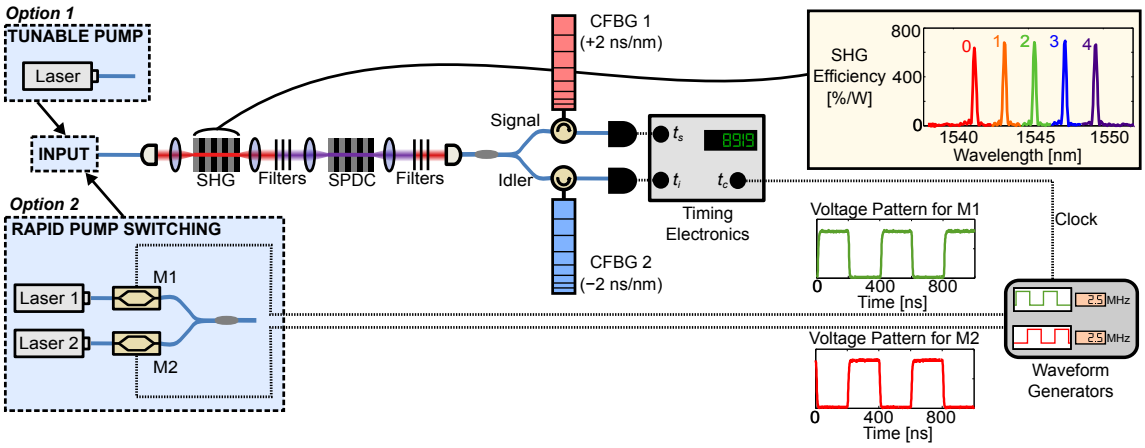

Fig. 2.5. Experimental setup. Boxes at the input show two types of pump sources—a single tunable CW laser and a rapid wavelength switch (two lasers with intensity modulators, M1 and M2, driven synchronously). The input beam is first upconverted in the second-harmonic-generation (SHG) waveguide and then down-converted in the SPDC waveguide. The chirped fiber Bragg gratings (CFBGs) apply dispersion to the separated signal and idler photons, which are measured by a pair of single-photon detectors. The timing electronics tag the arrival time of each photon, as well as the clock signal from the waveform generators.

CFBG 2 with a dispersion parameter of -2 ns/nm ($A = -2580$ ps^2); each CFBG has a loss of only 3 dB, compared to the 24 dB expected from an SMF-28e fiber link with the same dispersion. In addition to their large dispersion, these CFBGs also have a 40-nm-wide acceptance bandwidth that matches the 1530-1570 nm lightwave C-band. A pair of internally triggered gated InGaAs single-photon detectors (Aurea SPD_AT_M2) and time-tagging electronics (PicoQuant HydraHarp 400) are then used to retrieve the arrival-time correlations of the biphotons. We note that since these CFBGs are factory components designed to mimic (CFBG 1) and exactly cancel (CFBG 2) 120 km of SMF-28e, they intentionally impart higher-order phase terms: CFBG 1 introduces a cubic phase coefficient of -16.3 ps^3 and CFBG 2 of 15.4 ps^3. Because opposite signs of cubic phase add rather than cancel for spectrally anticorrelated photons [18], these high-order terms introduce slight distortion in the measured correlation functions below. We emphasize this distortion would be removed entirely by custom-built CFBGs contributing only second-order phase.

To begin, we show the extent to which we can spread and compress the biphoton temporal correlation. Our pump here is a single tunable CW laser (*Option 1* in Fig. 2.5) with wavelength set to 1541 nm. Figure 2.6(a) shows the resulting coincidence

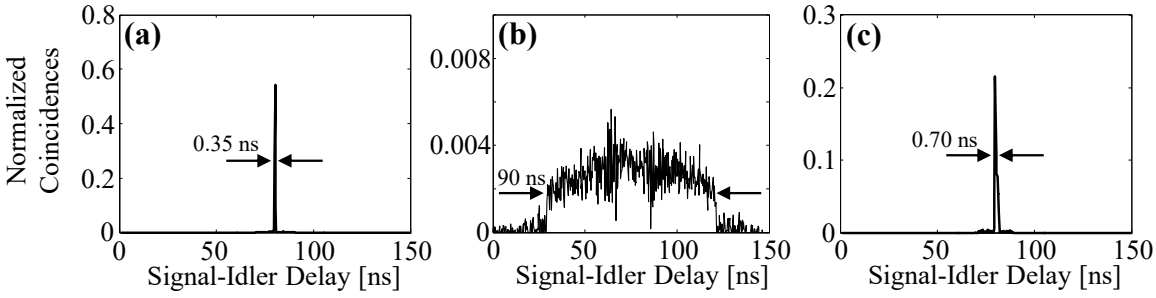

Fig. 2.6. Spreading, compression of biphoton coincidences. Measured temporal correlation (a) before applying dispersion, (b) with positive dispersion applied to signal and idler, (c) with positive dispersion on signal and negative on idler.

peak directly after the 50/50 splitter (after subtracting the background accidentals) with a detector-jitter-limited full-width at half-maximum (FWHM) of 350 ps; a bin size of 256 ps was used for the plot, and we normalize such that the sum over all bins adds up to 1. To see the effect of dispersion, we place CFBG 1 in the path of the entangled photons before splitting them into separate arms and detecting them—this is equivalent to sending the signal and idler photons through separate CFBGs with equal dispersion. Since the CFBG cuts off the 1541-nm-centered biphoton at 1530 nm, only signal and idler photons within 1530-1552 nm (a 22 nm bandwidth) contribute to coincidence counts. The broadened correlation is given in Fig. 2.6(b), showing biphoton wavepacket spreading up to 90 ns. However, when we send the signal photons through CFBG 1 and the idler photons through CFBG 2, we are able to observe nonlocal dispersion cancellation as evidenced by Fig. 2.6(c). A FWHM of 700 ps is measured for the compressed correlation peak, limited by the residual cubic dispersion of the CFBGs. Our spreading-to-despreading factor of 129 is the largest ever observed for *nonlocal* detection of dispersion cancellation, completely eclipsing the single-digit factors in previous examples [26, 46].

Next, keeping the configuration for nonlocal dispersion cancellation, we show the range of reconfigurable signal-idler delays attainable with this setup. Using the phase-

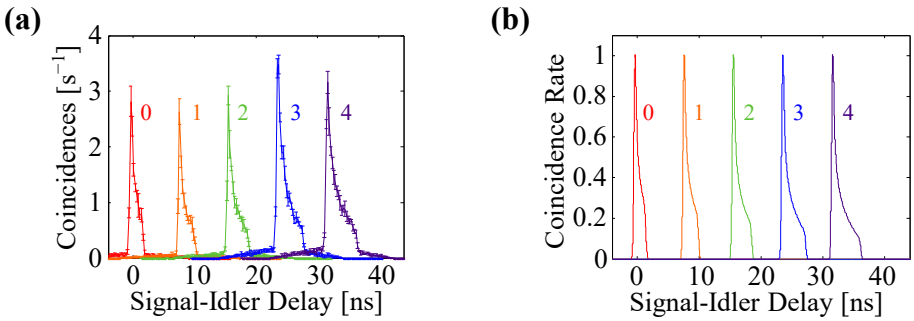

Fig. 2.7. Delay tuning of biphoton coincidences. (a) Experimental and (b) Theoretical correlation functions corresponding to the pump wavelength detuned by $\{0, 1, 2, 3, 4\} \times (-250$ GHz).

matching curve (shown in Fig. 2.5) as a guide, we tune the pump wavelength from 1541 nm to {1543, 1545, 1547, 1549} nm for shifts of $\{-250, -500, -750, -1000\}$ GHz in the biphoton center frequency. The coincidence patterns are given in Fig. 2.7, showing temporal shifts of $\{0, 8, 16, 24, 32\}$ ns; the error bars represent the standard deviation over five acquisitions. Excellent agreement can be seen between our experimental results [Fig. 2.7(a)] and the theoretical predictions [Fig. 2.7(b)]. The correlation peaks broaden as the center wavelength approaches 1550 nm due to a combination of the cubic dispersion and transmission response of our CFBGs (both effects were accounted for in the numerical simulations). The closer the biphoton center wavelength is to 1550 nm, the larger the biphoton bandwidth transmitted through the CFBG, which yields a more pronounced effect of the uncompensated cubic spectral phase on the temporal correlation.

2.3.3 High-Speed Delay Switching

Lastly, we demonstrate rapid delay modulation of different signal-idler delay combinations by implementing a wavelength switch which consists of two electro-optic intensity modulators (EOSpace) and two tunable CW lasers operating at distinct wavelengths—*Option 2* in Fig. 2.5. The modulators are driven with a pair of synchronized waveform generators, both outputting 50%-duty-cycle square pulses with a period of 400 ns (2.5 MHz frequency), but one phase-shifted from the other by half a period, as shown in Fig. 2.5; when M1 is high, M2 is low, and vice versa. The detectors are again triggered by an independent 1.25 MHz clock which, because of its asynchronicity with these modulation patterns, allows the detectors to evenly sample the full switching period. In addition to tagging the signal and idler arrival times, we also record the clock signal from the wavelength switch, enabling us to experimentally corroborate the pump wavelength responsible for each coincidence event.

The result for modulating the pump wavelength between 1547 nm and 1549 nm is presented in Fig. 2.8(a)—we plot photon coincidences as a function of both signal-

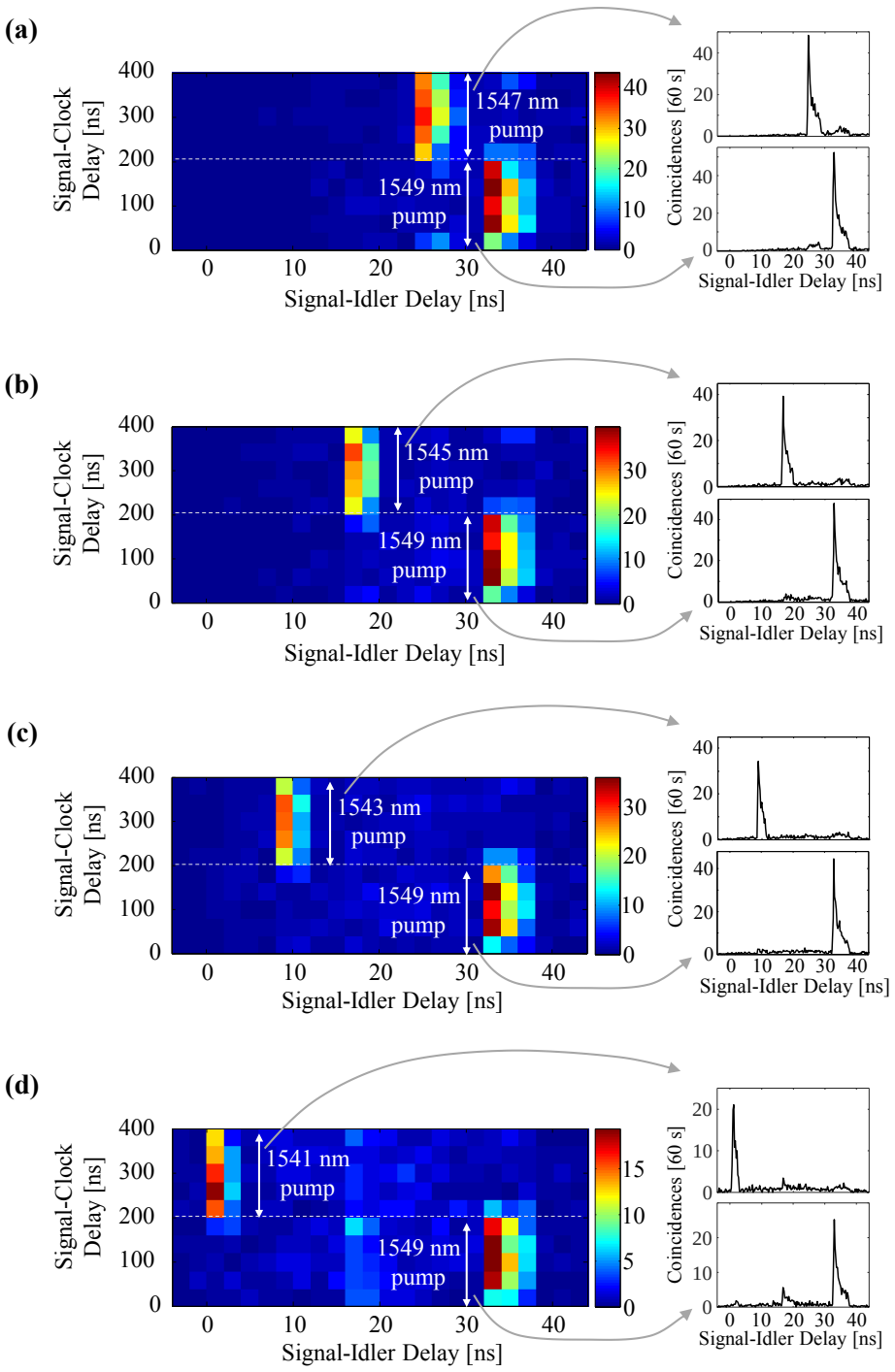

Fig. 2.8. Rapid delay modulation results with coincidences plotted as a function of signal-idler delay (horizontal axis) and signal-clock delay (vertical axis). Modulation of pump wavelengths between (a) 1547 and 1549 nm. (b) 1545 and 1549 nm, (c) 1543 and 1549 nm, and (d) 1541 and 1549 nm.

idler delay ($t_s - t_i$) and signal-clock delay ($t_s - t_c$). On the signal-idler delay axis, the coincidences cluster at 24 ns and 32 ns , respectively. Moreover, as expected from the wavelength modulation at 2.5 MHz, we see that the coincidences due to the 1547 nm-pump appear between 200 and 400 ns on the signal-clock delay axis while the coincidences due to the 1549 nm-pump turn out between 0 and 200 ns. Similarly, we obtain the results for wavelength modulation between 1545 nm and 1549 nm [Fig. 2.8(b)], 1543 nm and 1549 nm [Fig. 2.8(c)], and 1541 nm and 1549 nm [Fig. 2.8(d)]; as expected, the signal-idler delays corresponding to the two different wavelengths again appear in separate halves of the signal-clock delay axis. The slight overlap between coincidence events recorded in the first and second halves of the clock period [in Figs. 2.8(a)–2.8(d)] only occurs because our group delay spread is starting to approach the pump gate period. And so our results show the first high-speed modulation of biphoton delays.

2.4 Outlook and Conclusion

Our delay control mechanism has the potential to positively impact several applications. For example, it could be used for on-the-fly delay correction and mitigating delay fluctuations in quantum networks—including clock synchronization and quantum communication networks. In the case of single-photon sources, this approach could be applied toward fast temporal multiplexing. For although our demonstration here concentrated on pump frequency tuning, one could also employ frequency shifting of heralded narrowband single photons directly. In this way, one dispersive medium—rather than active switches and fixed delay lines [51–53]—would impart the tunable delay required in temporally multiplexed single-photon sources. A second frequency converter at the output can then be used to remove the initial wavelength shift, thereby making our approach fully compatible with the need for frequency indistinguishability while simultaneously exploiting spectrally dependent delay.

In summary, we have demonstrated delay tuning of biphotons from the picosecond scale to several nanoseconds through pump frequency tuning. We also presented our results on modulating biphoton arrival times at a rate of 2.5 MHz. Moreover, the technique applies well to essentially any desired switching speed, so long as the modulated pump remains within the acceptance bandwidth of the nonlinear process. For example, GHz switching speeds could be reached in our setup with faster electronics and reduced total dispersion: this would effectively rescale the temporal axis but otherwise preserve performance. Such flexibility implies an assortment of design opportunities, so that it would also be interesting to examine this technique as a possible degree of freedom in novel quantum key distribution protocols, such as quantum analogues of pulse position modulation. Furthermore, continuous delay control would be realizable with only minor modifications to the present configuration. In our case, the permissible pump frequencies—and hence biphoton delays—are fixed to discrete values by the waveguide phase matching. Yet nonlinear media offering a broadband region of low phase mismatch would instead permit delay control over a continuum of pump wavelengths. Such would be the case with, e.g., a short nonlinear crystal or a QPM waveguide with a chirped poling pattern (see Appendix), where in general one compromises between peak nonlinear efficiency and total bandwidth [54].

3. ARBITRARY SHAPING OF BIPHOTON CORRELATIONS USING NEAR-FIELD FREQUENCY-TO-TIME MAPPING

3.1 Background

As discussed in the previous chapters, developing techniques to control the temporal correlations of biphotons has received significant attention in recent times. In this regard, we have already introduced a scheme based on dispersion to enable reconfigurable delay between a pair of entangled photons. Using dispersion, another method for manipulating the temporal correlations of entangled photons, in a manner similar to classical ultrashort pulses, is frequency-to-time mapping (FTM), whereby a considerable amount of dispersion allows the temporal correlation function to take on the shape of the biphoton spectrum [9, 56]. To achieve proper mapping of the spectrum into the temporal domain, the so-called temporal *far-field* condition has to be met; i.e., the second-order spectral phase constant has to be much larger than the square of the Fourier-limited temporal duration of the biphoton wavepacket [9,57,58]. But what if for a given spectral shape and desired temporal duration, the far-field limit is beyond reach?

In this chapter, we describe a technique adopted from classical photonics, termed *near-field* FTM [59], to demonstrate arbitrary shaping of the temporal correlations of broadband biphotons. Here successful FTM is achieved through spectral amplitude and phase pre-adjustment along with smaller amounts of dispersion (compared with the far-field approach). Moreover, unlike far-field FTM which leads to spreading of the correlations over a large temporal window, typically on the ns-scale, the near-field

The results of this chapter have been published in Ref. [55].

technique can be used to address a narrower temporal range (a few ps) as it does not require substantial dispersion.

3.2 Theory

Recall from Section 1.1 that the biphoton temporal correlation is the square-modulus of the wavepacket. Prior to any manipulation, the input temporal wavepacket $\psi_{\text{in}}(\tau)$ can simply be written in the form

$$\psi_{\text{in}}(\tau) \propto \int d\Omega\, \phi_{\text{in}}(\Omega)\, e^{-i\Omega\tau} \tag{3.1}$$

$\phi_{\text{in}}(\Omega)$ is the spectral amplitude of the input biphotons and conversely, can be written as the inverse-Fourier transform of the temporal wavepacket:

$$\phi_{\text{in}}(\Omega) \propto \int d\tau\, \psi_{\text{in}}(\tau)\, e^{i\Omega\tau} \tag{3.2}$$

In the presence of group velocity dispersion with a net quadratic spectral phase constant of A (the sum of second order spectral phase constants in the signal and idler paths), the biphoton wavepacket is modified as follows:

$$\psi_{\text{out}}(\tau) \propto \int d\Omega\, \phi_{\text{in}}(\Omega)\, e^{iA\Omega^2/2}\, e^{-i\Omega\tau} \tag{3.3}$$

which we can formulate to yield a Fresnel integral:

$$\psi_{\text{out}}(\tau) \propto \int d\tau'\, \psi_{\text{in}}(\tau')\, e^{-i\tau'^2/2A}\, e^{i\tau\tau'/A} \tag{3.4}$$

The expression of the biphoton wavepacket (Eq. 3.4) bears a resemblance to the complex envelope of a classical pulse propagating through dispersion; it is on this account that we can adopt the mathematical procedure in [59].

Far-field frequency-to-time mapping

If $A \gg \Delta\tau^2\, (\sim \Delta f^{-2})$—where $\Delta\tau$ is the temporal duration of $|\psi_{\text{in}}(\tau)|$ and is *inversely* proportional to Δf, its finest spectral feature—then the first complex ex-

ponential term under the integral in Eq. 3.4 can be dropped as an approximation. Consequently, it would be possible to write the resulting wavepacket as

$$\psi_{\text{out}}(\tau) \propto \int d\tau' \, \psi_{\text{in}}(\tau') \, e^{i\tau\tau'/A}, \tag{3.5}$$

which, when compared to Eq. 3.2, implies that $\psi_{\text{out}}(\tau)$ is identical to $\phi_{\text{in}}(\Omega = \tau/A)$. Therefore, we arrive at $G^{(2)}_{\text{out}}(\tau) = |\phi_{\text{in}}(\Omega = \tau/A)|^2$, meaning that the temporal correlation is now essentially a scaled-replica of the biphoton spectrum.

Demonstrations of far-field FTM have already been shown using biphotons from different sources. The earliest work in this regard [9] reported examples in which the authors implemented far-field mapping (using dispersion from long fiber spools) to measure the continuous broadband spectra of type-I and type-II spontaneous parametric downconversion (SPDC) sources. While in some other experiments, we used strong dispersion from a chirped fiber Bragg grating to demonstrate FTM for a relatively flat-top spectrum obtained from type-0 SPDC [Fig. 2.6(b)], and a biphoton comb structure from a microring resonator [56]. To add to this body of work, we further show far-field FTM after spectral-amplitude shaping of SPDC biphotons. Using a pulse shaper, we program three rectangular filters with bandwidths of 50, 100 and

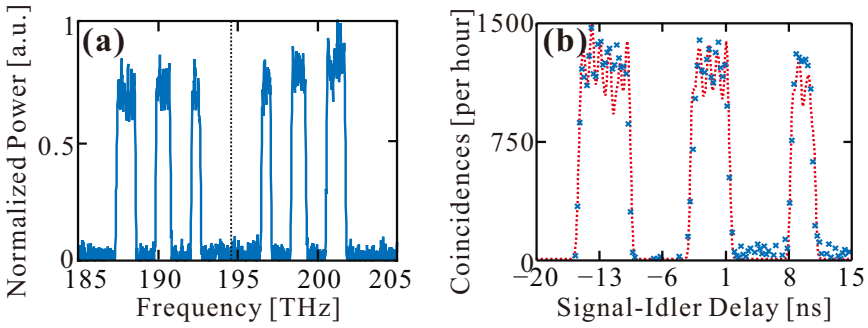

Fig. 3.1. Experimental example of far-field frequency-to-time mapping. (a) Biphoton spectrum measured after three rectangular filters are applied on both signal and idler sides. (b) The measured temporal correlation after biphotons propagate through a chirped fiber Bragg grating with A of 5200 ps^2. The measured temporal correlation (blue markers) agrees well with the theoretical prediction (red dashed trace) in the far-field region.

150 GHz, on both signal and idler photons, as can be seen in Fig. 3.1(a). After amplitude shaping of the biphotons, we propagate them through our chirped fiber Bragg grating with a net dispersion constant of $5200\,\mathrm{ps}^2$, which easily meets the requirement for far-field FTM. A measure of the temporal correlation [3.1(b)] now shows a structure that resembles the biphoton spectrum [Fig. 3.1(a)].

Near-field frequency-to-time mapping

If A is not large enough to meet the far-field FTM requirement (i.e., operation is in the near-field regime), we can still obtain the expression in Eq. 3.5 using a different approach. This time, we will eliminate the first complex exponential term under the integral in Eq. 3.4 by replacing the input wavepacket with a modified version,

$$\psi_{\mathrm{nf}}(\tau') = \psi_{\mathrm{in}}(\tau') \times e^{i\tau'^2/2A} \tag{3.6}$$

after which propagating through dispersion allows us to attain a wavepacket given by

$$\psi_{\mathrm{out}}(\tau) \propto \int d\tau'\, \psi_{\mathrm{nf}}(\tau')\, e^{i\tau\tau'/A} \tag{3.7}$$

Therefore, irrespective of the amount of dispersion available, we are able to map a target shape to the temporal domain by pre-adjusting the biphoton wavepacket before propagating it through dispersion. Indeed the expression in Eq. 3.6 points to the utilization of quadratic temporal phase (a time lens) [60–62] for pre-adjustment. However, in our experiments, we realize the functionality of the time lens by applying the frequency-domain equivalent of the expression in Eq. 3.6 using a programmable pulse shaper—this Fourier approach is termed *virtual* time lensing [59]. Hence our near-field shaping procedure is as follows:

1. Compute $\psi_{\mathrm{nf}}(\tau') = \psi_{\mathrm{in}}(\tau') \times \exp(i\tau'^2/2A)$.
2. Fourier transform $\psi_{\mathrm{nf}}(\tau')$ to its frequency-domain equivalent, $\phi_{\mathrm{nf}}(\Omega)$.
3. Apply the near-field frequency-domain mask to the biphoton using a pulse shaper.

4. Propagate biphoton through dispersive medium with net dispersion constant A.

As will be observed in our experiments, it is also worth noting that the spectral intensity for a near-field mask is identical in shape to the distorted temporal correlation. The spectral mask applied to the biphotons for near-field FTM is the frequency-domain counterpart of $\psi_{\text{nf}}(\tau')$ in Eq. 3.6, which can be written as

$$\phi_{\text{nf}}(\Omega) = \int d\tau' \, \psi_{\text{in}}(\tau') \, e^{i\tau'^2/2A} \, e^{i\Omega\tau'}. \tag{3.8}$$

Thus, we we identify a one-to-one correspondence when we compare the form of $\phi_{\text{nf}}(\Omega)$ to that of $\psi_{\text{out}}(\tau)$ in Eq. 3.3.

3.3 Experimental Demonstration

The experimental setup we utilize is identical to that in Fig. 2.2. We couple type-0 SPDC biphotons into a programmable pulse shaper (Finisar WaveShaper 1000S) capable of independent amplitude and phase control at a 10-GHz specified resolution over the band from 191.250 to 196.275 THz. The pulse shaper is used to apply amplitude and spectral phase filters, in addition to the quadratic spectral phase required for our FTM demonstrations. Upon leaving the pulse shaper, we use sum-frequency generation (SFG) along with a single-photon detector for sub-picosecond resolution measurements of the biphoton temporal correlations (see Section 2.3.1 for more details on using SFG for high-resolution temporal correlation measurements).

To perform FTM, we start with programming the desired spectral shapes on the biphoton spectrum via the pulse shaper. Since frequency entanglement ensures that the net transfer function on the biphoton is the product of the complex filters applied to the signal and idler photons (see Section 1.2), we choose to shape only signal photons and always leave the idlers untouched in the following experiments.

3.3.1 Series of Gaussian Filters

For our first demonstration, we implement a series of Gaussian filters, each with a full-width at half-maximum (FWHM) linewidth of 210 GHz, spaced by 600 GHz. Figure 3.2(a) shows the biphoton spectrum acquired with an optical spectrum analyzer (OSA) after applying the filters to the signal-half while leaving the idler-half untouched. The temporal correlation is subsequently stretched by a quadratic spectral phase ($A = 0.6\,\mathrm{ps}^2$) programmed on the shaper, which emulates a 30-m-long Corning SMF-28e fiber. Noticeably, the output stretched temporal correlation, shown in Fig.

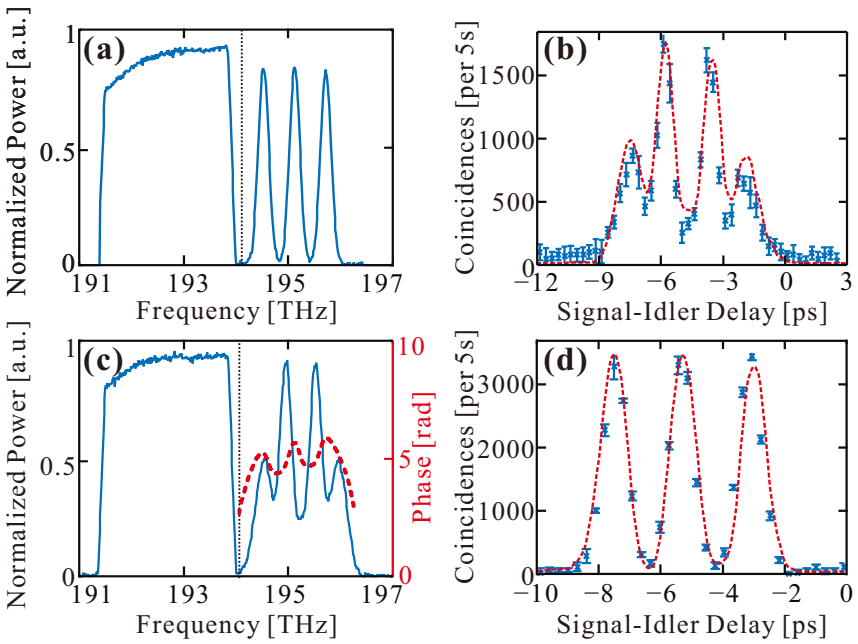

Fig. 3.2. (a) Biphoton spectrum measured with an optical spectrum analyzer (OSA) after three Gaussian passbands, each with a full-width at half-maximum (FWHM) of 210 GHz, spaced by 600 GHz, are applied to the signal. (b) The temporal correlation measured after a quadratic spectral phase($A = 0.6\,\mathrm{ps}^2$) is applied on the spectrum in (a). (c) Pre-adjusted biphoton spectrum (solid; acquired with an OSA) and extra spectral phases (dashed; programmed on the pulse shaper) needed to facilitate near-field FTM. (d) The measured temporal correlation utilizing the near-field FTM method is in good accordance with theoretical prediction.

3.2(b), is seriously distorted as the far-field FTM requirement is strongly violated; in this case, since the smallest biphoton spectral feature is 210 GHz, the stipulation for far-field FTM is satisfied only for a quadratic spectral phase constant larger than 23 ps^2. However, we can circumvent the far-field condition by utilizing the near-field approach. We use the pulse shaper to apply the frequency-domain equivalent of $\psi_{nf}(\tau')$ to the biphotons. Figure 3.2(c) shows the new biphoton spectrum—amplitude- and phase-shaped based on the absolute value squared and the phase of $\phi_{nf}(\Omega)$, respectively. The output temporal correlation, in Fig. 3.2(d), now shows clearly mapped Gaussian peaks after being stretched again by quadratic spectral phase ($A = 0.6ps^2$).

3.3.2 Pair of Triangular Filters

To show another example of the near-field FTM method, we implement a pair of triangular shapes (FWHM of each triangle is 300 GHz) [Fig. 3.3(a)] and apply group velocity dispersion to the biphotons. The measured temporal correlation is distorted [Fig. 3.3(b)] once again after being stretched by the same amount of quadratic spectral phase ($A = 0.6\,ps^2$); successful far-field FTM requires $A \gg 11$ ps^2. However, clear mapping is achieved [Fig. 3.3(d)] once the specific complex filter is computed in advance and applied to the biphotons [Fig. 3.3(c)] before they experience dispersion. A closer look at the results also reveals that the orientation of the triangles in the correlation plot [Fig. 3.3(d)] is flipped when compared to the applied masks [Fig. 3.3(a)]. This is due to the sign of A; the oppositely signed dispersion constant will ensure that the orientation of the triangles in the temporal measurement is identical to that of the initial spectral masks.

Here we would like to emphasize that the near-field mask is complex, composed of not only an amplitude but also a phase which varies depending on the specifications of the target temporal correlation. As can be seen, the applied spectral phase in Fig. 3.3(c) is distinct from that applied in Fig. 3.2(c). And even though the phases here are only a few radians, they are vital for successful implementation of this technique—

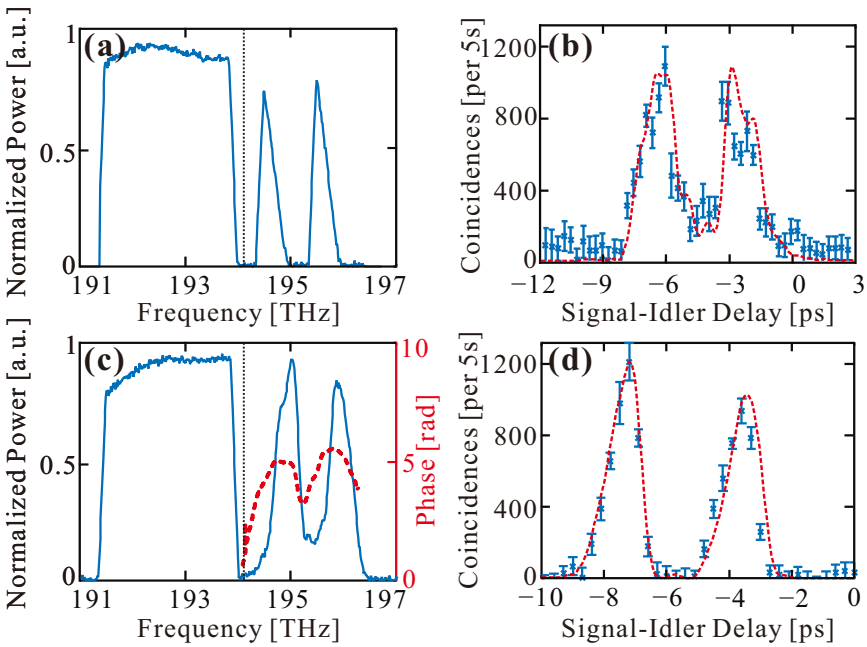

Fig. 3.3. (a) Biphoton spectrum and (b) the temporal correlation measured after amplitude filtering and quadratic spectral phase ($A = 0.6\,\mathrm{ps}^2$) are applied via the pulse shaper. (c) Pre-adjusted biphoton spectrum and (d) the measured temporal correlation utilizing the near-field FTM method.

whereas in the far-field limit, the correlation is insensitive to such additional small input spectral phases.

3.3.3 Flat-Top Waveform with Tunable Duration

Lastly, we show that for a target shape, the near-field FTM method possesses strong tunability in controlling the temporal correlation width, while maintaining the total photon flux. Although the pre-adjusted complex biphoton spectrum, $\phi_{\mathrm{nf}}(\Omega)$, is dependent on the amount of dispersion available (Eq. 3.8), the spectral energy remains constant. This can be understood through Parseval's theorem,

$$\frac{1}{2\pi}\int d\Omega\,|\phi_{\mathrm{nf}}(\Omega)|^2 = \int d\tau'\,|\psi_{\mathrm{nf}}(\tau')|^2, \tag{3.9}$$

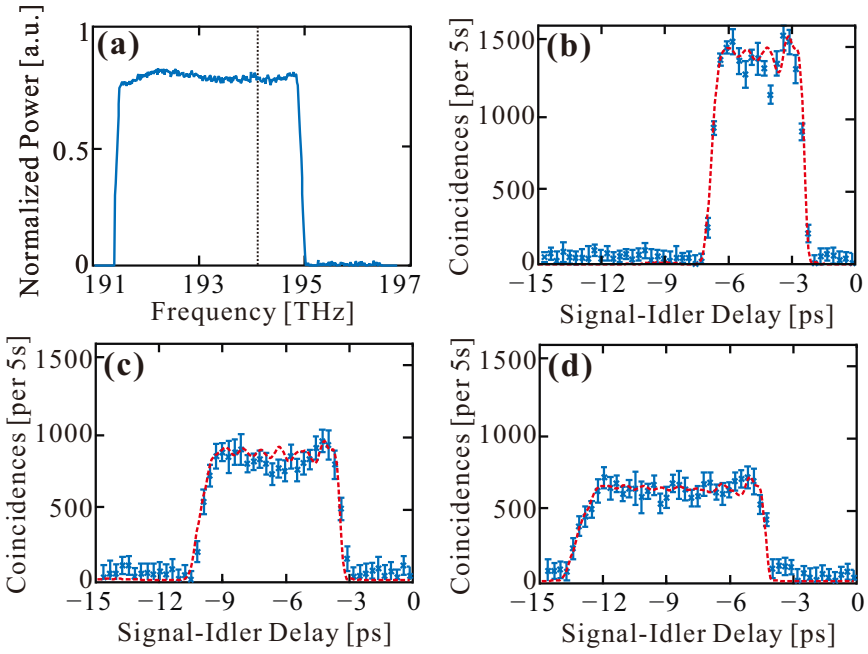

Fig. 3.4. (a) Biphoton spectrum measured after a rectangular filter, with a FWHM of 1 THz, is applied on the signal side. The measured temporal correlations after a quadratic spectral phase with (b) $A = 0.8\,\mathrm{ps}^2$ (c) $A = 1.2\,\mathrm{ps}^2$ and (d) $A = 1.6\,\mathrm{ps}^2$ is applied (after the near-field FTM correction) shows good agreement with the theoretical curves. The measured FWHM are 4.4, 6.7 and 8.9 ps, respectively

which allows us to compute the spectral energy of the biphoton in the temporal domain. Since, using Eq. 3.6, $|\psi_{\mathrm{nf}}(\tau')|^2 = |\psi_{\mathrm{in}}(\tau')|^2$, we can infer that the spectral energy of the near-field corrected biphoton is always equal to the energy of the input wavepacket, and does not change as a function of dispersion.

Experimentally, we illustrate this property of strong tunability by using different dispersion values to obtain a rectangular target shape. Figure 3.4(a) provides the biphoton spectrum after applying a rectangular filter with a FWHM of 1 THz. We then compute and pre-adjust the biphoton spectrum to explore near-field FTM for three different dispersion constants, $A = 0.8$, 1.2 and 1.6 ps^2, emulating a 40-, 60- and 80-meter-long Corning SMF-28e, respectively—these quadratic spectral phases do not satisfy the criteria for far-field FTM. The corresponding measured temporal

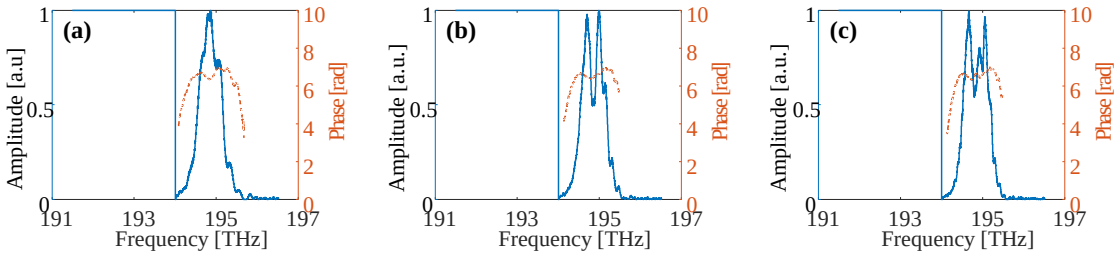

Fig. 3.5. Near-field correction masks (amplitude and phase) for (a) $A = 0.8\,\mathrm{ps}^2$ (b) $A = 1.2\,\mathrm{ps}^2$ and (c) $A = 1.6\,\mathrm{ps}^2$.

correlations shown in Figs. 3.4(b), 3.4(c) and 3.4(d) demonstrate excellent mapping to the target waveform with a FWHM of 4.4, 6.7 and 8.9 ps, respectively, in close agreement with theoretical predictions. Moreover, the maximum coincidence counts recorded in Figs. 3.4(b)–3.4(d) are ∼1400, ∼930 and ∼700 per 5 s, respectively, from which we obtain a correlation width-height product of 6160, 6231, and 6230 counts per 5 s, respectively. This suggests that the total photon-pair flux stays almost constant even in the presence of different values of A. We also highlight the fact that the near-field correction masks applied to obtain the flat-top temporal correlations in Fig. 3.4 are different for the chosen dispersion values; Figs. 3.5(a), 3.5(b) and 3.5(c) show the amplitude and phase masks implemented to obtain the results in Figs. 3.4(b), 3.4(c) and 3.4(d), respectively.

3.4 Outlook and Conclusion

In summary, we have shown that the near-field frequency-to-time mapping technique can be implemented to create arbitrary temporal correlation functions in the picosecond region. By pre-adjusting the complex biphoton spectrum with a Fourier-transform pulse shaper, the target shape can be mapped onto the biphoton temporal waveform after propagating through a small amount of dispersion. And unlike amplitude-only filtering which results in a reduction of biphoton flux to achieve longer

temporal correlations, this near-field mapping approach synthesizes both amplitude and phase filtering for efficient shaping of biphotons. Lastly, near-field frequency-to-time mapping of biphotons could play a role in modifying dispersion requirements for time-frequency quanturm key distribution protocols.

4. GENERATION OF BIPHOTON CORRELATION TRAINS THROUGH PROGRAMMABLE SPECTRAL FILTERING

4.1 Background

Biphoton frequency combs—entangled photons occurring in a superposition of discrete spectral mode pairs [64–73]—offer much promise, as such biphotons have the potential to combine the unique characteristics of quantum entanglement [4, 74] with the precision of classical optical frequency comb metrology [75,76], in addition to serving as high-dimensional states for quantum information processing [77]. Other names used in place of biphoton frequency combs include two-photon frequency combs, quantum frequency combs and frequency-bin entangled photons. Several configurations generating such photonic states have been implemented, including spontaneous four-wave mixing in microresonators [56,73,78–83], cavity-enhanced spontaneous parametric downconversion (SPDC) [65–68, 72, 84], and direct filtering of broadband biphotons [70,71]. Assuming phase locking of the constituent spectral modes, the temporal correlation function of these biphoton frequency combs consists of a train of peaks, the number of which is approximately equal to the spectral mode spacing divided by the linewidth. Indirect measurements based on Hong-Ou-Mandel interference have revealed periodic coincidence dips indicative of such correlation trains [65, 70, 71], and with sufficiently low repetition rates, direct correlation measurements have been made possible as well [66,68,72,85]. Moreover, it has been predicted theoretically [86] that propagation of these two-photon frequency combs through dispersive media will produce revivals of the temporal correlation function at discrete dispersion values, through an extension of the classical temporal Talbot effect [41, 87].

The results of this chapter have been published in Ref. [63].

In this chapter, we experimentally examine a new method for generating biphoton correlation trains based on optical filtering with spatial light modulators [48, 57, 88]. Our technique permits the creation of extremely high-repetition-rate (∼THz) trains, with programmable control of peak number and spacing. We explore both amplitude and phase filtering approaches, each with its own advantages. With amplitude filtering, we create coherent biphoton frequency combs with tunable properties and experimentally demonstrate the two-photon temporal Talbot effect for the first time. Alternatively, when the temporal phase of the biphoton wavepacket is unimportant, we show that spectral phase-only filtering can yield correlation trains with much greater efficiency, even though the filtered spectrum does not contain a series of a discrete frequencies—i.e., it is not comb-like. Our results therefore not only contribute to the development of two-photon frequency combs, but also show that for some applications it may be possible to remove the requirement of a true frequency comb in favor of a low-loss spectral phase filter.

4.2 Experimental Demonstration

The experimental setup we implement is identical to that shown in Figure 2.2. Broadband entangled photons are generated through type-0 SPDC and then coupled into a pulse shaper (Finisar WaveShaper 1000S). We use the pulse shaper to apply spectral amplitude and/or phase to the signal-idler spectrum, after which we use sum-frequency generation for ultrafast coincidence detection. Detailed description of the setup can be found in Section 2.3.1. Again, we define the signal (idler) photon as having frequency greater (less) than one-half that of the pump. To aid comparison with subsequent measurements, we first show the biphoton spectrum and its corresponding singly peaked correlation function generated without any additional spectral modulation in Figs. 4.1(a) and (b), respectively.

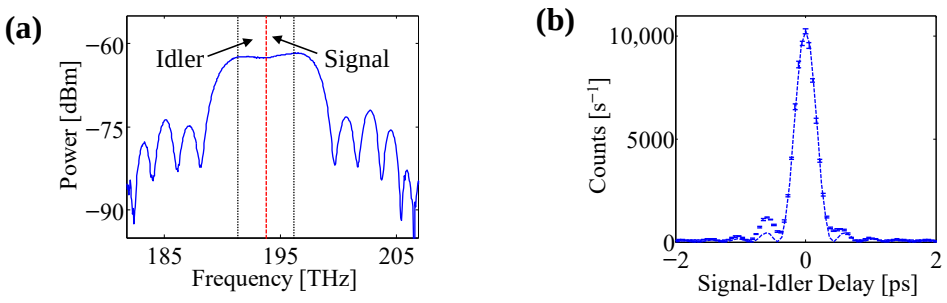

Fig. 4.1. (a) Biphoton spectrum showing flat-top signal and idler bands. (b) Measured correlation function with pulse shaper compensating setup dispersion. The full-width at half-maximum of the correlation peak is about 370 fs. Error bars represent the standard deviation of five 1-s measurements, and the dotted curve gives the theoretical result.

4.2.1 Amplitude Filtering

In the case of amplitude filtering, we first note that there exists a fundamental tradeoff between overall flux and the number of peaks generated. Defining ω_c as the bandwidth of a given spectral passband and ω_{FSR} as the spacing between passbands, the total number of peaks in the train is proportional to the ratio $\omega_{\mathrm{FSR}}/\omega_c$, whereas the total power transmissivity is *inversely* proportional to this quantity [89]. Combined with the fact that the optical energy is now distributed among many peaks, the maximum count rate actually decreases quadratically with the number of correlation peaks. Therefore to remain comfortably above the background, we program on the signal spectrum three passbands spaced at 650 GHz, each with the fractionally broad bandwidth of 250 GHz, and leave the idler untouched. The measured signal spectrum is given in Fig. 4.2(a), acquired with an optical spectrum analyzer at a resolution of 62.5 GHz. The spacing-to-passband ratio predicts about three temporal peaks, and this is precisely what we find for the filtered biphoton correlation function, as shown in Fig. 4.2(b). The result is in excellent agreement with theory, confirming the ability

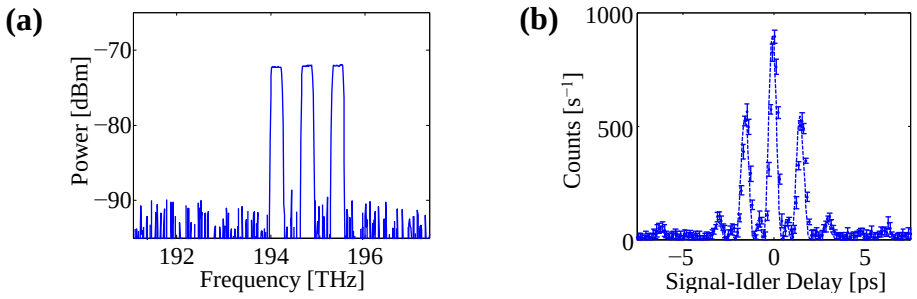

Fig. 4.2. Amplitude filtering. (a) Signal spectrum measured after the pulse shaper (with idler blocked). The nearly flat spectrum of Fig. 4.1(a) is converted to a set of three passbands, spaced by 650 GHz and each of width 250 GHz. (b) Measured temporal correlation function for the spectrum in (a), but with the low-frequency idler passed. A 650-GHz correlation train with three peaks is generated, in accordance with theoretical predictions.

to produce correlation trains through straightforward amplitude filtering by our pulse shaper.

4.2.2 Biphoton temporal Talbot effect

The biphoton comb generated in the previous section lends itself well to the examination of the temporal Talbot effect. The spatial Talbot phenomenon—first reported by Henry Talbot in 1836 [90]—describes the revival of spatial interference patterns at discrete distances away from a periodic grating [91, 92], an effect which has recently been observed for entangled photons as well [93,94]. The temporal counterpart which we consider here derives from the formal mathematical equivalence between paraxial diffraction and narrowband dispersion, known as space-time duality [60, 95]. In this dual version, a periodic electric field envelope is exactly replicated after propagation through multiples of the so-called Talbot dispersion [41, 87].

The origin of this effect for biphoton frequency combs can be understood most simply by considering the ideal case of a series of comb lines with infinitely narrow linewidths followed by second-order dispersion. Specifically, in Eq. 1.11 we take

$$H_{\mathrm{s}}(\omega_0 + \Omega) = \sum_{n=0}^{N-1} a_n \delta(\Omega - n\omega_{\mathrm{FSR}}) e^{iA_{\mathrm{s}}\Omega^2/2} \tag{4.1}$$

and

$$H_{\mathrm{i}}(\omega_0 - \Omega) = e^{iA_{\mathrm{i}}\Omega^2/2} \tag{4.2}$$

which yields the final biphoton amplitude

$$\psi(\tau) \propto \sum_{n=0}^{N-1} \phi(n\omega_{\mathrm{FSR}}) a_n e^{iA_{\mathrm{eff}}n^2\omega_{\mathrm{FSR}}^2/2} e^{-in\omega_{\mathrm{FSR}}\tau} \tag{4.3}$$

where $A_{\mathrm{eff}} = A_{\mathrm{s}} + A_{\mathrm{i}}$, with the familiar Franson dispersion cancellation condition resulting when $A_{\mathrm{s}} = -A_{\mathrm{i}}$. Again, we note that the entanglement shared between signal and idler photons allows the same expression to be obtained when applying all narrowband filters on the idler instead, for it is only the *product* of signal-idler spectral filters which enters in Eq. 1.11. Returning to Eq. 4.3 we readily observe that the periodic wavepacket completely replicates itself for values of A_{eff} that are integer multiples of the Talbot dispersion A_{T}, where

$$A_{\mathrm{T}} = \frac{4\pi}{\omega_{\mathrm{FSR}}^2} \tag{4.4}$$

as this ensures that the dispersion factor in Eq. 4.3 evaluates to unity for all n [86]. Taking the limit of infinitesimal linewidth for the signal spectrum shown in Fig. 4.2(a) gives the theoretical Talbot carpet shown in Fig. 4.3(a). At integer multiples of A_{T}, perfect reconstruction of the biphoton train is realized; at half-integer multiples, revivals with a half-period delay shift are obtained.

For real biphoton combs, the temporal train is not perfectly periodic, but damped by an envelope with duration inversely proportional to the non-vanishing linewidth, a well-known effect in classical pulse shaping [88]; therefore only approximate coherence revivals are possible. In particular, dispersion eventually spreads out the entire wavepacket, meaning that the self-imaging phenomenon is discernible only up to a

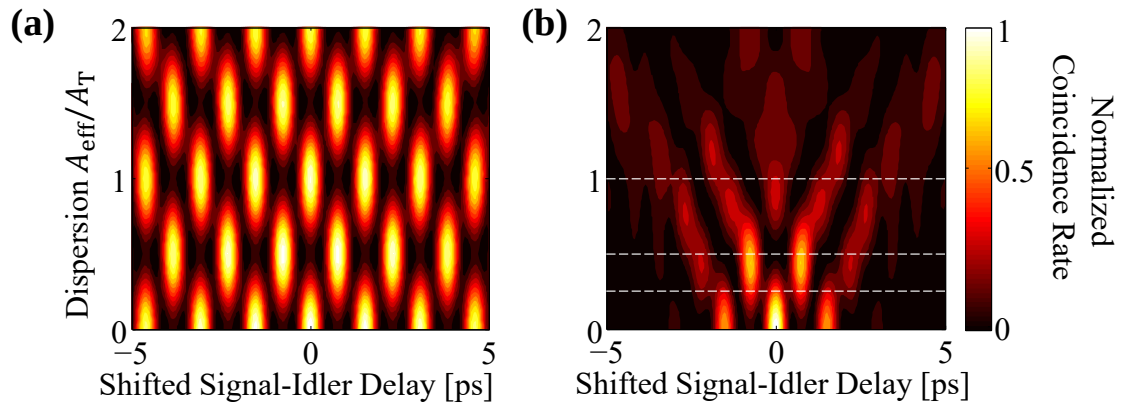

Fig. 4.3. Simulated Talbot carpets. (a) Theoretical temporal correlation as a function of applied dispersion, for our three-peak signal spectrum but with infinitely narrow linewidth. Perfect revivals are observed at integer multiples of the Talbot dispersion. (b) Corresponding correlation function when the linewidth is 250 GHz, as in Fig. 4.2(a). Dashed horizontal lines indicate the values of dispersion considered in Fig. 4.4. Imperfect—but still clear—self-imaging is obtained over the first Talbot length, limited by dispersive spreading. (An overall delay shift has been subtracted off for clarity.)

finite multiple of $A_{\rm T}$ [86]. With the fractionally large linewidth in our experiments ($\omega_{\rm FSR}/\omega_c = 2.6$), chosen to minimize loss, measurable Talbot interference is limited to approximately the dispersion regime $0 < |A_{\rm eff}| < A_{\rm T}$. This is nevertheless sufficient to observe the basic effect. Figure 4.3(b) presents the theoretical Talbot carpet for our filtered biphoton source, plotting the temporal two-photon correlation function $G^{(2)}(\tau)$ as a function of net dispersion; horizontal lines mark the specific dispersions which we consider experimentally below. At each value of the dispersion, we have shifted the wavepacket center to zero delay, in much the same way as retarded time is calculated for classical pulses [57]. For in general, the applied dispersion introduces a frequency-dependent delay given by $\tau(\Omega) = A_{\rm eff}\Omega$, and since the mean signal frequency offset $\langle\Omega\rangle \neq 0$, the mean signal-idler delay varies with applied dispersion. Intuitively, the fact that signal and idler are separated by frequency implies that group

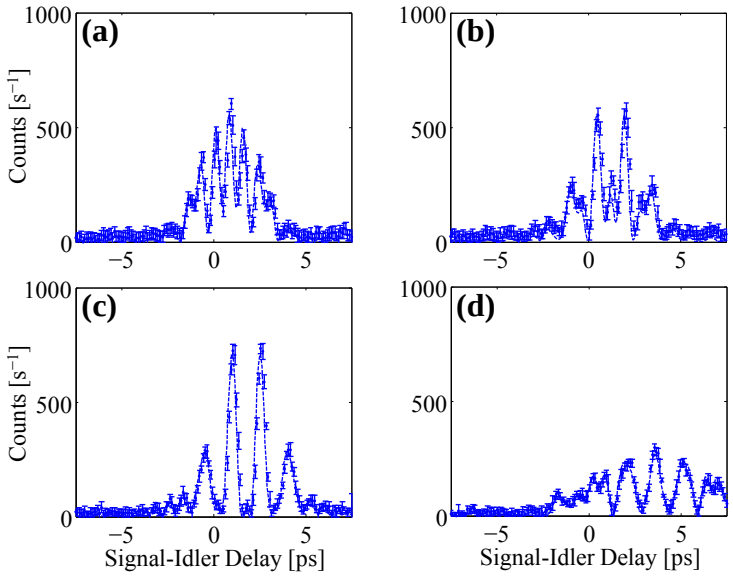

Fig. 4.4. Examples of Talbot interference. Biphoton correlation functions measured for dispersion A_{eff} equal to (a) $0.25A_{\text{T}}$, (b) $0.35A_{\text{T}}$, (c) $0.5A_{\text{T}}$, and (d) A_{T}.

velocity dispersion forces them to travel at different mean speeds; therefore their average temporal separation increases as they propagate through greater amounts of dispersion.

Experimentally, we explore the temporal Talbot effect by programming the optical dispersion directly on the pulse shaper and observing the change to the biphoton correlation function of Fig. 4.2(b). For our 650-GHz correlation trains, the Talbot dispersion parameter A_{T} is 0.753 ps^2, and we apply net dispersions satisfying

$$A_{\text{eff}} = 0.25A_{\text{T}}, 0.35A_{\text{T}}, 0.5A_{\text{T}}, A_{\text{T}} \tag{4.5}$$

The result for the quarter-Talbot case is presented in Fig. 4.4(a). The correlation train has doubled in repetition rate to 1.3 THz and matches theory well. Similar quarter-Talbot-based repetition-rate multiplication has been used to generate classical pulse trains as well [96–98]. In Fig. 4.4(b), the dispersion is now 35% of the Talbot value, with the odd peaks increasing in relative magnitude and the even ones falling

off, a transition which is made complete at the half-Talbot mark, as highlighted in Fig. 4.4(c). High-extinction peaks at 650 GHz are again clearly evident, shifted under the envelope by half a period with respect to the zero-dispersion case. Finally, the function is returned to its original state at a full Talbot dispersion [Fig. 4.4(d)], although the effects of finite linewidth are taking their toll as the train spreads out, resulting in a lower maximum count rate and the formation of extra satellite peaks.

For direct comparison of the coherence revivals, we numerically correct for the temporal offset due to signal-idler group velocity difference and overlay the zero-, half-, and full-Talbot correlation functions in Fig. 4.5(a), which clearly shows resurgence of the 650-GHz train due to temporal Talbot interference. In likewise fashion, we superpose the quarter- and zero-Talbot results in Fig. 4.5(b), highlighting the repetition-rate doubling. Such rate multiplication through the temporal Talbot effect is particularly advantageous in that it is achieved without removing spectral lines, which would instead reduce overall flux by an amount equal to the frequency mul-

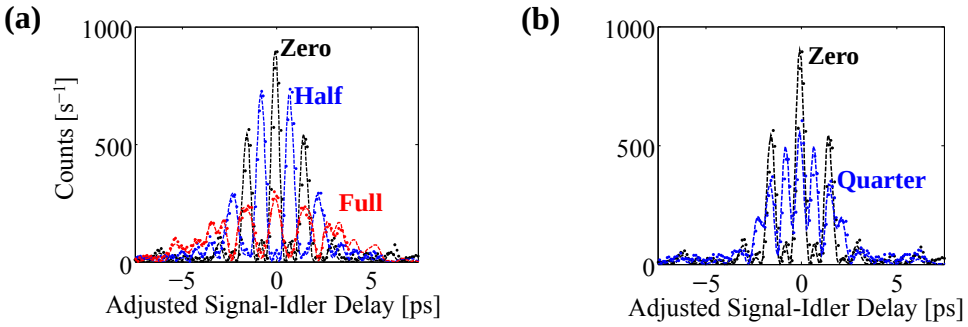

Fig. 4.5. Coherence revival comparison. (a) Overlay of the zero-, half-, and full-Talbot cases, after delay correction to center all at zero delay. 650-GHz trains are seen in all cases, with the finite linewidth responsible for overall spreading. (b) Overlay of the zero- and quarter-Talbot cases, again shifted so both are centered at zero delay. The original 650-GHz train is doubled to 1.3 THz at the quarter-Talbot dispersion, as expected from theory. (In both plots, error bars have been omitted for clarity.)

tiplication factor [99–101]. And our results fully confirm the theory of Ref. [86] in extending the temporal Talbot effect to biphotons.

4.2.3 Phase-only Filtering

For circumstances in which the temporal biphoton phase is unimportant, and one is concerned only with the correlation function itself, an alternative method based on spectral phase-only filtering can be used to produce correlation trains much more efficiently than amplitude filtering, utilizing a technique developed early in the history of classical femtosecond pulse shaping [89] and applied to, e.g., control of molecular motion [102]. To understand this approach, consider the modulus squared of Eq. 1.11, where we define $K(\Omega) = \phi(\Omega)H_{\mathrm{s}}(\omega_0 + \Omega)H_{\mathrm{i}}(\omega_0 - \Omega)$ for simplicity. This allows us to write the temporal correlation function as

$$G^{(2)}(\tau) = \int d\Omega \int d\Omega'\, K^*(\Omega)K(\Omega')e^{i(\Omega-\Omega')\tau} \tag{4.6}$$

Redefining a new integration variable Δ according to $\Delta = \Omega' - \Omega$ and replacing Ω' gives

$$G^{(2)}(\tau) = \int d\Delta\, e^{-i\Delta\tau} \int d\Omega\, K^*(\Omega)K(\Omega + \Delta) \tag{4.7}$$

Thus the measured correlation function is given by the inverse Fourier transform of the autocorrelation of the filtered biphoton spectrum, and so the condition for a periodic train requires only that this *autocorrelation* consist of discrete peaks—$K(\Omega)$ itself need not be comb-like. In our case, we achieve the desired spectral peaks by taking $H_{\mathrm{i}}(\omega) = 1$ and choosing $H_{\mathrm{s}}(\omega)$ to be a periodic repetition of a maximal-length binary phase sequence (M-sequence) [103], which indeed possesses discrete spikes in its autocorrelation. Since the input biphoton spectrum is essentially flat over the pulse-shaper passband, no additional amplitude equalization is required, and so the spectral filtering is ideally lossless. In stark contrast to the amplitude filtering of Section 4.2.1, the maximum count rate drops only linearly with the number of peaks generated by phase filtering—instead of quadratically—thereby offering the potential for significantly longer biphoton trains at a given flux. However, we emphasize that

temporal interference effects, such as the Talbot phenomenon, do not carry over to these non-comb-like states, since the inter-peak temporal phase varies widely.

We first consider the length-7 M-sequence [0 1 1 1 0 1 0], where we map the zeros to phase 0 and the ones to phase π. Each element is programmed to cover a bandwidth of 115 GHz, giving a total of three repetitions of the M-sequence over the 2.415-THz signal passband set on the pulse shaper here. The measured correlation train is presented in Fig. 4.6(a), again showing good agreement with theory. The missing peak at zero delay results from destructive interference between the 0- and π-phase elements [89]. We can restore the central peak by changing the binary phase shift; taking 0.78π for the shift instead of the original π, we obtain the blue curve in Fig. 4.6(b). A high-contrast train at 805 GHz is generated under a smooth envelope, without any amplitude filtering of the biphoton spectrum.

To directly compare the flux improvement over the equivalent amplitude filter, we also program three repetitions of the amplitude sequence [1 0 0 0 0 0 0] over the same bandwidth, which gives the desired 805-GHz train but at the cost of removing

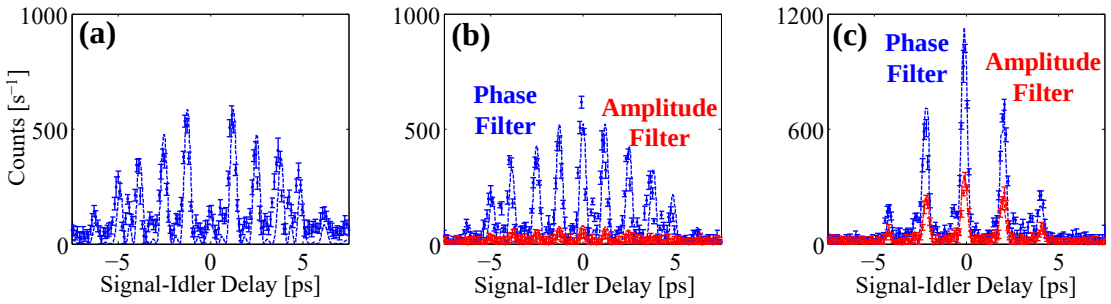

Fig. 4.6. M-sequence filtering. (a) Measured correlation function for length-7 M-sequence with a π phase shift. (b) Correlation function for the same M-sequence but with a 0.78π phase shift (blue), compared to an amplitude filter at the same repetition rate (red). (c) Correlation function for a length-3 M-sequence with a 0.65π phase shift (blue) and the corresponding amplitude filter. In both (b) and (c), phase filtering yields a flux improvement roughly equal to the number of peaks.

much of the original biphoton spectrum. This result (red curve) is compared to the phase-only approach in Fig. 4.6(b); the amplitude case is reduced approximately 7-fold in integrated flux and is barely visible above the noise. We run a similar comparison for length-3 sequences as well, giving each symbol a bandwidth of 160 GHz and replicating the sequence five times over a 2.4-THz total signal bandwidth. For the phase filter, we use the M-sequence [1 0 1], where ones now map to a phase shift of 0.65π; for the amplitude filter, we take the transmission sequence of [1 0 0]. Both results are compared in Fig. 4.6(c), and a count rate improvement of about 3:1 is observed for the phase-only sequence. These results stress the substantial flux increases facilitated by pure phase filtering, which—coupled with the programmable control of peak number and spacing—make such states valuable tools for future work with high-repetition-rate biphotons.

4.2.4 Resolution Limitations with Shaper-Assisted Correlation Train

We have discussed how to use a pulse shaper to generate correlation trains through amplitude filtering, and how flux reduction resulting from amplitude filtering can be mitigated through phase-only filtering. However, there still remains a separate restriction imposed by the finite pulse-shaper resolution: time aperture. The time aperture, or the maximum temporal duration over which the shaped waveform will accurately reproduce that of the ideal infinite-resolution mask, is fixed by the resolvable frequency spacing [48, 57, 88]. If we model this temporal window as a Gaussian function with an intensity full-width at half-maximum (FWHM), $T_{\mathrm{FWHM}} = (2\ln 2)^{1/2}T$, the effect of finite resolution is to yield the impulse response $h(t)$ (the inverse Fourier transform of the transfer function $H(\omega)$)

$$h(t) = h^{(0)}(t)e^{-t^2/T^2} \tag{4.8}$$

where $h^{(0)}(t)$ is the impulse response corresponding to an infinite-resolution pulse shaper. Therefore the generated trains are restricted to a time window roughly equal to the inverse of the spectral resolution. Now when the characteristic frequency scale

$\delta\omega$ over which the ideal mask $H^{(0)}(\omega)$ varies satisfies $1/\delta\omega \ll T$, $h(t) \approx h^{(0)}(t)$, and the effects of finite resolution are negligible (which was the case in our results up to now). However, to explicitly examine the limits of our biphoton correlation train generator, now we choose filter functions that are significantly modified by the time aperture. Moreover, because we use the pulse shaper not only for generation but also for imposing the relative signal-idler delay, we suffer on two counts: first in the creation of the correlation train, and second in its measurement. Letting $\tilde{\psi}(\tau)$ denote the measured wavepacket under the effects of finite pulse-shaper resolution, to best reflect the experimental conditions of our measurement, the expression of the biphoton wavepacket must be modified to

$$\tilde{\psi}(\tau) = \int d\Omega\, \phi(\Omega) \tilde{H}_{\mathrm{s}}(\omega_0 + \Omega, \tau/2) \tilde{H}_{\mathrm{i}}(\omega_0 - \Omega, -\tau/2) \tag{4.9}$$

where the delay τ is explicitly imposed by the filters, with the signal temporally shifted by $\tau/2$ and the idler by $-\tau/2$ [13]. The corresponding infinite-resolution filters are thus

$$\tilde{H}_{\mathrm{s}}^{(0)}(\omega_0 + \Omega, \tau/2) = C(\Omega) e^{-i\Omega\tau/2} \tag{4.10}$$

and

$$\tilde{H}_{\mathrm{i}}^{(0)}(\omega_0 - \Omega, -\tau/2) = e^{-i\Omega\tau/2} \tag{4.11}$$

where $C(\Omega)$ is the ideal spectral code applied to the signal photon. The finite-resolution filters $\tilde{H}_{\mathrm{s}}(\omega, \tau)$ and $\tilde{H}_{\mathrm{i}}(\omega, \tau)$ are obtained by convolving $\tilde{H}_{\mathrm{s}}^{(0)}(\omega, \tau)$ and $\tilde{H}_{\mathrm{i}}^{(0)}(\omega, \tau)$ with the Fourier transform of the time aperture function e^{-t^2/T^2}. In this way we can incorporate the effect of finite resolution on both the spectral code and imposition of signal-idler delay.

Experimentally, we take the same periodically repeated length-3 phase sequence as in one of our phase-only filtering results [Fig. 4.6(c)], but this time consider very narrow spectral chips. In order to correct for count-rate reduction due to alignment drift, we normalize each correlation function to a peak value of unity; since the time aperture term is equal to one at zero signal-idler delay, such renormalization has no effect on examination of aperture effects. In the first case, we program a chip

bandwidth of 16 GHz, for a total of 50 repetitions of the fundamental sequence over the 2.4-THz signal bandwidth; the measured correlation function is given in Fig. 4.7(a). Compared to the 160-GHz chip case in Fig. 4.6(c), the peak separation has been pushed from 2.1 to 21 ps, and the two side peaks are lowered slightly in relative intensity by the pulse-shaper time aperture. Further reductions are evident for even smaller chips; Fig. 4.7(b) shows the results for 9-GHz chips (total signal bandwidth 2.403 THz), while Fig. 4.7(c) shows those for 5-GHz chips (2.4-THz total signal bandwidth). We find that a value for T of 50 ps ($T_{\mathrm{FWHM}} = 58.9$ ps) gives good agreement with the observed peak reduction, as evident by the dotted theoretical curves in Fig. 4.7. This experimentally measured time aperture corresponds to a 3-dB spectral resolution of about 7.5 GHz, slightly better than the 10 GHz specified for the WaveShaper 1000S. From these results, it is clear that pulse-shaper resolution

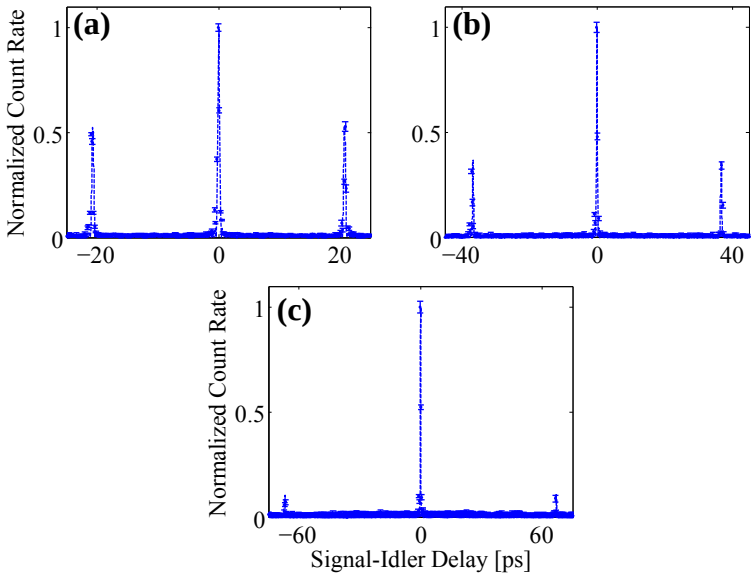

Fig. 4.7. Examination of pulse-shaper time aperture. Normalized coincidence rate for periodic repetitions of length-3 M-sequences with (a) 16-GHz chips, (b) 9-GHz chips, and (c) 5-GHz chips. The theoretical curves are obtained with $T = 50$ ps in Eq. (4.8).

limits the overall duration of the generated biphoton correlation function to a window of around 50 ps.

4.3 Outlook and Conclusion

We have experimentally implemented several techniques based on programmable spectral filtering with spatial light modulators for the generation of biphoton correlation trains. Amplitude filtering was first used to create an approximately comb-like spectrum, and accompanying this filter with appropriate quadratic spectral phase, we were able to demonstrate for the first time coherence revivals and repetition-rate multiplication through the biphoton temporal Talbot effect. Using a pulse shaper along with the continuous broadband spectrum from downconversion gives us the ability to programmably carve out combs with a wide range of linewidths and spacings, unlike those generated through cavity-based filtering. Subsequently we explored phase-only filtering to generate correlation trains with much greater efficiency over the amplitude filtering approach, useful when the temporal biphoton phase is of no concern. These demonstrated spectral filtering tactics could prove quite valuable in future work on periodic biphotons, especially where high speeds and tunability are advantageous. In particular, we will adopt the amplitude filtering approach for studies on phase coherence of biphoton frequency combs (see Chapter 5).

5. CHARACTERIZATION OF COHERENT BIPHOTON FREQUENCY COMBS USING ELECTRO-OPTIC PHASE MODULATION

5.1 Background

Defined earlier in Chapter 4, a biphoton frequency comb (BFC) or frequency-bin entangled photon pair is an entangled photon state occuring in a coherent superposition of discrete spectral mode pairs. In this context, *coherent superposition* implies that there is a fixed relationship between both amplitude and phase of the different comb line pairs [Fig. 5.1(a)]. To examine the coherence of a BFC, a straightforward approach would be through temporal correlation measurements: if the two-photon spectrum is a coherent comb with a flat spectral phase, the temporal correlation would consist of a train of evenly spaced narrow peaks [see Fig. 5.1(b)], which can be manipulated by adjusting the phase of different comb line pairs. In order to observe these features with a pair of single-photon detectors, the period of the correlation train would have to exceed the timing-jitter of the detectors; for example, a detection resolution of ~ 100 ps can only resolve the temporal structure of BFCs with a free spectral range (FSR) smaller than 10 GHz. And while nonlinear mixing techniques can be used for sub-picosecond resolution in coincidence measurements [13, 63, 105], diminishing nonlinear efficiency makes this approach impractical for narrow-linewidth entangled photons—the comb lines examined with sum-frequency generation in Chapter 4 had a linewidth of 250 GHz.

An alternative method to investigate the coherence of BFCs is by employing electro-optic phase modulation to mix comb lines, which can then reveal spectral phase sensitivity even with slow single-photon detectors. In Ref. [106], the authors

The results of this chapter have been published in Ref. [104].

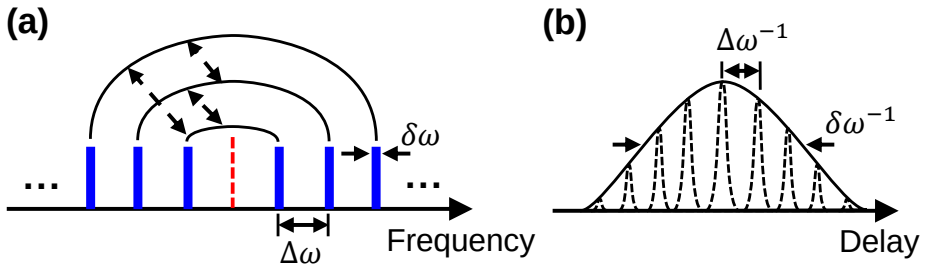

Fig. 5.1. Depiction of a biphoton frequency comb (BFC). (a) BFC spectrum; solid black lines represent frequency-mode correlations while dotted arrows portray fixed phase relationships between comb line pairs. (b) Time correlation function, with fast substructure arising from coherent interference between the different biphoton frequency components. If the phase between different biphoton frequency components is random, there will be no time-average interference, and we would get only the longer envelope.

used a pair of phase-modulators along with control of their modulation depths and relative phases to interfere biphotons, from which frequency entanglement was inferred; however, the input states to the "two-photon interferometer" had a continuous broadband spectrum and the notion of *frequency bins* was only implied from the application of narrow band spectral filters right before detection.

In this Chapter, we implement another phase-modulation scheme to demonstrate a proof-of-concept experiment, wherein our input states are BFCs obtained through spectral amplitude shaping of broadband biphotons; phase modulation in addition to spectral phase control enable us to observe high contrast interference fringes, a confirmation that the biphotons are indeed in a coherent superposition of frequency modes. Our frequency domain scheme is in close analogy with Franson interferometry [107], which has been widely applied in experiments on time-bin entangled photons [108–110].

5.2 Theory

The state of a BFC can be written as

$$\begin{aligned} |\Psi\rangle &= \sum_{k=1}^{d} \alpha_k |k\rangle_{\mathrm{s}} |k\rangle_{\mathrm{i}} \\ |k\rangle_{\mathrm{s}} |k\rangle_{\mathrm{i}} &= \int d\Omega\, \phi(\Omega - k\Delta\omega, \Omega + k\Delta\omega)\, |\omega_0 + \Omega\rangle_{\mathrm{s}} |\omega_0 - \Omega\rangle_{\mathrm{i}} \end{aligned} \tag{5.1}$$

where $|k\rangle_{\mathrm{s}}|k\rangle_{\mathrm{i}}$ indicates the k^{th} comb line pair of the signal and idler spectrum, α_k is a complex number representing the joint amplitude and phase of the k^{th} comb line pair, $\phi(\omega_{\mathrm{s}}, \omega_{\mathrm{i}})$ is the lineshape of an energy-matched comb tooth pair, $\Delta\omega$ is the FSR, d is the number of comb tooth pairs, and $\omega_0 = 2\pi f_0$ is the center frequency of the biphoton spectrum.

Applying phase modulation of the form $e^{i\delta \sin \omega_{\mathrm{m}} t}$ (ω_{m} is the modulation frequency and δ is the modulation depth) to a comb line projects it into sidebands offset from the original comb line by integer multiples of ω_{m} [111]—the positive-integer multiples correspond to upshifts in frequency while those of the negative-integers correspond to frequency downshifts. Thus, for a single comb line, we choose to describe the effect of phase modulation on the the k^{th} frequency mode if in the signal or idler spectrum by

$$\hat{m}_{\mathrm{s}} |k\rangle_{\mathrm{s}} = \sum_{n=-\infty}^{\infty} C_n \left| k + \frac{n\omega_{\mathrm{m}}}{\Delta\omega} \right\rangle_{\mathrm{s}} \tag{5.2}$$

or

$$\hat{m}_{\mathrm{i}} |k\rangle_{\mathrm{i}} = \sum_{m=-\infty}^{\infty} C_m \left| k - \frac{m\omega_{\mathrm{m}}}{\Delta\omega} \right\rangle_{\mathrm{i}} \tag{5.3}$$

respectively, where $C_{n,m} = J_{n,m}(\delta)$ is the Bessel function of the first kind and $J_{-n} = \mathrm{e}^{in\pi} J_n$. When normalized, C_n represents the probability amplitude of the n^{th} sideband after phase modulation. Consequently, the projection state of the k^{th} biphoton mode after phase modulation of the signal and idler can be written as:

$$\hat{m}_{\mathrm{s}} \hat{m}_{\mathrm{i}} |k\rangle_{\mathrm{s}} |k\rangle_{\mathrm{i}} = \sum_{n=-\infty}^{\infty} \sum_{m=-\infty}^{\infty} C_n C_m \left| k + \frac{n\omega_{\mathrm{m}}}{\Delta\omega} \right\rangle_{\mathrm{s}} \left| k - \frac{m\omega_{\mathrm{m}}}{\Delta\omega} \right\rangle_{\mathrm{i}} \tag{5.4}$$

From this we glean that the phase modulation process on the biphoton comb introduces new spectral correlations. Therefore, if we project different comb line pairs into sidebands and select only overlapping sideband modes in the signal and idler spectrum, the emerging two-photon state would be in a superposition of indistinguishable frequency mode pairs. We can then examine the coherence of the biphoton comb through the second-order cross-spectral density, which gives the probability of detecting the signal photon in mode k and the idler photon in mode k' [31, 112]

$$\Theta^{(2)}(k_{\mathrm{s}}, k_{\mathrm{i}}') = |\langle \mathrm{vac}|\hat{a_{k_{\mathrm{s}}}}\,\hat{a_{k_{\mathrm{i}}'}}|\Psi\rangle|^2 \tag{5.5}$$

As an example, let us consider entangled photons consisting of two comb line pairs:

$$|\Psi\rangle = \alpha_k|k\rangle_{\mathrm{s}}|k\rangle_{\mathrm{i}} + \alpha_{k+1}|k+1\rangle_{\mathrm{s}}|k+1\rangle_{\mathrm{i}} \tag{5.6}$$

If we apply phase modulation with $\omega_m = \Delta\omega/2$ and consider just the first modulation sidebands ($n, m = \pm 1$), the biphoton state would be modified as follows:

$$\begin{aligned}
\hat{m}_{\mathrm{s}}\hat{m}_{\mathrm{i}}|\Psi\rangle = {} & \alpha_k C_1 C_1 \Big|k+\frac{1}{2}\Big\rangle_{\mathrm{s}}\Big|k-\frac{1}{2}\Big\rangle_{\mathrm{i}} + \alpha_k C_1 C_{-1}\Big|k+\frac{1}{2}\Big\rangle_{\mathrm{s}}\Big|k+\frac{1}{2}\Big\rangle_{\mathrm{i}} \\
& + \alpha_k C_{-1} C_1 \Big|k-\frac{1}{2}\Big\rangle_{\mathrm{s}}\Big|k-\frac{1}{2}\Big\rangle_{\mathrm{i}} + \alpha_k C_{-1} C_{-1}\Big|k-\frac{1}{2}\Big\rangle_{\mathrm{s}}\Big|k+\frac{1}{2}\Big\rangle_{\mathrm{i}} \\
& + \alpha_{k+1} C_1 C_1 \Big|k+\frac{3}{2}\Big\rangle_{\mathrm{s}}\Big|k+\frac{1}{2}\Big\rangle_{\mathrm{i}} + \alpha_{k+1} C_1 C_{-1}\Big|k+\frac{3}{2}\Big\rangle_{\mathrm{s}}\Big|k+\frac{3}{2}\Big\rangle_{\mathrm{i}} \\
& + \alpha_{k+1} C_{-1} C_1 \Big|k+\frac{1}{2}\Big\rangle_{\mathrm{s}}\Big|k+\frac{1}{2}\Big\rangle_{\mathrm{i}} + \alpha_{k+1} C_{-1} C_{-1}\Big|k+\frac{1}{2}\Big\rangle_{\mathrm{s}}\Big|k+\frac{3}{2}\Big\rangle_{\mathrm{i}}
\end{aligned} \tag{5.7}$$

Now when we select only the sidebands that are in-between k and $k+1$, the output biphoton state will become a superposition of identical frequency modes:

$$|\Psi_{\mathrm{out}}\rangle = \Big(\alpha_k C_1 C_{-1} + \alpha_{k+1} C_{-1} C_1\Big)\Big|k+\frac{1}{2}\Big\rangle_{\mathrm{s}}\Big|k+\frac{1}{2}\Big\rangle_{\mathrm{i}} \tag{5.8}$$

Yet if the biphoton comb is coherent, there will be two-photon interference in the second-order cross-spectral density,

$$\Theta^{(2)}\Big(k+\frac{1}{2}, k+\frac{1}{2}\Big) = \Big|C_1 C_{-1}\Big(\alpha_k + \alpha_{k+1}\Big)\Big|^2 \tag{5.9}$$

which we can observe by manipulating the phases of α_k and α_{k+1}.

5.3 Experimental Demonstration

Our experimental setup is presented in Fig. 5.2(a). We pump a 67-mm-long periodically poled lithium niobate waveguide with a continuous-wave laser at 771 nm in order to generate broadband biphotons centered around 1542 nm (194.55 THz). Figure 5.2(b) shows a conceptual picture of the broadband biphoton spectrum generated through spontaneous parametric downconversion; the signals are defined as photons in the higher frequency band while the lower-frequency photons are called idlers. After filtering out the pump photons, we couple the signal and idler photons into a commercial pulse shaper (pulse shaper 1, Finisar WaveShaper 1000S). Using pulse shaper 1, we carve the continuous broadband spectrum into a BFC with a linewidth of 12 GHz and an FSR of 36 GHz ($\Delta\omega/2\pi$) [Fig. 5.2(c)]. Pulse shaper 1 is also used to attenuate comb lines when necessary to ensure the amplitude equalization required for maximally entangled states [16], as well as applying spectral phase patterns to the signal and idler comb lines during measurements. Next, the BFC is sent into a phase modulator (EOSpace PM-5K4-20-PFU-PFU-UV) driven by an 18-GHz sinusoidal waveform from a radio frequency (rf) oscillator (Agilent Technologies E8257D) to create sidebands at integer multiples of 18 GHz [Fig. 5.2(d)]—18 GHz is chosen for the phase modulator as it is one-half the FSR of the BFC—and we can adjust the magnitude of each sideband projection by tuning the rf power to control the modulation depth. We then send the phase-modulated BFC into another pulse shaper (pulse shaper 2, Finisar WaveShaper 4000s), with which we pick out only overlapped sidebands that consist of projections from different signal and idler comb lines [Fig. 5.2(e)]. The selected sidebands from the signal and idler halves are sent to a pair of gated InGaAs single-photon detectors (Aurea SPD_AT_M2) and an event timer (PicoQuant HydraHarp 400) is used to record coincidences occuring in a 0.5 ns window—we chose 0.5 ns to speed up our measurement acquisition time while maintaining sufficient coincidence-to-accidental ratios.

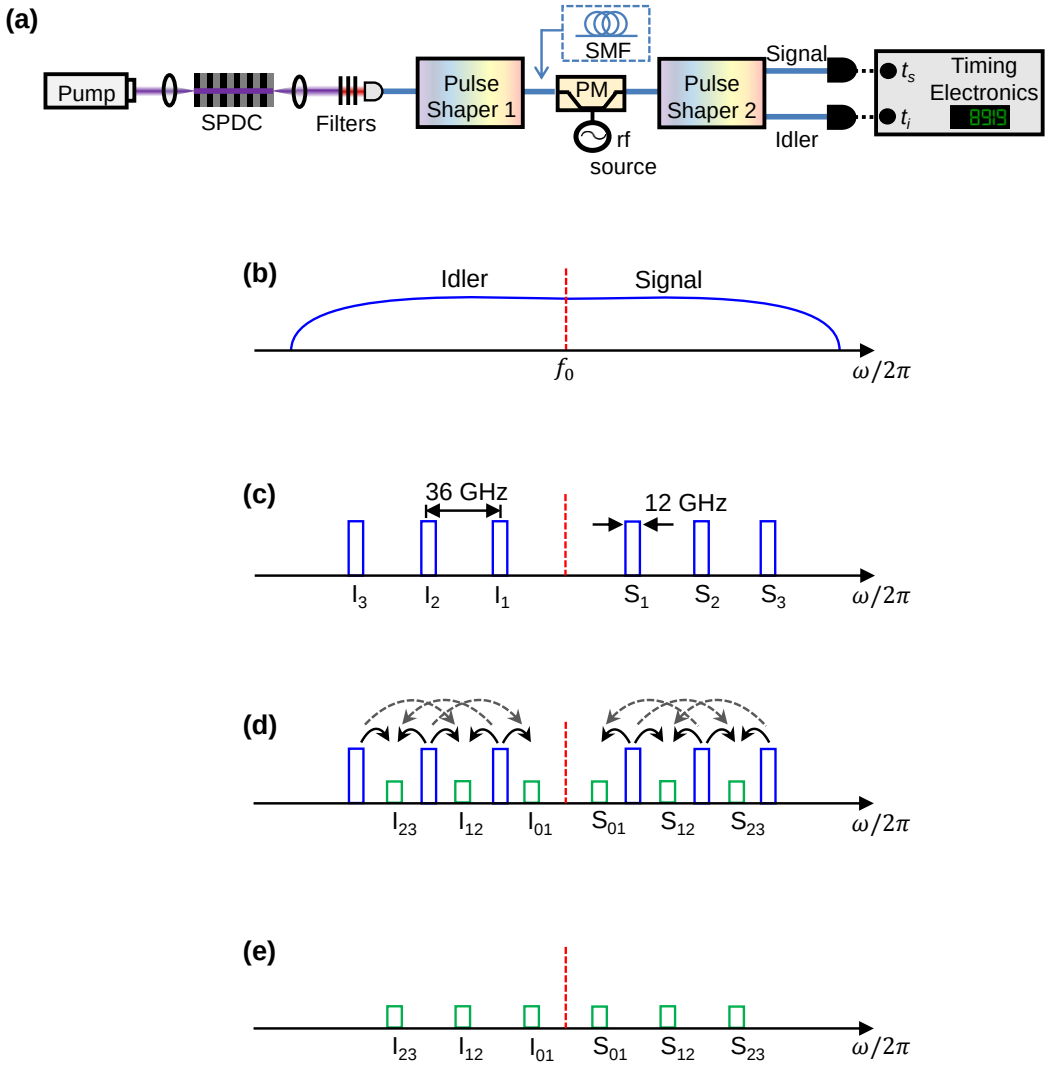

Fig. 5.2. Basic schematic for phase coherence measurements and illustration of biphoton spectral progression at different steps. (a) Experimental setup. (b) Broadband continuous biphoton spectrum. (c) Biphoton frequency comb after carving continuous spectrum with pulse shaper 1. The blocked frequencies were attenuated by 60 dB, making contamination from undesired frequencies negligible. (d) Sidebands projected from phase modulation of comb lines. (e) Using pulse shaper 2, selected sidebands are routed to a pair of single-photon detectors. SPDC: spontaneous parametric downconversion; PM: phase modulator; rf: radio frequency.

5.3.1 Two-Dimensional Frequency-Bin Entanglement

For our first demonstration, we create two comb line pairs, S_1I_1 and S_2I_2, while ensuring that the pairs contribute equal amplitudes ($|\alpha_1|^2 = |\alpha_2|^2$) by measuring coincidences between S_1 and I_1, and S_2 and I_2. We also apply a phase of $\varphi/2$ to both S_2 and I_2, giving a total relative phase of φ on S_2I_2 with respect to S_1I_1—see illustration in Fig. 5.3(a). Then we drive the phase modulator with an rf power such that the frequency projection is mostly dominated by the first phase modulation sidebands, giving us $|C_{\pm1}|^2 = 0.32$ (the amplitude of each sideband is obtained by

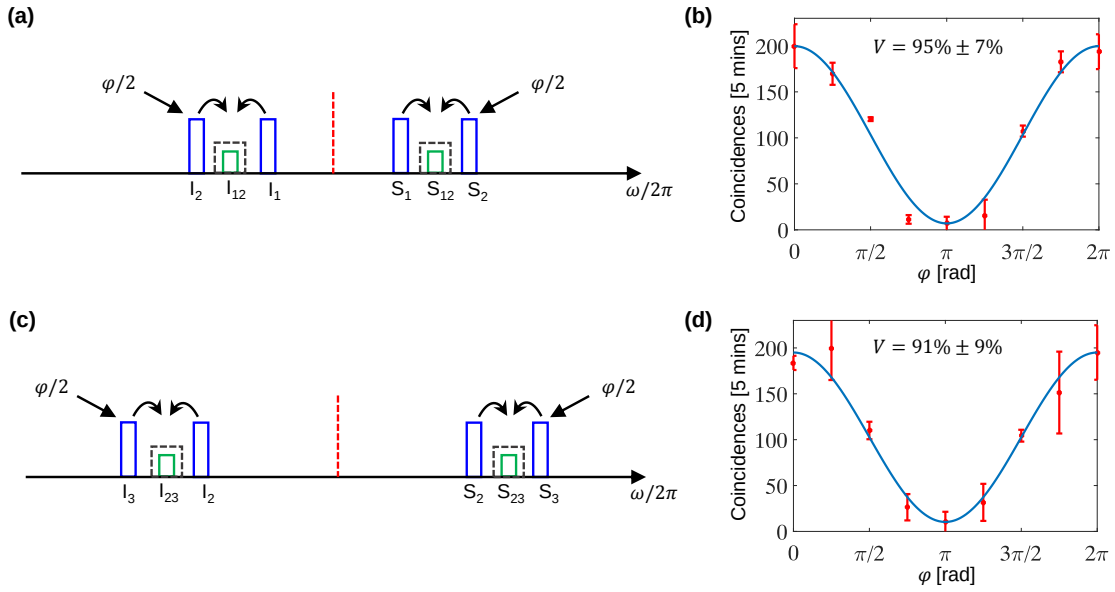

Fig. 5.3. Frequency-bin entanglement with 2 comb line pairs. Illustration of selected sidebands originating from phase modulation of parent comb line pairs (a) S_1I_1 and S_2I_2, (c) S_2I_2 and S_3I_3. The two-photon interference as a result of applying (b) φ relative phase on S_2I_2 with respect to S_1I_1, (d) φ relative phase on S_3I_3 with respect to S_2I_2. The red error bars are the standard deviation of three measurements for each phase value and the blue curves indicate the theoretical predictions taking into account the visibility calculated from the maximum and minimum data points. The coincidence-to-accidental ratio in our measurements was 3, but accidentals were subtracted here and in subsequent plots.

sending a continuous-wave laser through the phase modulator and measuring the output using an optical spectrum analyzer). After phase modulation, we pick out the overlapped sidebands—S_{12} halfway between S_1 and S_2, and I_{12} in the middle of I_1 and I_2. Sweeping φ from 0 to 2π and recording the coincidence rates, we obtain a sinusoidal interference pattern with a visibility of $95\% \pm 7\%$, shown in Fig. 5.3(b). The pattern matches our expectation from theory, $\Theta^{(2)}(\frac{3}{2}, \frac{3}{2}) \sim 1 + \cos\varphi$, using Eq. 5.9 with $\alpha_2 = e^{i\varphi}\alpha_1$.

Similarly, we repeated the experiment using comb line pairs S_2I_2 and S_3I_3, and picked out the overlapped sidebands in-between them ($S_{23}I_{23}$) [Fig. 5.3(c)]; the resulting interference pattern with a visibility of $91\% \pm 9\%$ is shown in Fig. 5.3(d). Thus we can confirm frequency-bin entanglement for the utilized $d = 2$ states since the visibilities exceed 71% [109]. Here we also note that the constructive and destructive interference points occur at $\varphi = 0$ and $\varphi = \pi$ respectively, suggesting that $\alpha_1 \approx \alpha_2 \approx \alpha_3$.

5.3.2 Three-Dimensional Frequency-Bin Entanglement

To explore $d = 3$ frequency-bin entanglement, we utilize all three of the comb line pairs, S_1I_1, S_2I_2, and S_3I_3 (setting $|\alpha_1|^2 = |\alpha_2|^2 = |\alpha_3|^2$). After phase modulation, we again pick out the sidebands S_{12} and I_{12}, but in this case, S_{12} consists of the sideband projections $n = 1, -1, -3$ from S_1, S_2, S_3, and $m = -1, 1, 3$ from I_1, I_2, I_3, respectively, as shown in Fig. 5.4(a). We ensure that the magnitude of the first and third sidebands are equal by adjusting the rf power to give us $C_1 = -C_{-1} = C_3 = -C_3$, and we measured $|C_1|^2$ to be 0.16. Now by applying a phase of 0 to comb line pair S_1I_1, φ to S_2I_2, and 2φ to S_3I_3, the cross-spectral density for the selected sidebands (S_{12} and I_{12}) can be written as:

$$\Theta^{(2)}\Big(\frac{3}{2}, \frac{3}{2}\Big) = \Big|\alpha_1 C_1 C_{-1} + \alpha_2 C_{-1} C_1 e^{i\varphi} + \alpha_3 C_{-3} C_3 e^{i2\varphi}\Big|^2 \tag{5.10}$$

and if $\alpha_1 = \alpha_2 = \alpha_3$, Eq. 5.10 can be simplified further to give

$$\Theta^{(2)}\Big(\frac{3}{2}, \frac{3}{2}\Big) = \Big|\alpha_1 {C_1}^2\Big(1 + e^{i\varphi} + e^{i2\varphi}\Big)\Big|^2 \tag{5.11}$$

The result obtained after sweeping φ from 0 to 2π is presented in Fig. 5.4(b). Since we have contributions from three pairs of comb lines, the features of the interference pattern are now sharper compared to those observed in the Figs. 5.3(b) and 5.3(d); this sharpening is analogous to the sharpening of the pulses in a mode-locked laser as more frequency lines are added. We calculate a visibility of $90\% \pm 6\%$, which is sufficient to prove entanglement between our entangled qutrits ($d = 3$) since it is higher than the three-dimensional classical visibility threshold of 77.5% [109].

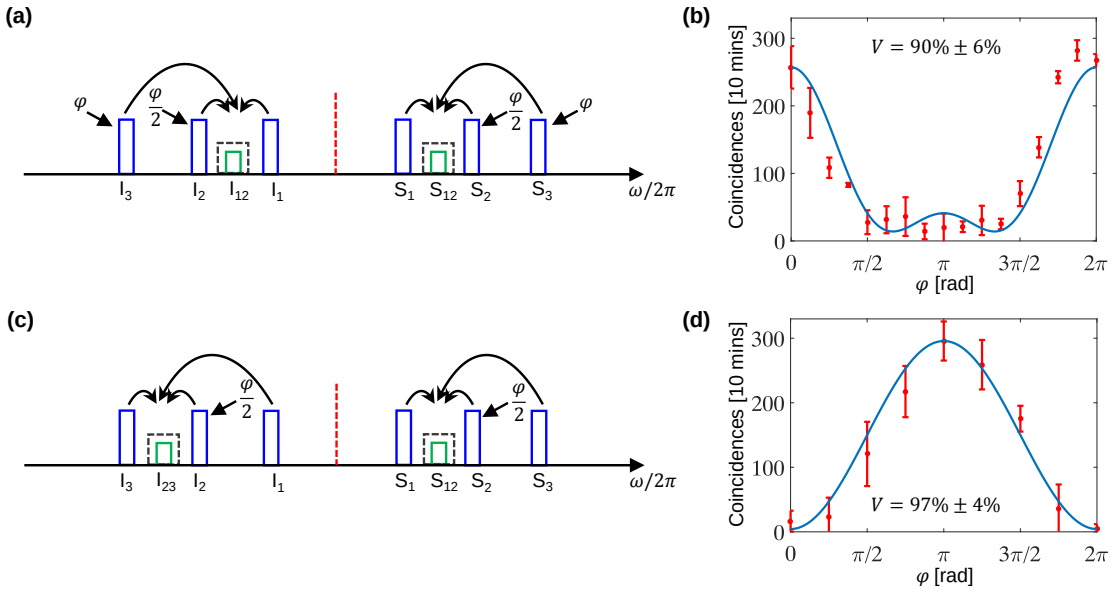

Fig. 5.4. Frequency-bin entanglement with 3 comb line pairs. (a) and (c) Illustration of selected sidebands arising from phase modulation of parent comb line pairs S_1I_1, S_2I_2 and S_3I_3. In (c), the sideband amplitudes are set with the phase modulator such that $|C_3| = \frac{|C_1|}{2}$. The two-photon interference as a result of applying (b) φ phase on S_2I_2 and 2φ on S_3I_3, with respect to S_1I_1, (d) φ relative phase on S_2I_2 with respect to S_1I_2 and S_1I_2. The red error bars are the standard deviation of three measurements for each phase and the blue curves indicate the theoretical predictions taking into account the visibility calculated from the maximum and minimum data points.

We can also manipulate the coincidence pattern resulting from the interference of three comb line pairs by looking at sidebands projected to other frequency locations as well as applying different phase configurations to the comb lines. Here we examine asymmetric sidebands, S_{12} and I_{23}, containing contributions from the $n = 1,\ -1,\ -3$ sidebands of $S_1,\ S_2,\ S_3$, and $m = -3,\ -1,\ 1$ sidebands of $I_1,\ I_2,\ I_3$, respectively—see Fig. 5.4(c). Again, we set $\alpha_1 = \alpha_2 = \alpha_3$, but now we tune the rf power such that $|C_3| = \frac{|C_1|}{2}$ and then we apply a phase of φ to S_2I_2. The cross-spectral density for the selected state is

$$\Theta^{(2)}\Big(\frac{3}{2},\frac{5}{2}\Big) = \Big|\alpha_1 C_1 C_{-3} + \alpha_2 C_{-1} C_{-1} e^{i\varphi} + \alpha_3 C_{-3} C_1\Big|^2 \tag{5.12}$$

which can be reduced to

$$\Theta^{(2)}\Big(\frac{3}{2},\frac{5}{2}\Big) = \Big|\alpha_1 {C_1}^2\Big(\frac{1}{2} - e^{i\varphi} + \frac{1}{2}\Big)\Big|^2 \tag{5.13}$$

since $C_{-1} = -C_1$ and $C_{-3} = -C_3$. Yet again we observe a sinusoidal interference pattern [Fig. 5.4(d)] when we sweep φ from 0 to 2π, in agreement with theory—using Eq. 5.13, $\Theta^{(2)}(\frac{3}{2},\frac{5}{2}) \sim 1 - \cos\varphi$.

5.3.3 Dispersion Measurement

The versatility of our experimental technique facilitates the measurement of dispersion using entangled photons. We insert some SMF-28e fiber before pulse shaper 1 to induce dispersion on the biphotons [Fig. 5.2(a)]—the dispersion of this fiber around 1550 nm (extracted from the datasheet) is $D = 16.2\,\mathrm{ps/(nm\ km)}$ and $\beta_2 = -D\lambda^2/2\pi c = -2.06 \times 10^{-2}\,\mathrm{ps^2/m}$ [57]. Now we revisit the $d = 2$ interference results shown in Fig 5.3, and described by Eq. (5.9). Fiber dispersion will impart an additional relative phase on the $(k+1)^{\mathrm{th}}$ bin with respect to the k^{th}, and this will lead to a phase shift in the interference pattern. The phase shift is given by

$$\begin{aligned} \varphi_{\mathrm{shift}} &= -(2\pi)^2 \beta_2 l[(f_{\mathrm{os}} + \Delta f)^2 - f_{\mathrm{os}}^2] \\ &= -(2\pi)^2 \beta_2 l \Delta f (2 f_{\mathrm{os}} + \Delta f) \end{aligned} \tag{5.14}$$

where l is the fiber length, $\Delta f = \Delta\omega/2\pi$ is the FSR in Hz, $f_{\text{os}} = k\Delta f$ is the frequency difference between the k^{th} frequency bin and the center frequency, and we have assumed the dominant dispersion is the quadratic spectral phase term. (Unlike the classical term, a factor of 1/2 is dropped in Eq. 5.14 since the total phase shift is equal to the sum of relative phase shifts in the signal and idler comb lines.)

As an initial experimental test, we use a fiber length of 200 m and select comb line pairs S_5I_5 and S_6I_6. Similar to previous measurements, after phase modulation, we pick out the sidebands S_{56} between S_5 and S_6, and I_{56} between I_5 and I_6, and then record the second-order cross-spectral density as we sweep the applied φ phase on S_5I_5 from 0 to 2π. The result, given in Fig. 5.5(a), shows a sinuosidal interference pattern albeit shifted by a phase of 0.74π, in excellent agreement with theory (using Eq. 5.14 with $k = 5$ and $\Delta f = 36$ GHz).

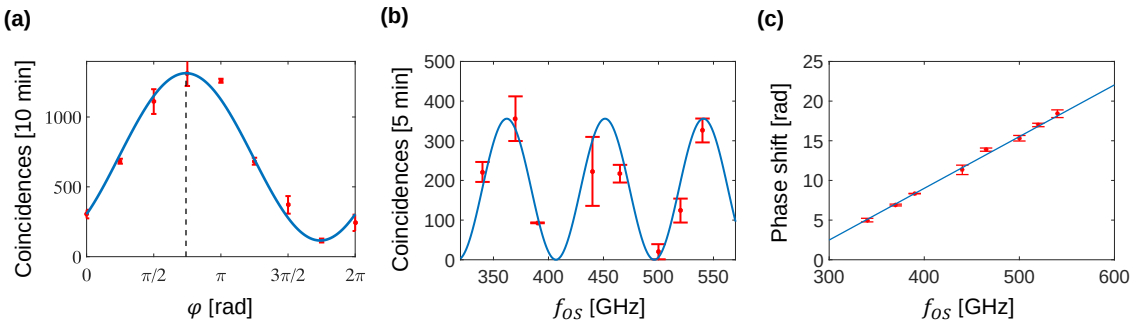

Fig. 5.5. (a) Shift in the interference pattern as a result of added dispersion from a 200-m-long fiber; the dashed vertical line indicates a relative shift of $\varphi = 0.74\pi$. The blue curve indicates the theoretical prediction taking into account the visibility calculated from the maximum and minimum data points.(b) Coincidences as a function of f_{os} when a 1.1-km-long fiber is introduced into the setup, while the pulse shaper does not apply any relative phase between frequency bin pairs. The blue curve is the theoretical prediction normalized to the maximum number of coincidence counts. (c) Deduced phase shift as a function of f_{os}. The blue line is the linear fit to the data points. The red error bars are the standard deviation of three measurements.

For a complete frequency-dependent phase shift measurement, we replace the 200-m-long fiber with another fiber, 1.1 km long. However, rather than sweep φ for various frequency bin pairs, we set it to zero and only register the coincidence counts as a function of f_{os} [Fig. 5.5(b)]. We then compute the phase shift for each f_{os} by comparing its corresponding coincidence counts $C(f_{\mathrm{os}})$ to the expected maximum number of coincidences C_{max}. (By measuring identical single photon count rates in the selected frequency bins, we ensured that C_{max} was constant as a function of f_{os}.) The phase shift will be given by $C(f_{\mathrm{os}}) = \frac{C_{\mathrm{max}}}{2}[1 + \cos(\varphi_{\mathrm{shift}})]$, which we can unwrap to obtain the linear plot in Fig. 5.5(c). From Fig. 5.5(c), β_2 can be retrieved by calculating the slope of the curve (derivative of φ_{shift} with respect to f_{os} in Eq. 5.14). We obtain a value of $\beta_2 = (-2.030 \pm 0.013) \times 10^{-2}\,\mathrm{ps}^2/\mathrm{m}$, not far off the $-2.06 \times 10^{-2}\,\mathrm{ps}^2/\mathrm{m}$ expected for SMF-28e fiber.

5.4 Outlook and Conclusion

In conclusion, we have demonstrated a technique for verifying phase coherence in BFCs. The attributes of this approach, in which we mix adjacent frequency bins, are analogous to those of Franson interferometry, which mixes entangled photon time bins. Equivalently, our approach provides a straightforward path to prove frequency-bin entanglement; we presented interference patterns with visibilities higher than the classical threshold for entangled qubit and qutrit states. Additionally, our dispersion measurements suggest the potential of low-light dispersion measurement with biphoton frequency combs.

While the work discussed in this chapter was conducted using relatively wide frequency bins (12 GHz) carved out of a continuous-broadband spontaneous parametric downconversion spectra, we have also explored a similar experimental setup for narrow linewidth comb line pairs generated through spontaneous four-wave mixing in an on-chip silicon nitride microring resonator [113]. In parallel, Kues *et al.* [83] conducted similar studies using a microring resonator fabricated from a high refractive

index glass. These two works were the first reported verification of high-dimensional frequency-bin entanglement from an on-chip source, showing the potential of chip-scale devices for quantum information processing. Our results in conjunction with those based on spontaneous four-wave mixing signify the universality of this approach for characterizing frequency-bin entanglement.

6. MODULATION TECHNIQUE FOR IMPROVING TEMPORAL RESOLUTION IN BIPHOTON COINCIDENCE MEASUREMENTS

6.1 Background

In the previous chapters, we highlighted that the relative timing between a pair of broadband entangled photons can be useful for a variety of quantum information technologies, and all of our experiments so far have involved temporal correlation measurements. The most straightforward method used to obtain the temporal correlation of entangled photons involves coincidence measurements between a pair of single-photon detectors. However, standard single-photon avalanche photodiodes (SPADs) suffer from large timing jitters—typically on the order of several hundreds of picoseconds. Even at best, jitters only around a few tens of picoseconds have been realized, either with optimized Si photon counters for visible light [115] or superconducting nanowire detectors at telecom wavelengths [116, 117]. If well chosen, microwave solutions can furnish substantial speed improvements over direct detection with standard SPADs. While not as fast as nonlinear optical techniques such as entangled-photon mixing [13, 18, 118–120], short-pulse upconversion [105, 121], and time-to-frequency conversion [122, 123], electronics does benefit from robustness and simplicity, providing a bridge between slow (but straightforward) direct detection and ultrafast (but elaborate) nonlinear optical processing.

A concrete example of such intermediary microwave processing of quantum light was developed [111] and demonstrated [21] by Harris and colleagues. Each photon from an entangled pair is separately propagated through sinusoidal intensity modulation; then coincidences between the two outputs are measured with slow integrating

The results of this chapter have been published in Ref. [114].

detectors. By maintaining phase synchronization as the modulation frequency is swept, it is possible to extract the Fourier spectrum of the Glauber correlation function $G^{(2)}(\tau)$. The maximum measurable bandwidth is then limited not by detector jitter, but rather the speed of the electro-optic modulators. Although the first proof-of-principle experiment considered frequencies up to only 30 MHz [21], state-of-the art 100-GHz modulators [124] could in theory resolve temporal features shorter than 5 ps. And unlike Hong-Ou-Mandel interference—which can indeed provide a measure of ultrafast biphoton synchronization without nonlinear optics [albeit not of $G^{(2)}(\tau)$ directly] [125]—the photons need not mix spatially, making this approach consistent with nonlocal detection as well.

We extend on Harris's work, proposing and experimentally demonstrating a new technique for biphoton measurement based on high-speed electro-optic intensity modulation with arbitrary microwave waveforms. Our measurements are found to be related to the modulators' temporal cross-correlation, with periodic revivals controlled by the repetition rate. Moreover, by propagating the biphoton through various lengths of optical fiber, we demonstrate sensitivity to temporal spreading and shifting beyond the capabilities of our SPADs. Thus our approach makes use of temporal cross-correlation rather than Fourier transformation to resolve fast features, and we expect the idea to contribute in characterization of high-speed quantum information-processing systems.

6.2 Theory

To theoretically describe our modulation procedure, we consider an input correlation function $G^{(2)}_{\mathrm{in}}(t_2, t_1) = G^{(2)}_0(t_2 - t_1)$, which when properly normalized gives the probability density for joint detection of the signal photon at time t_1 and the idler at time t_2. We have assumed a monochromatic pump, so that the temporal correlations depend only on the difference $t_2 - t_1$. Applying T-periodic intensity modulation functions, $M_{\mathrm{s}}(t_1 + \tau) = |m_{\mathrm{s}}(t + \tau)|^2$ to the signal and $M_{\mathrm{i}}(t_2) = |m_{\mathrm{i}}(t_2)|^2$ to the idler

photons, where τ is a tunable time shift, modifies the biphoton wavepacket (as described in Section 1.3) such that the resulting temporal correlation can be written as

$$G^{(2)}_{\text{out}}(t_2, t_1) = G^{(2)}_{\text{in}}(t_2, t_1)\, M_{\text{s}}(t_1 + \tau)\, M_{\text{i}}(t_2). \tag{6.1}$$

The measured coincidence rate follows by summing all joint photon detections within some time window Δ. Integrating Eq. 6.1, we arrive at the coincidence rate,

$$R_{\text{c}}(\tau) = \int_{-\infty}^{\infty} dt_1 \int_{t_1-\Delta}^{t_1+\Delta} dt_2 G^{(2)}_0(t_1 - t_2)\, M_{\text{s}}(t_1 + \tau)\, M_{\text{i}}(t_2). \tag{6.2}$$

Following a development similar to that in [21], we can simplify further to arrive at the final coincidence rate:

$$R_c(\tau) = K \int_{-\infty}^{\infty} dt\, G^{(2)}_0(t) \gamma_{\text{si}}(t + \tau), \tag{6.3}$$

where K is a constant, and

$$\gamma_{\text{si}}(t) = \int_{t_0}^{t_0+T} dx\, M_{\text{s}}(x + t) M_{\text{i}}(x) \tag{6.4}$$

is the circular intensity correlation between the two modulators. In this way we see that the modulator cross-correlation supplants any detector characteristics in the overall temporal response function, and we observe two important limiting cases.

1. When the initial correlation function $G^{(2)}_0(t)$ is much narrower than $\gamma_{\text{si}}(t)$, we recover $R_{\text{c}}(\tau) \propto \gamma_{\text{si}}(\tau)$; that is, the coincidence pattern reflects the modulator cross-correlation.

2. On the other hand, when the modulators are much faster than $G^{(2)}_0(t)$, the coincidence rate becomes $R_{\text{c}}(\tau) \propto G^{(2)}_0(-\tau)$ for $\tau \in (-\frac{T}{2}, \frac{T}{2})$, assuming a modulator period much longer than the biphoton correlation time.

This second case is the motivation for our method, revealing how electro-optic modulation can recover photon correlations too fast for the available SPADs. Both extremes are considered in the experiments below, although we employ the more precise Eq. 6.3 in all theoretical curves rather than these approximations.

6.3 Experimental Demonstration

To explore these ideas experimentally, we utilize the setup in Fig. 6.1. We generate entangled photons with a photon flux estimated as $\sim 10^8$/s, corresponding to a pair occupation probability of about 0.1 per 1-ns coincidence window used below; this reduces the effects of multipair emission and ensures we are operating in the single-photon detection regime. The biphotons are coupled into fiber and separated using a 50/50 fiber beam splitter; with 50% probability, the photons in a given pair will exit along separate paths and can contribute to coincident arrivals. An electronic arbitrary waveform generator (Tektronix AWG7122B) provides the desired 20-GS/s microwave drive signal, which is then split, amplified, and applied to each intensity modulator (EOSpace AX-0K5-10-PFU-PFU-UL). A series of microwave delay stages precedes the electrical input of the signal modulator in order to control the relative delay τ. The modulated photons are then detected by a pair of gated InGaAs SPADs (Aurea SPD_AT_M2), and coincidences within a 1-ns window are determined by an event timer. The modulation speed is limited by the bandwidths of the waveform generator (7.5 GHz) and the modulators themselves (10 GHz). Although sufficient for an initial experiment, significantly faster modulation could be realized with, e.g., 100-GHz modulators and photonically generated drive signals [126, 127].

As a first test, we drive each modulator with a length-4 sequence consisting of one high and three low voltages. In practice, imperfections in the waveform generator limit the purity of the applied modulation, and the modulator bandwidth reduces the extinction ratio. Figure 6.2(a) shows the experimental modulator functions $M_{\mathrm{s}}(t)$ (signal) and $M_{\mathrm{i}}(t)$ (idler), obtained by sending a continuous-wave laser through each and measuring the temporal response with an analog photodiode and sampling oscilloscope. In order to give the most accurate measure of the optical throughput, we average 2000 traces and remove the combined impulse response of the photodiode and oscilloscope through deconvolution. (The exact form of the impulse response was previously obtained by exciting the diode with $\sim$100-fs laser pulses and record-

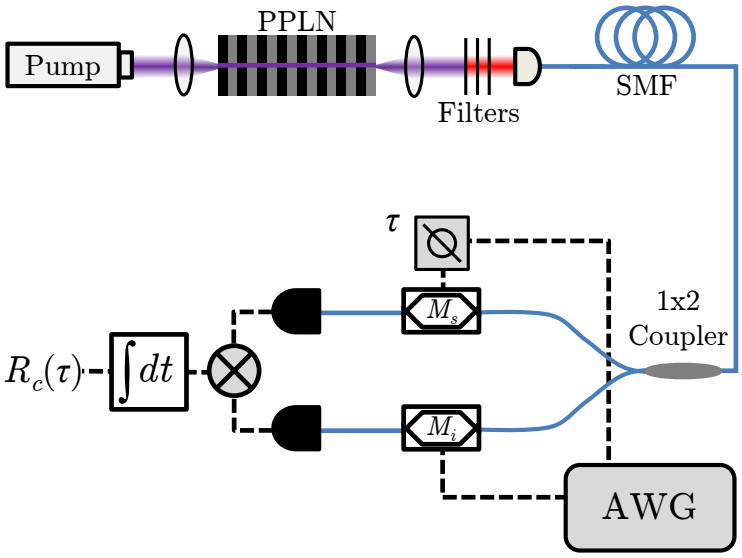

Fig. 6.1. Experimental setup. Entangled photons are generated in the process of SPDC in a PPLN waveguide, coupled into optical fiber, and separated with a fiber beam splitter. Signal and idler then experience intensity modulation, and coincidences are recorded as the timing of the signal modulation is swept. SMF: single-mode fiber; AWG: arbitrary waveform generator.

ing the electrical output, showing a full-width at half-maximum of 18.2 ps.) With these patterns applied, we then send entangled photons through each modulator and measure the coincidence rate as the delay of the drive signal to M_s is shifted. The precise value of the delay τ (apart from an unimportant overall offset) is determined by tapping off a portion of the time-shifted signal and observing its relative position on an oscilloscope. The coincidence results are presented in Fig. 6.2(b), normalized to idler detections in order to partially compensate for power fluctuations over the course of the measurement; thus the values along the y-axis provide an estimate of the linear transmissivity of the system, including coupling and detection efficiencies. Each data point is the mean of five 120-s acquisitions, with error bars giving the standard deviation. Accidentals are determined by measuring coincidences when the two detector gates are temporally mismatched; these are subtracted off in the results

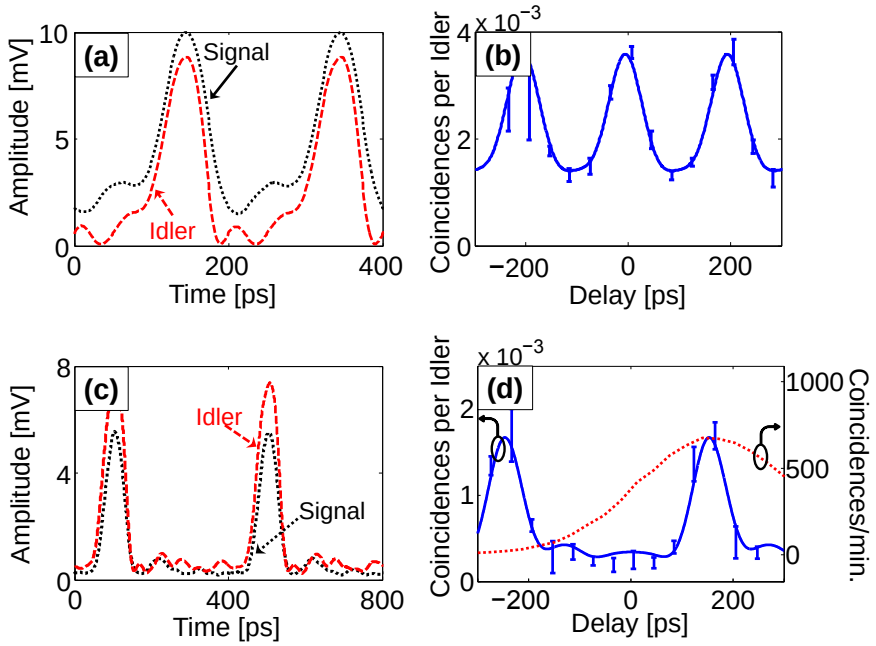

Fig. 6.2. Coincidence measurements with pulse-like modulation. (a) Modulation functions and (b) corresponding coincidence rate when a 25%-duty-cycle sequence is applied by waveform generator. (c) Intensity modulation and (d) associated coincidence rate for 12.5%-duty-cycle pattern. For comparison, the red dotted curve in (d) gives the measured coincidence spread when the modulators are bypassed and the photons are detected directly, binned into 32-ps time slots. For the modulation results in (b) and (d) (left axis), error bars show experimental results; solid curves give theoretical predictions.

of Fig. 6.2(b). The solid curve gives the theoretical prediction utilizing the measured modulator functions and accounting for dispersive spreading of the biphoton in the short fiber leads, with the time origin and amplitude as the only adjustable parameters. Excellent agreement between theory and experiment is observed. The full width at half maximum (FWHM)—after removing the background—is 73.4 ps, dominated by the modulator correlation time rather than that of the biphoton itself, which for the $\sim$7 m of fiber used is estimated at around 10 ps.

The contrast of 2.7:1 in Fig. 6.2(b) is limited by both the modulation bandwidth and imperfect extinction. So for improved visibility, we increase the sequence length

to eight by adding four more zero samples; this doubles the period while maintaining the same pulse width as before. These new modulation functions are plotted in Fig. 6.2(c), and the results of a coincidence measurement in Fig. 6.2(d) (left axis). We have again subtracted accidentals and included the theoretical prediction as a solid line. Sharp 73.5-ps correlation peaks repeating at the 400-ps period are observed, but now the contrast has increased to 6.7:1. The fluctuations between peaks derive from the oscillations present in the modulator functions of Fig. 6.2(c) and could be eliminated with higher-bandwidth electronics. These results highlight a key advantage of this technique: the ability to arbitrarily extend the periodicity and ensure temporal separation of the measured correlation peaks. As reference, also included in Fig. 6.2(d) (right axis) is the correlation pattern measured via direct electronic coincidence detection with our InGaAs SPADs and without any modulation, delay-shifted for visual comparison with the modulated case; at 353 ps, the jitter-limited FWHM is approximately five times wider than that obtained from our new technique.

In the previous examples the biphoton correlation time is significantly less than the modulator correlation width, so that $G_0^{(2)}(t)$ is effectively sampling $\gamma_{\mathrm{si}}(t)$ in Eq. 6.3. Accordingly, the measurements in Figs. 6.2(b) and (d) provide upper bounds on the width of the input temporal correlations, but not a direct measure thereof. So in order to confirm that this modulation approach is indeed sensitive to modifications of $G_0^{(2)}(t)$, we next consider additional fiber links optimized for two different cases: in the first, we make use of long links to show the method's ability to resolve dispersive spreading (second-order spectral phase); in the second, a series of shorter patch cords are inserted into the idler path to demonstrate sensitivity to linear delay shifts (first-order spectral phase). For the dispersion tests, we insert optical fiber after the collimator and before the coupler in Fig. 6.1; the results for 50 and 200 m of additional fiber for the length-8 sequence in Fig. 6.2(c) are presented in Figs. 6.3(a) and (b), respectively. The photonic correlations spread in good agreement with theory, with the extra dispersion significantly modifying the coincidence peak widths. At 50 m, the background-subtracted FWHM has increased to around 100 ps; for

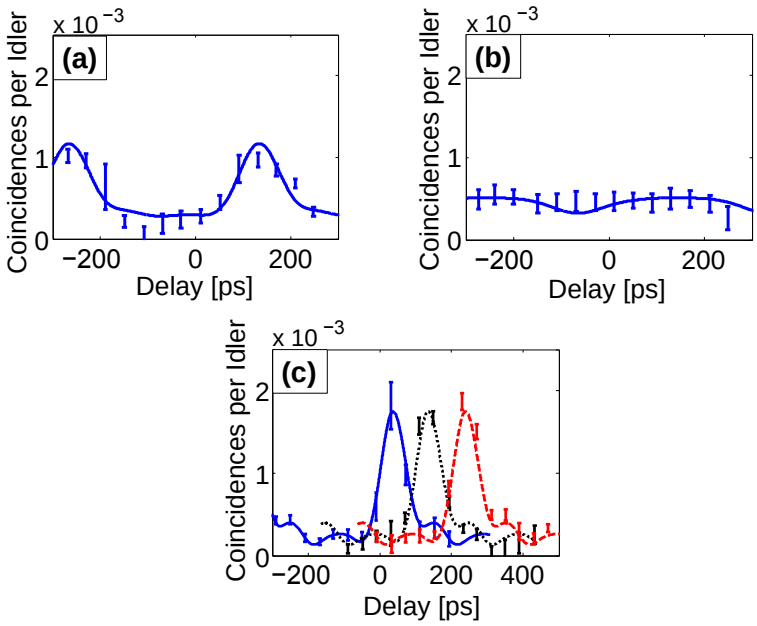

Fig. 6.3. Additional tests. Coincidence rate vs. time shift for (a) 50 m and (b) 200 m of single-mode fiber added before the coupler in Fig. 6.1. The background-subtracted FWHMs for each are 97.5 ps and 269 ps, compared to the 73.5 ps in Fig. 6.2(d). (c) Results for fiber added instead in the idler arm of Fig. 6.1. The solid blue, dotted black, and dashed red cases correspond to 41.9-, 43.7-, and 46.0-cm links, respectively.

200 m of fiber, it has spread nearly beyond recognition, with a theoretical duration of about 270 ps. Proceeding to the delay tests, we remove the long fiber links and add short fiber patches in the idler arm prior to modulator M_{i} in Fig. 6.1. Figure 6.3(c) shows the coincidence rates for added lengths of 41.9 cm (solid blue), 43.7 cm (dotted black), and 46.0 cm (dashed red). The correlation peaks are shifted by about 100 ps and are clearly separated. Combined with the observed dispersive spreading in Figs. 6.3(a) and (b), these results verify sensitivity to biphoton transformations significantly smaller than the combined ∼350-ps resolution of our electronic detectors.

The modulation functions considered thus far consist of low-duty-cycle return-to-zero pulses, a natural choice for obtaining well-resolved correlation peaks. Yet alternative patterns with more sophisticated properties can also furnish useful char-

acteristics. For the single-pulse examples earlier, the complexity of the measured biphoton correlation function is related to the duty cycle; the period specifies the longest discernible features (anything longer overlaps with the next peak), and the modulation width gives the sharpest observable correlations. To increase the ratio of the two—i.e., the maximum time-bandwidth product the system can resolve—one necessarily must reduce the duty cycle, which in turn lowers the transmitted flux.

A binary pattern which can ideally decouple loss and resolution is the M-sequence (previously described in Section 4.2.3). The circular autocorrelation of one such length-(2^N-1) phase sequence (with N an integer and elements equal to ± 1) produces a peak value of $2^N - 1$ at every multiple of $2^N - 1$, while at every other offset, -1 is obtained. Since temporal phase modulation is unobservable in our detection scheme, we must consider an amplitude-only version, in which any minus-ones are replaced by transmissivities of zero. Defining the sequences so that 2^{N-1} bits are high transmission and $2^{N-1} - 1$ are low, one predicts an ideal autocorrelation contrast of 2:1 between matched and mismatched delays. While reduced from the theoretically infinite contrast in the low-duty-cycle case, the fact that over half of the bits pass incoming photons implies minimal reduction in flux as the resolution is improved.

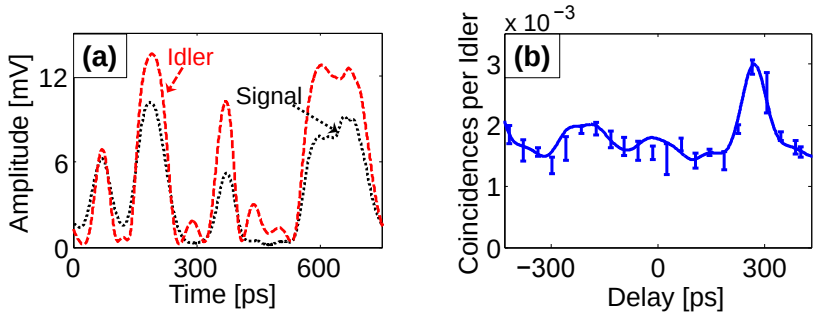

Fig. 6.4. M-sequence tests. (a) Modulation of a single-frequency laser for a length-15 sequence, shown over one full period. (b) Biphoton coincidence rate as the voltage applied to the signal modulator is temporally shifted. Error bars show experimental uncertainty, and solid lines provide theoretical predictions.

As N increases, the probability for transmitting a photon asymptotically approaches 1/2, rather than zero as in the single-pulse case. Experimentally, we consider the length-15 M-sequence [0 1 0 1 1 0 0 1 0 0 0 1 1 1 1], which at our 20-GS/s sampling rate corresponds to a period of 750 ps [Fig. 6.4(a)]. The measured coincidence rate under this modulation follows in Fig. 6.4(b); the peak-to-background contrast is near the ideal value of 2:1, and the background-subtracted FWHM is 83.6 ps, comparable to the values obtained in our low-duty-cycle experiments.

6.4 Outlook and Conclusion

In conclusion, we have realized an approach for temporal biphoton measurement based on high-speed electro-optic intensity modulation and tunable electronic delay. Our proof-of-principle experiment attains a timing resolution of 75 ps, showing sensitivity to both temporal spreading and delay. Moreover, with pseudorandom M-sequence codes, we provide a means by which the time-bandwidth product of the measurement can be increased without significantly lowering throughput. Either technique can improve the temporal sensitivity of a given pair of avalanche photodiodes, and—more excitingly—could reduce timing uncertainty well beyond even the fastest photon detectors, by employing state-of-the-art >100-GHz intensity modulators. More generally, our results provide yet another example of the value afforded by high-speed classical technologies in quantum information.

7. SUMMARY

There is a surging interest in studying quantum states of light as they provide a route for developing unprecedented technologies, such as quantum computation, quantum communication and quantum metrology. One particular quantum state of light capable of displaying correlations in both time and frequency measurements, a feature unattainable with classical light, is the time-frequency entangled photon or biphoton. This quantum state of light is already being exploited for quantum key distribution, as well as for processing quantum information. In this dissertation, we have utilized tools from ultrafast photonics to provide additional insight into the manipulation and characterization of time-frequency entangled photons, in ways that could be beneficial for the improvement of quantum technologies. Our schemes were aided by devices able to perform spectral amplitude and phase control (Fourier-transform pulse shapers and dispersive media), and temporal amplitude and phase control (electro-optic intensity and phase modulators).

In Chapter 2, we described and demonstrated a scheme for adjusting the relative delay between a pair of entangled photons with fixed dispersive media and in a manner compatible with high-speed delay switching. An apparent impact of this work would be in the aspect of high-speed delay correction in quantum networks. It would also be interesting to introduce this delay control idea to temporally-multiplexed single-photon sources for generating single-photons on demand.

In Chapter 3, we implemented near-field frequency-to-time mapping (FTM) to achieve arbitrary shaping of entangled photons, thereby circumventing the need for very large dispersion values typically required for conventional FTM. An avenue for further research could be examining the near-field approach for quantum key distribution, especially since the conventional FTM method is already being used to serve as a conjugate-basis in time-frequency quantum key distribution.

We began our studies on biphoton combs in Chapter 4. The distinguishing feature of a biphoton frequency comb is that its spectrum consists of a superposition of discretized frequency-bin pairs, hence the potential for high-dimensional entanglement. We examined the time-domain correlation trains that coherent biphoton combs display due to interference. Moreover, we also used this opportunity to verify the temporal self-imaging (Talbot) effect using entangled photons for the first time, in addition to exploring spectral phase-only filtering for generating more efficient correlation trains.

Our measurements in Chapter 4 relied on sum-frequency generation for sub-picosecond resolution, since standard single-photon detectors only resolve down to ~ 100 ps; however, for narrower linewidth biphoton combs, such measurement techniques become impractical due to diminishing nonlinear efficiency. In Chapter 5, we discussed a technique for studying coherent biphoton frequency combs even with slow detectors. Using electro-optic phase modulators to mix comb lines, we were able to observe interference from two and three comb line pairs, and subsequently measured the dispersion in a single-mode fiber. It will be interesting to investigate this method beyond single-digit comb line pairs in order to characterize larger-dimensional entanglement.

Lastly, in Chapter 6, we discussed our realization of a high-speed modulation setup for improving the temporal resolution coincidence measurements. We were able attain a timing resolution of 75 ps, five-times better than the resolution in regular measurements with our InGaAs single-photon detectors. While not as fast as nonlinear mixing techniques, state-of-the-art intensity modulators can offer speeds faster than 100 GHz, thus alluding to the potential of improving the timing resolution of our scheme less than 10 ps.

REFERENCES

REFERENCES

[1] T. D. Ladd, F. Jelezko, R. Laflamme, Y. Nakamura, C. Monroe, and J. L. O'Brien, "Quantum computers," *Nature*, vol. 464, pp. 45–53, 2010.

[2] M. A. Nielsen and I. L. Chuang, *Quantum computation and quantum information*. Cambridge University Press, 2010.

[3] N. Gisin, G. Ribordy, W. Tittel, and H. Zbinden, "Quantum cryptography," *Rev. Mod. Phys.*, vol. 74, pp. 145–195, Mar 2002.

[4] N. Gisin and R. Thew, "Quantum communication," *Nature Photonics*, vol. 1, pp. 165–171, Mar. 2007.

[5] H.-K. Lo, M. Curty, and K. Tamaki, "Secure quantum key distribution," *Nature Photonics*, vol. 8, pp. 595–604, 2014.

[6] V. Giovannetti, S. Lloyd, and L. Maccone, "Quantum-enhanced positioning and clock synchronization," *Nature*, vol. 412, pp. 417–419, 2001.

[7] ——, "Advances in quantum metrology," *Nature Photonics*, vol. 5, no. 4, pp. 222–229, 2011.

[8] J. L. O'brien, A. Furusawa, and J. Vučković, "Photonic quantum technologies," *Nature Photonics*, vol. 3, no. 12, pp. 687–695, 2009.

[9] A. Valencia, M. V. Chekhova, A. Trifonov, and Y. Shih, "Entangled two-photon wave packet in a dispersive medium," *Phys. Rev. Lett.*, vol. 88, p. 183601, Apr 2002.

[10] S.-Y. Baek, O. Kwon, and Y.-H. Kim, "Nonlocal dispersion control of a single-photon waveform," *Phys. Rev. A*, vol. 78, p. 013816, Jul 2008.

[11] ——, "Temporal shaping of a heralded single-photon wave packet," *Phys. Rev. A*, vol. 77, p. 013829, Jan. 2008.

[12] M. Avenhaus, A. Eckstein, P. J. Mosley, and C. Silberhorn, "Fiber-assisted single-photon spectrograph," *Opt. Lett.*, vol. 34, no. 18, pp. 2873–2875, Sep 2009.

[13] A. Pe'er, B. Dayan, A. A. Friesem, and Y. Silberberg, "Temporal shaping of entangled photons," *Phys. Rev. Lett.*, vol. 94, p. 073601, Feb. 2005.

[14] B. Dayan, "Theory of two-photon interactions with broadband down-converted light and entangled photons," *Phys. Rev. A*, vol. 76, p. 043813, Oct 2007.

[15] F. Zäh, M. Halder, and T. Feurer, "Amplitude and phase modulation of time-energy entangled two-photon states," *Opt. Express*, vol. 16, no. 21, pp. 16 452–16 458, Oct. 2008.

[16] C. Bernhard, B. Bessire, T. Feurer, and A. Stefanov, "Shaping frequency-entangled qudits," *Phys. Rev. A*, vol. 88, p. 032322, Sep 2013.

[17] J. M. Lukens, A. Dezfooliyan, C. Langrock, M. M. Fejer, D. E. Leaird, and A. M. Weiner, "Biphoton manipulation with a fiber-based pulse shaper," *Opt. Lett.*, vol. 38, pp. 4652–4655, 2013.

[18] ——, "Demonstration of high-order dispersion cancellation with an ultrahigh-efficiency sum-frequency correlator," *Phys. Rev. Lett.*, vol. 111, p. 193603, Nov 2013.

[19] ——, "Orthogonal spectral coding of entangled photons," *Phys. Rev. Lett.*, vol. 112, p. 133602, Apr 2014.

[20] P. Kolchin, C. Belthangady, S. Du, G. Y. Yin, and S. E. Harris, "Electro-optic modulation of single photons," *Phys. Rev. Lett.*, vol. 101, p. 103601, Sep. 2008.

[21] C. Belthangady, S. Du, C.-S. Chuu, G. Y. Yin, and S. E. Harris, "Modulation and measurement of time-energy entangled photons," *Phys. Rev. A*, vol. 80, p. 031803, Sep. 2009.

[22] S. Sensarn, G. Y. Yin, and S. E. Harris, "Observation of nonlocal modulation with entangled photons," *Phys. Rev. Lett.*, vol. 103, p. 163601, Oct 2009.

[23] C. Belthangady, C.-S. Chuu, I. A. Yu, G. Y. Yin, J. M. Kahn, and S. E. Harris, "Hiding single photons with spread spectrum technology," *Phys. Rev. Lett.*, vol. 104, p. 223601, Jun. 2010.

[24] S. Mittal, V. V. Orre, A. Restelli, R. Salem, E. A. Goldschmidt, and M. Hafezi, "Temporal and spectral manipulations of correlated photons using a time lens," *Phys. Rev. A*, vol. 96, p. 043807, Oct 2017.

[25] J. Mower, Z. Zhang, P. Desjardins, C. Lee, J. H. Shapiro, and D. Englund, "High-dimensional quantum key distribution using dispersive optics," *Phys. Rev. A*, vol. 87, p. 062322, Jun 2013.

[26] C. Lee, Z. Zhang, G. R. Steinbrecher, H. Zhou, J. Mower, T. Zhong, L. Wang, X. Hu, R. D. Horansky, V. B. Verma, A. E. Lita, R. P. Mirin, F. Marsili, M. D. Shaw, S. W. Nam, G. W. Wornell, F. N. C. Wong, J. H. Shapiro, and D. Englund, "Entanglement-based quantum communication secured by nonlocal dispersion cancellation," *Phys. Rev. A*, vol. 90, p. 062331, Dec 2014.

[27] J. Nunn, L. J. Wright, C. Söller, L. Zhang, I. A. Walmsley, and B. J. Smith, "Large-alphabet time-frequency entangled quantum key distribution by means of time-to-frequency conversion," *Opt. Express*, vol. 21, no. 13, pp. 15 959–15 973, Jul 2013.

[28] J. M. Lukens and P. Lougovski, "Frequency-encoded photonic qubits for scalable quantum information processing," *Optica*, vol. 4, no. 1, pp. 8–16, Jan 2017.

[29] Y. Shih, "Entangled biphoton source - property and preparation," *Rep. Prog. Phys.*, vol. 66, no. 6, p. 1009, 2003.

[30] L. Mandel and E. Wolf, *Optical Coherence and Quantum Optics*. Cambridge, UK: Cambridge University Press, 1995.

[31] R. J. Glauber, "The quantum theory of optical coherence," *Phys. Rev.*, vol. 130, pp. 2529–2539, Jun. 1963.

[32] K. R. Parameswaran, R. K. Route, J. R. Kurz, R. V. Roussev, M. M. Fejer, and M. Fujimura, "Highly efficient second-harmonic generation in buried waveguides formed by annealed and reverse proton exchange in periodically poled lithium niobate," *Opt. Lett.*, vol. 27, no. 3, pp. 179–181, Feb. 2002.

[33] C. Langrock, S. Kumar, J. E. McGeehan, A. E. Willner, and M. M. Fejer, "All-optical signal processing using $\chi^{(2)}$ nonlinearities in guided-wave devices," *J. Lightw. Technol.*, vol. 24, no. 7, p. 2579, Jul. 2006.

[34] O. D. Odele, J. M. Lukens, J. A. Jaramillo-Villegas, C. Langrock, M. M. Fejer, D. E. Leaird, and A. M. Weiner, "Tunable delay control of entangled photons based on dispersion cancellation," *Opt. Express*, vol. 23, no. 17, pp. 21 857–21 866, Aug 2015.

[35] O. D. Odele, J. M. Lukens, J. A. Jaramillo-Villegas, P. Imany, C. Langrock, M. M. Fejer, D. E. Leaird, and A. M. Weiner, "High-speed switching of biphoton delays through electro-optic pump frequency modulation," *APL Photonics*, vol. 2, no. 1, p. 011301, 2017.

[36] I. Ali Khan and J. C. Howell, "Experimental demonstration of high two-photon time-energy entanglement," *Phys. Rev. A*, vol. 73, p. 031801, Mar 2006.

[37] I. Ali-Khan, C. J. Broadbent, and J. C. Howell, "Large-alphabet quantum key distribution using energy-time entangled bipartite states," *Phys. Rev. Lett.*, vol. 98, p. 060503, Feb 2007.

[38] V. Giovannetti, S. Lloyd, L. Maccone, and F. N. C. Wong, "Clock synchronization with dispersion cancellation," *Phys. Rev. Lett.*, vol. 87, p. 117902, Aug 2001.

[39] A. Valencia, G. Scarcelli, and Y. Shih, "Distant clock synchronization using entangled photon pairs," *Applied Physics Letters*, vol. 85, no. 13, pp. 2655–2657, 2004.

[40] J. van Howe and C. Xu, "Ultrafast optical signal processing based upon space-time dualities," *J. Lightwave Technol.*, vol. 24, no. 7, p. 2649, Jul 2006.

[41] V. Torres-Company, J. Lancis, and P. Andrés, "Chapter 1 - space-time analogies in optics," ser. Progress in Optics, E. Wolf, Ed. Elsevier, 2011, vol. 56, pp. 1 – 80.

[42] J. van Howe and C. Xu, "Ultrafast optical delay line by use of a time-prism pair," *Opt. Lett.*, vol. 30, no. 1, pp. 99–101, Jan 2005.

[43] J. E. Sharping, Y. Okawachi, J. van Howe, C. Xu, Y. Wang, A. E. Willner, and A. L. Gaeta, "All-optical, wavelength and bandwidth preserving, pulse delay based on parametric wavelength conversion and dispersion," *Opt. Express*, vol. 13, no. 20, pp. 7872–7877, Oct 2005.

[44] Y. Wang, C. Yu, L. Yan, A. E. Willner, R. Roussev, C. Langrock, M. M. Fejer, J. E. Sharping, and A. L. Gaeta, "44-ns continuously tunable dispersionless optical delay element using a PPLN waveguide with two-pump configuration, DCF, and a dispersion compensator," *IEEE Photon. Technol. Lett.*, vol. 19, no. 11, pp. 861–863, June 2007.

[45] J. D. Franson, "Nonlocal cancellation of dispersion," *Phys. Rev. A*, vol. 45, pp. 3126–3132, Mar. 1992.

[46] S.-Y. Baek, Y.-W. Cho, and Y.-H. Kim, "Nonlocal dispersion cancellation using entangled photons," *Opt. Express*, vol. 17, no. 21, pp. 19 241–19 252, Oct. 2009.

[47] K. A. O'Donnell, "Observations of dispersion cancellation of entangled photon pairs," *Phys. Rev. Lett.*, vol. 106, p. 063601, Feb 2011.

[48] A. M. Weiner, "Femtosecond pulse shaping using spatial light modulators," *Rev. Sci. Instrum.*, vol. 71, no. 5, pp. 1929–1960, 2000.

[49] R. Prevedel, K. M. Schreiter, J. Lavoie, and K. J. Resch, "Classical analog for dispersion cancellation of entangled photons with local detection," *Phys. Rev. A*, vol. 84, p. 051803, Nov 2011.

[50] M. Asobe, O. Tadanaga, H. Miyazawa, Y. Nishida, and H. Suzuki, "Multiple quasi-phase-matched linbo3 wavelength converter with a continuously phase-modulated domain structure," *Opt. Lett.*, vol. 28, no. 7, pp. 558–560, Apr 2003.

[51] F. Kaneda, B. G. Christensen, J. J. Wong, H. S. Park, K. T. McCusker, and P. G. Kwiat, "Time-multiplexed heralded single-photon source," *Optica*, vol. 2, no. 12, pp. 1010–1013, Dec 2015.

[52] G. J. Mendoza, R. Santagati, J. Munns, E. Hemsley, M. Piekarek, E. Martín-López, G. D. Marshall, D. Bonneau, M. G. Thompson, and J. L. O'Brien, "Active temporal and spatial multiplexing of photons," *Optica*, vol. 3, no. 2, pp. 127–132, Feb 2016.

[53] C. Xiong, X. Zhang, Z. Liu, M. J. Collins, A. Mahendra, L. G. Helt, M. J. Steel, D.-Y. Choi, C. J. Chae, P. H. W. Leong, and B. J. Eggleton, "Active temporal multiplexing of indistinguishable heralded single photons," *Nature Commun.*, vol. 7, p. 10853, 2016.

[54] D. S. Hum and M. M. Fejer, "Quasi-phasematching," *Comptes Rendus Physique*, vol. 8, no. 2, pp. 180 – 198, 2007, recent advances in crystal optics.

[55] H.-H. Lu, O. D. Odele, D. E. Leaird, and A. M. Weiner, "Arbitrary shaping of biphoton correlations using near-field frequency-to-time mapping," *Opt. Lett.*, vol. 43, no. 4, pp. 743–746, Feb 2018.

[56] J. A. Jaramillo-Villegas, P. Imany, O. D. Odele, D. E. Leaird, Z.-Y. Ou, M. Qi, and A. M. Weiner, "Persistent energy–time entanglement covering multiple resonances of an on-chip biphoton frequency comb," *Optica*, vol. 4, no. 6, pp. 655–658, Jun 2017.

[57] A. M. Weiner, *Ultrafast Optics*. Hoboken, NJ: Wiley, 2009.

[58] V. Torres-Company, D. E. Leaird, and A. M. Weiner, "Dispersion requirements in coherent frequency-to-time mapping," *Opt. Express*, vol. 19, no. 24, pp. 24 718–24 729, Nov 2011.

[59] A. Dezfooliyan and A. M. Weiner, "Photonic synthesis of high fidelity microwave arbitrary waveforms using near field frequency to time mapping," *Opt. Express*, vol. 21, no. 19, pp. 22 974–22 987, Sep 2013.

[60] B. H. Kolner and M. Nazarathy, "Temporal imaging with a time lens," *Opt. Lett.*, vol. 14, no. 12, pp. 630–632, Jun. 1989.

[61] J. Lavoie, J. M. Donohue, L. G. Wright, A. Fedrizzi, and K. J. Resch, "Spectral compression of single photons," *Nature Photonics*, vol. 7, no. 5, pp. 363–366, 2013.

[62] M. Karpinski, M. Jachura, L. J. Wright, and B. J. Smith, "Bandwidth manipulation of quantum light by an electro-optic time lens," *Nature Photonics*, vol. 11, pp. 53–57, 2017.

[63] J. M. Lukens, O. Odele, C. Langrock, M. M. Fejer, D. E. Leaird, and A. M. Weiner, "Generation of biphoton correlation trains through spectral filtering," *Opt. Express*, vol. 22, no. 8, pp. 9585–9596, Apr 2014.

[64] J. Perina, Jr., "Characterization of a resonator using entangled two-photon states," *Opt. Commun.*, vol. 221, no. 13, pp. 153–161, 2003.

[65] Y. J. Lu, R. L. Campbell, and Z. Y. Ou, "Mode-locked two-photon states," *Phys. Rev. Lett.*, vol. 91, p. 163602, Oct 2003.

[66] H. Goto, Y. Yanagihara, H. Wang, T. Horikiri, and T. Kobayashi, "Observation of an oscillatory correlation function of multimode two-photon pairs," *Phys. Rev. A*, vol. 68, p. 015803, Jul 2003.

[67] H. Goto, H. Wang, T. Horikiri, Y. Yanagihara, and T. Kobayashi, "Two-photon interference of multimode two-photon pairs with an unbalanced interferometer," *Phys. Rev. A*, vol. 69, p. 035801, Mar 2004.

[68] H. Wang, T. Horikiri, and T. Kobayashi, "Polarization-entangled mode-locked photons from cavity-enhanced spontaneous parametric down-conversion," *Phys. Rev. A*, vol. 70, p. 043804, Oct 2004.

[69] H.-b. Wang and T. Kobayashi, "Quantum interference of a mode-locked two-photon state," *Phys. Rev. A*, vol. 70, p. 053816, Nov 2004.

[70] M. A. Sagioro, C. Olindo, C. H. Monken, and S. Pádua, "Time control of two-photon interference," *Phys. Rev. A*, vol. 69, p. 053817, May 2004.

[71] A. Zavatta, S. Viciani, and M. Bellini, "Recurrent fourth-order interference dips and peaks with a comblike two-photon entangled state," *Phys. Rev. A*, vol. 70, p. 023806, Aug 2004.

[72] F.-Y. Wang, B.-S. Shi, and G.-C. Guo, "Observation of time correlation function of multimode two-photon pairs on a rubidium D_2 line," *Opt. Lett.*, vol. 33, no. 19, pp. 2191–2193, Oct 2008.

[73] W. C. Jiang, X. Lu, J. Zhang, O. Painter, and Q. Lin, "A silicon-chip source of bright photon-pair comb," *arXiv:1210.4455*, 2012.

[74] A. Aspect, "Bell's inequality test: more ideal than ever," *Nature*, vol. 398, pp. 189–190, March 1999.

[75] T. Udem, R. Holzwarth, and T. W. Hänsch, "Optical frequency metrology," *Nature*, vol. 416, no. 6877, pp. 233–237, Mar. 2002.

[76] N. R. Newbury, "Searching for applications with a fine-tooth comb," *Nature Photon.*, vol. 5, pp. 186–188, Mar. 2011.

[77] Z. Xie, T. Zhong, S. Shrestha, X. Xu, J. Liang, Y.-X. Gong, J. C. Bienfang, A. Restelli, J. H. Shapiro, W. N. C., and C. Wei Wong, "Harnessing high-dimensional hyperentanglement through a biphoton frequency comb," *Nature Photonics*, vol. 9, no. 8, pp. 536–542, 08 2015.

[78] S. Clemmen, K. P. Huy, W. Bogaerts, R. G. Baets, P. Emplit, and S. Massar, "Continuous wave photon pair generation in silicon-on-insulator waveguides and ring resonators," *Opt. Express*, vol. 17, no. 19, pp. 16 558–16 570, Sep. 2009.

[79] S. Azzini, D. Grassani, M. J. Strain, M. Sorel, L. G. Helt, J. E. Sipe, M. Liscidini, M. Galli, and D. Bajoni, "Ultra-low power generation of twin photons in a compact silicon ring resonator," *Opt. Express*, vol. 20, no. 21, pp. 23 100–23 107, Oct. 2012.

[80] C. Reimer, L. Caspani, M. Clerici, M. Ferrera, M. Kues, M. Peccianti, A. Pasquazi, L. Razzari, B. E. Little, S. T. Chu, D. J. Moss, and R. Morandotti, "Integrated frequency comb source of heralded single photons," *Opt. Express*, vol. 22, no. 6, pp. 6535–6546, 2014.

[81] C. Reimer, M. Kues, P. Roztocki, B. Wetzel, F. Grazioso, B. E. Little, S. T. Chu, T. Johnston, Y. Bromberg, L. Caspani, D. J. Moss, and R. Morandotti, "Generation of multiphoton entangled quantum states by means of integrated frequency combs," *Science*, vol. 351, no. 6278, pp. 1176–1180, 2016.

[82] F. Mazeas, M. Traetta, M. Bentivegna, F. Kaiser, D. Aktas, W. Zhang, C. A. Ramos, L. A. Ngah, T. Lunghi, E. Picholle, N. Belabas-Plougonven, X. L. Roux, E. Cassan, D. Marris-Morini, L. Vivien, G. Sauder, L. Labonté, and S. Tanzilli, "High-quality photonic entanglement for wavelength-multiplexed quantum communication based on a silicon chip," *Opt. Express*, vol. 24, no. 25, pp. 28 731–28 738, Dec 2016.

[83] M. Kues, C. Reimer, P. Roztocki, L. R. Cortés, S. Sciara, B. Wetzel, Y. Zhang, A. Cino, S. T. Chu, B. E. Little, D. J. Moss, L. Caspani, J. Azaña, and R. Morandotti, "On-chip generation of high-dimensional entangled quantum states and their coherent control," *Nature*, vol. 546, no. 7660, pp. 622–626, 2017.

[84] Y. J. Lu and Z. Y. Ou, "Optical parametric oscillator far below threshold: Experiment versus theory," *Phys. Rev. A*, vol. 62, p. 033804, Aug 2000.

[85] X. Guo, Y. Mei, and S. Du, "Testing the bell inequality on frequency-bin entangled photon pairs using time-resolved detection," *Optica*, vol. 4, no. 4, pp. 388–392, Apr 2017.

[86] V. Torres-Company, J. Lancis, H. Lajunen, and A. T. Friberg, "Coherence revivals in two-photon frequency combs," *Phys. Rev. A*, vol. 84, p. 033830, Sep 2011.

[87] T. Jannson and J. Jannson, "Temporal self-imaging effect in single-mode fibers," *J. Opt. Soc. Am.*, vol. 71, no. 11, pp. 1373–1376, Nov. 1981.

[88] A. M. Weiner, "Ultrafast optical pulse shaping: A tutorial review," *Opt. Commun.*, vol. 284, no. 15, pp. 3669 – 3692, 2011.

[89] A. M. Weiner and D. E. Leaird, "Generation of terahertz-rate trains of femtosecond pulses by phase-only filtering," *Opt. Lett.*, vol. 15, no. 1, pp. 51–53, Jan. 1990.

[90] H. Talbot, "Facts relating to optical science." *Philos. Mag. Ser. 3*, vol. 9, no. 56, pp. 401–407, 1836.

[91] K. Patorski, "The self-imaging phenomenon and its applications," in *Progress in Optics Vol. 27*, ser. Progress in Optics, E. Wolf, Ed. Elsevier, 1989, vol. 27, pp. 1 – 108.

[92] J. Wen, Y. Zhang, and M. Xiao, "The Talbot effect: recent advances in classical optics, nonlinear optics, and quantum optics," *Adv. Opt. Photon.*, vol. 5, no. 1, pp. 83–130, Mar 2013.

[93] K.-H. Luo, J. Wen, X.-H. Chen, Q. Liu, M. Xiao, and L.-A. Wu, "Second-order Talbot effect with entangled photon pairs," *Phys. Rev. A*, vol. 80, p. 043820, Oct. 2009.

[94] X.-B. Song, H.-B. Wang, J. Xiong, K. Wang, X. Zhang, K.-H. Luo, and L.-A. Wu, "Experimental observation of quantum Talbot effects," *Phys. Rev. Lett.*, vol. 107, p. 033902, Jul. 2011.

[95] B. Kolner, "Space-time duality and the theory of temporal imaging," *IEEE J. Quantum Electron.*, vol. 30, no. 8, pp. 1951–1963, Aug. 1994.

[96] J. Azaña and M. A. Muriel, "Technique for multiplying the repetition rates of periodic trains of pulses by means of atemporal self-imaging effect in chirped fiber gratings," *Opt. Lett.*, vol. 24, no. 23, pp. 1672–1674, Dec 1999.

[97] J. Azaña and M. Muriel, "Temporal self-imaging effects: theory and application for multiplying pulse repetition rates," *IEEE J. Sel. Top. Quantum Electron.*, vol. 7, no. 4, pp. 728–744, 2001.

[98] J. Caraquitena, Z. Jiang, D. E. Leaird, and A. M. Weiner, "Tunable pulse repetition-rate multiplication using phase-only line-by-line pulse shaping," *Opt. Lett.*, vol. 32, no. 6, pp. 716–718, Mar 2007.

[99] I. Sizer, T., "Increase in laser repetition rate by spectral selection," *IEEE J. Quantum Electron.*, vol. 25, no. 1, pp. 97–103, 1989.

[100] P. Petropoulos, M. Ibsen, M. N. Zervas, and D. J. Richardson, "Generation of a 40-GHz pulse stream by pulse multiplication with a sampled fiber Bragg grating," *Opt. Lett.*, vol. 25, no. 8, pp. 521–523, Apr 2000.

[101] K. Yiannopoulos, K. Vyrsokinos, E. Kehayas, N. Pleros, K. Vlachos, H. Avramopoulos, and G. Guekos, "Rate multiplication by double-passing Fabry-Perot filtering," *IEEE Photon. Technol. Lett.*, vol. 15, no. 9, pp. 1294–1296, 2003.

[102] A. M. Weiner, D. E. Leaird, G. P. Wiederrecht, and K. A. Nelson, "Femtosecond pulse sequences used for optical manipulation of molecular motion," *Science*, vol. 247, no. 4948, pp. 1317–1319, 1990.

[103] M. R. Schroeder, *Number Theory in Science and Communication*. Berlin: Springer-Verlag, 1986.

[104] P. Imany, O. D. Odele, J. A. Jaramillo-Villegas, D. E. Leaird, and A. M. Weiner, "Characterization of coherent quantum frequency combs using electro-optic phase modulation," *Phys. Rev. A*, vol. 97, p. 013813, Jan 2018.

[105] O. Kuzucu, F. N. C. Wong, S. Kurimura, and S. Tovstonog, "Time-resolved single-photon detection by femtosecond upconversion," *Opt. Lett.*, vol. 33, pp. 2257–2259, 2008.

[106] L. Olislager, J. Cussey, A. T. Nguyen, P. Emplit, S. Massar, J.-M. Merolla, and K. P. Huy, "Frequency-bin entangled photons," *Phys. Rev. A*, vol. 82, p. 013804, Jul 2010.

[107] J. D. Franson, "Bell inequality for position and time," *Physical Review Letters*, vol. 62, no. 19, p. 2205, 1989.

[108] I. Marcikic, H. de Riedmatten, W. Tittel, V. Scarani, H. Zbinden, and N. Gisin, "Time-bin entangled qubits for quantum communication created by femtosecond pulses," *Phys. Rev. A*, vol. 66, p. 062308, Dec 2002.

[109] R. T. Thew, A. Acin, H. Zbinden, and N. Gisin, "Bell-type test of energy-time entangled qutrits," *Physical Review Letters*, vol. 93, no. 1, p. 010503, 2004.

[110] H. de Riedmatten, I. Marcikic, V. Scarani, W. Tittel, H. Zbinden, and N. Gisin, "Tailoring photonic entanglement in high-dimensional hilbert spaces," *Phys. Rev. A*, vol. 69, p. 050304, May 2004.

[111] S. E. Harris, "Nonlocal modulation of entangled photons," *Phys. Rev. A*, vol. 78, p. 021807, Aug. 2008.

[112] J. M. Lukens and A. M. Weiner, *Biphoton Pulse Shaping*. Cham: Springer International Publishing, 2015, pp. 423–448.

[113] P. Imany, J. A. Jaramillo-Villegas, O. D. Odele, K. Han, D. E. Leaird, J. M. Lukens, P. Lougovski, M. Qi, and A. M. Weiner, "50-ghz-spaced comb of high-dimensional frequency-bin entangled photons from an on-chip silicon nitride microresonator," *Opt. Express*, vol. 26, no. 2, pp. 1825–1840, Jan 2018.

[114] J. M. Lukens, O. D. Odele, D. E. Leaird, and A. M. Weiner, "Electro-optic modulation for high-speed characterization of entangled photon pairs," *Optics letters*, vol. 40, no. 22, pp. 5331–5334, 2015.

[115] M. Ghioni, A. Gulinatti, I. Rech, F. Zappa, and S. Cova, "Progress in silicon single-photon avalanche diodes," *IEEE Journal of Selected Topics in Quantum Electronics*, vol. 13, no. 4, pp. 852–862, July 2007.

[116] J. Zhang, W. Slysz, A. Verevkin, O. Okunev, G. Chulkova, A. Korneev, A. Lipatov, G. N. Gol'tsman, and R. Sobolewski, "Response time characterization of nbn superconducting single-photon detectors," *IEEE Transactions on Applied Superconductivity*, vol. 13, no. 2, pp. 180–183, June 2003.

[117] A. Pearlman, A. Cross, W. Slysz, J. Zhang, A. Verevkin, M. Currie, A. Korneev, P. Kouminov, K. Smirnov, B. Voronov *et al.*, "Gigahertz counting rates of nbn single-photon detectors for quantum communications," *IEEE transactions on applied superconductivity*, vol. 15, no. 2, pp. 579–582, 2005.

[118] B. Dayan, A. Pe'er, A. A. Friesem, and Y. Silberberg, "Nonlinear interactions with an ultrahigh flux of broadband entangled photons," *Phys. Rev. Lett.*, vol. 94, p. 043602, Feb. 2005.

[119] K. A. O'Donnell and A. B. U'Ren, "Time-resolved up-conversion of entangled photon pairs," *Phys. Rev. Lett.*, vol. 103, p. 123602, Sep.. 2009.

[120] S. Du, "Atomic-resonance-enhanced nonlinear optical frequency conversion with entangled photon pairs," *Phys. Rev. A*, vol. 83, p. 033807, Mar 2011.

[121] O. Kuzucu, F. N. C. Wong, S. Kurimura, and S. Tovstonog, "Joint temporal density measurements for two-photon state characterization," *Phys. Rev. Lett.*, vol. 101, p. 153602, 2008.

[122] J. M. Donohue, M. Agnew, J. Lavoie, and K. J. Resch, "Coherent ultrafast measurement of time-bin encoded photons," *Phys. Rev. Lett.*, vol. 111, p. 153602, Oct 2013.

[123] J. M. Donohue, J. Lavoie, and K. J. Resch, "Ultrafast time-division demultiplexing of polarization-entangled photons," *Phys. Rev. Lett.*, vol. 113, p. 163602, Oct 2014.

[124] EOSpace, "Advanced product line," 2015.

[125] C. K. Hong, Z. Y. Ou, and L. Mandel, "Measurement of subpicosecond time intervals between two photons by interference," *Phys. Rev. Lett.*, vol. 59, pp. 2044–2046, Nov 1987.

[126] A. Rashidinejad and A. M. Weiner, "Photonic radio-frequency arbitrary waveform generation with maximal time-bandwidth product capability," *J. Lightw. Technol.*, vol. 32, no. 20, pp. 3383–3393, Oct 2014.

[127] Y. Li, A. Rashidinejad, J.-M. Wun, D. E. Leaird, J.-W. Shi, and A. M. Weiner, "Photonic generation of W-band arbitrary waveforms with high time-bandwidth products enabling 3.9 mm range resolution," *Optica*, vol. 1, no. 6, pp. 446–454, Dec 2014.

APPENDIX

A. COMPILATION OF PHASE MATCHING CURVES

The quasi-phase matched (QPM) waveguides used for our biphoton work were obtained through a collaboration with Prof. Martin Fejer's group at Stanford University. In this appendix, we provide a record of the phase matching curves we measured for two chips comprising of 50 waveguides each. The phase matching curve shows a measure of the second-harmonic generation (SHG) conversion efficiency as a function of the pump frequency:

$$\text{Conversion efficiency} = \frac{P_{\text{SHG}}}{P_{\text{in}}^2} \times 100\% \tag{A.1}$$

On each chip, the waveguides are grouped into sections based on quasi-phase-matching structures.

Section 1: Uniform QPM (Single Phase Matching Peak)

Section 2: Phase-modulated QPM (5 peaks with 2-nm spacing)

Section 3: Linearly-chirped QPM (10-nm broad bandwidth)

Section 4: Phase-modulated QPM (5 peaks with 1-nm spacing)

Section 5: Linearly-chirped QPM (5-nm broad bandwidth)

For the experiments discussed in this dissertation, we opted for waveguides with high photon-conversion efficiencies while also taking the pump-acceptance bandwidth into consideration.

In Chapter 2, we implemented our experimental setups with Chips 4 and 6. For the first demonstration of ps-delay control (Fig. 2.2) with a fixed pump along with shifts in the dispersion curve, we used Chip 4–Section 1–Waveguide 4 for spontaneous parametric downconversion (SPDC) while Chip 6–Section 1–Waveguide 8 was used for sum-frequency generation (SFG); the other ps-delay control experiment required

QPM waveguides that could accommodate multiple pump frequencies, so we used Chip 4–Section 2–Waveguide 5 for SPDC and Chip 6–Section 2–Waveguide 8 for SFG. The experiments on ns-delay control and high-speed delay switching also depended on pump frequency modulation (Fig. 2.5), so we used Chip 4–Section 2–Waveguide 4 for SHG and Chip 6–Section 2–Waveguide 8 for SPDC.

In Chapter 3, Chip 4–Section 1–Waveguide 3 was used for SPDC while Chip 6–Section 1–Waveguide 8 was used for SFG. A similar waveguide pair was also used for the experiment in Chapter 4, while the experiments in Chapters 5 and 6 utilized Chip 4–Section 1–Waveguide 9 for SPDC.

CHIP 4 – SECTION 1

Section 01 – Waveguide 01
BAD

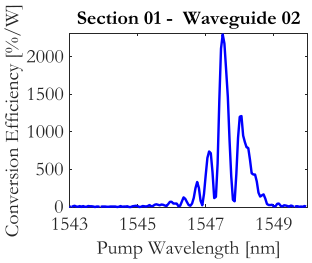

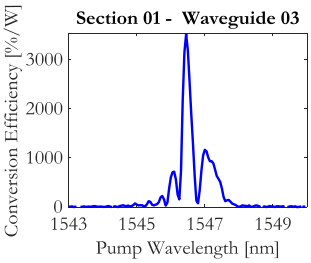

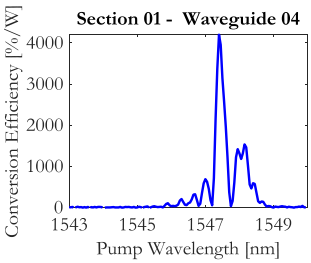

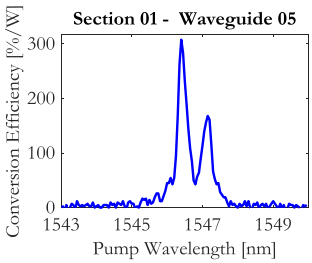

Section 01 – Waveguide 06
BAD

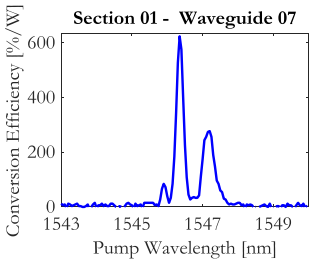

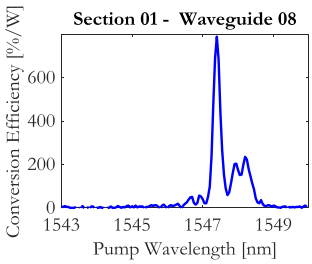

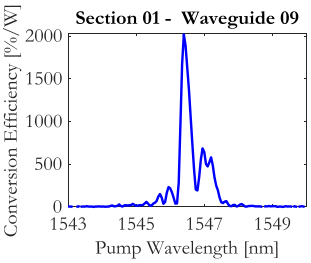

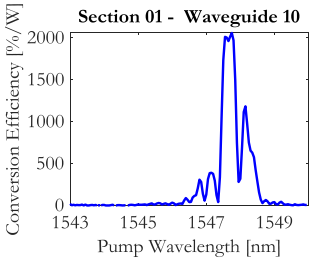

CHIP 4 – SECTION 2

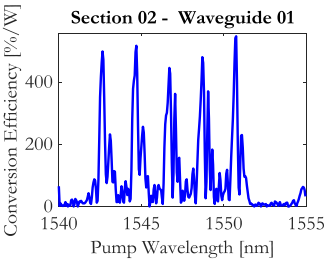

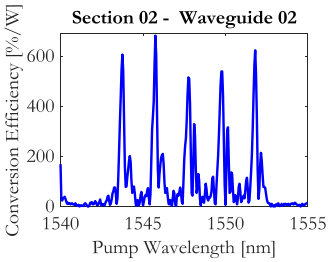

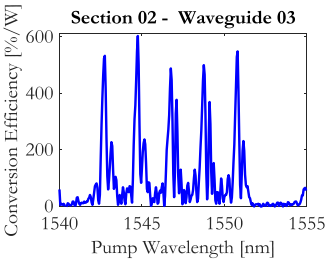

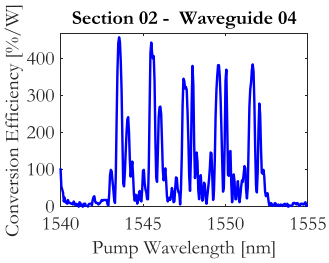

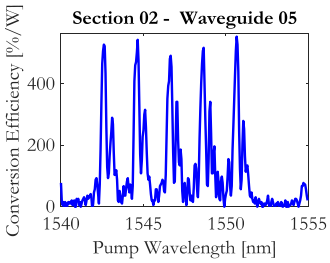

Section 01 – Waveguide 06
BAD

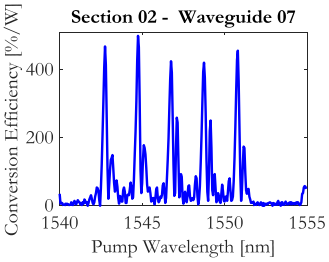

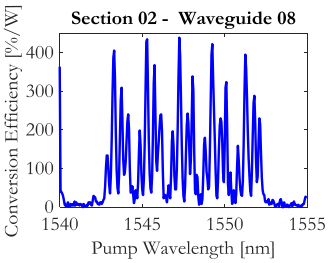

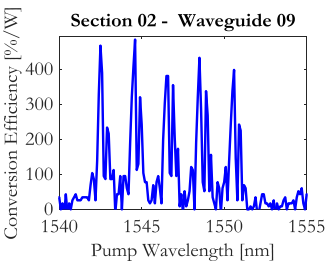

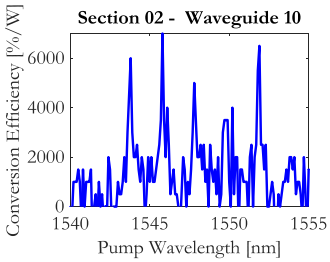

CHIP 4 – SECTION 3

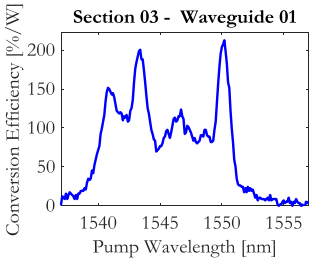

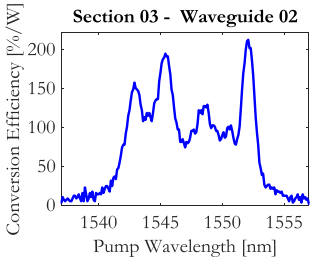

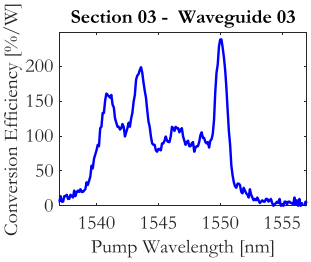

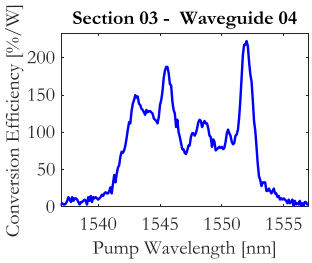

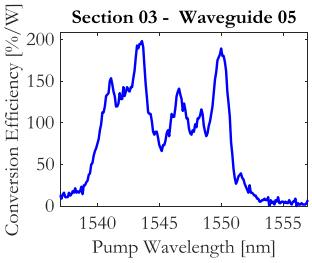

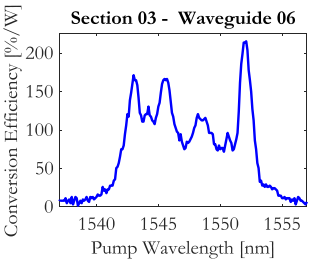

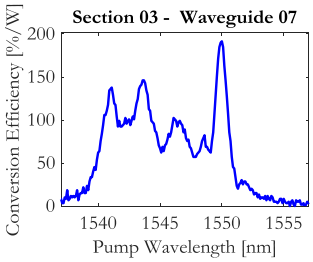

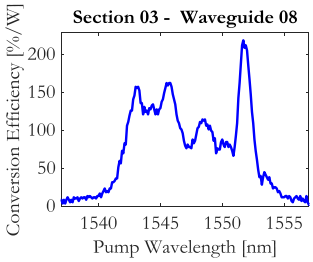

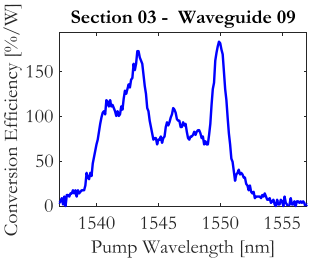

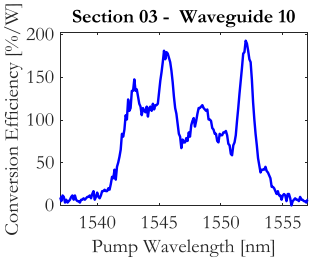

CHIP 4 – SECTION 4

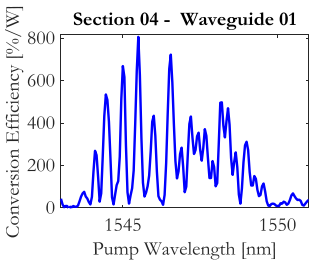

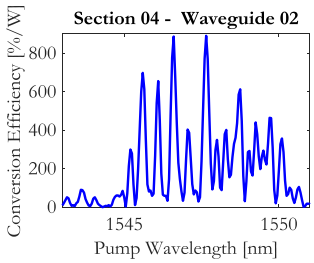

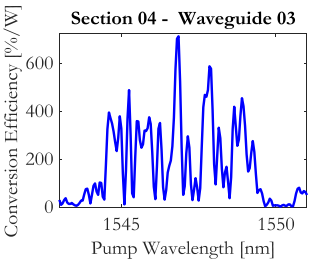

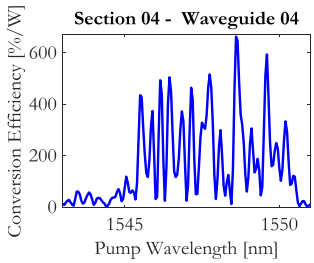

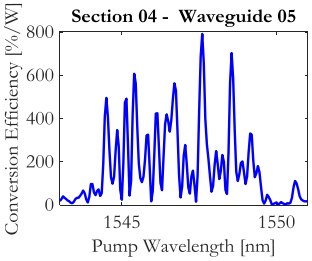

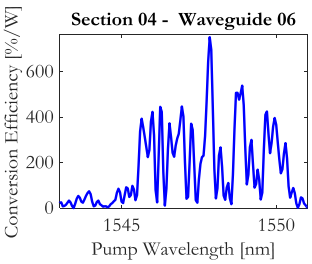

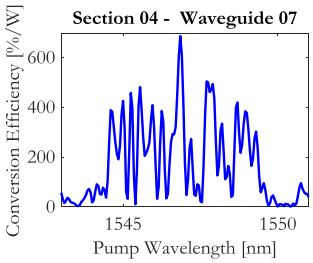

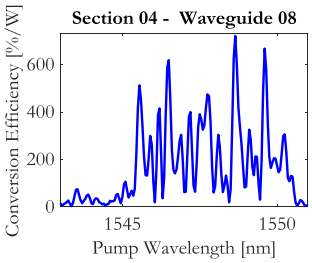

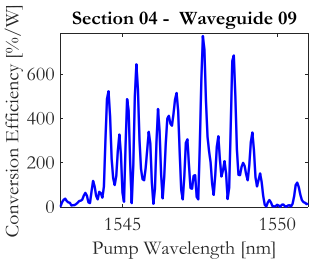

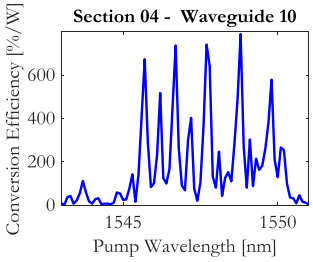

CHIP 4 – SECTION 5

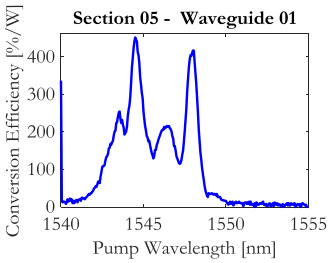

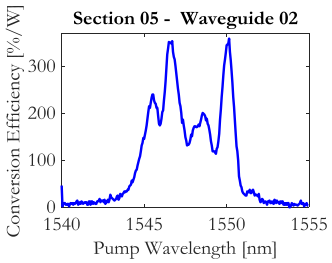

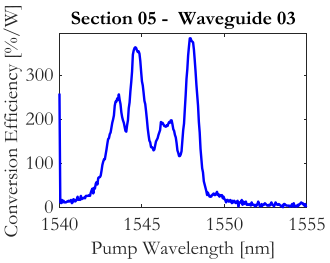

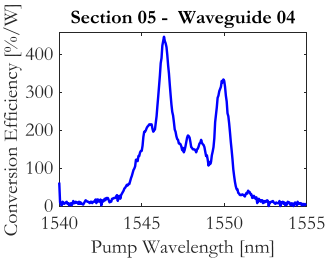

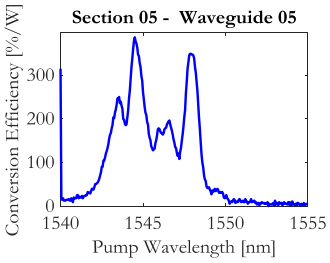

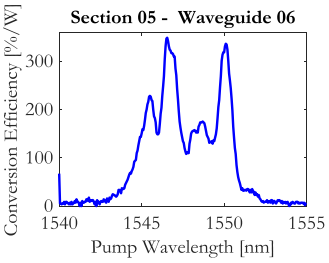

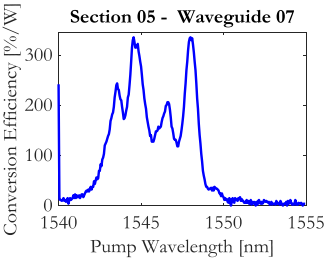

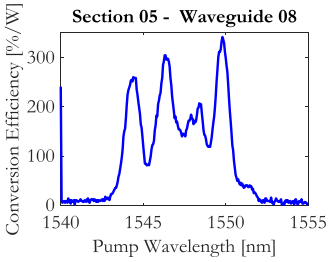

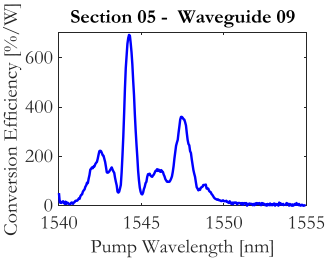

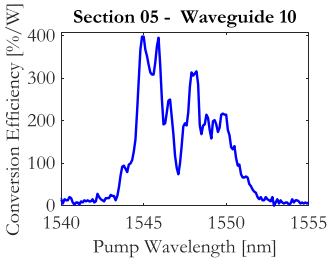

CHIP 6 – SECTION 1

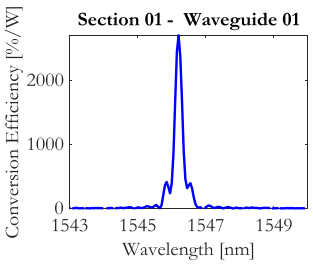

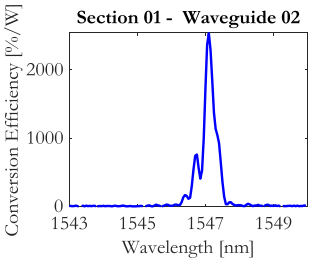

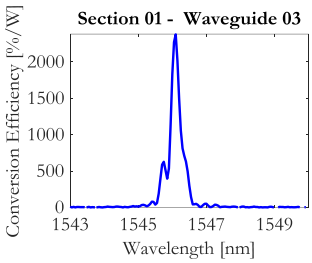

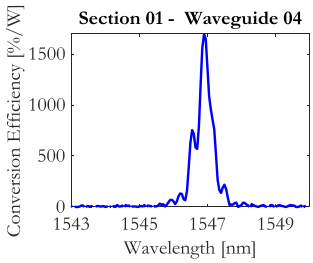

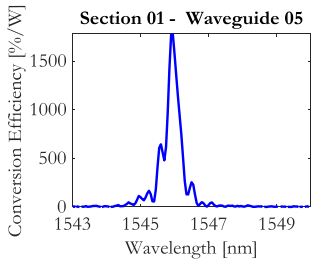

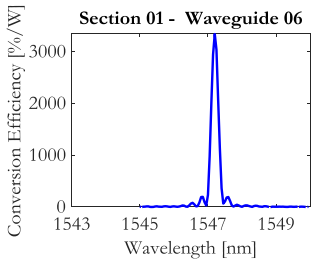

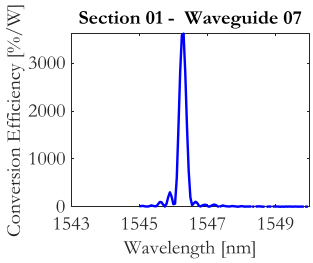

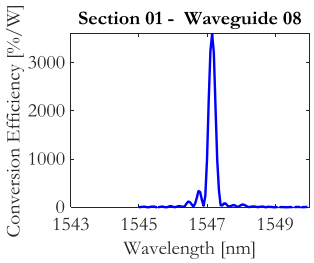

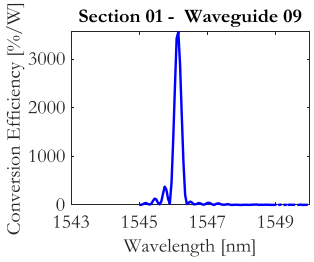

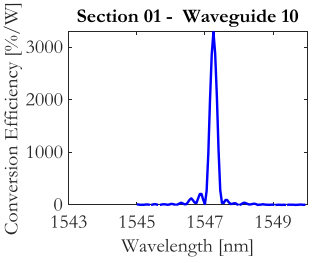

CHIP 6 – SECTION 2

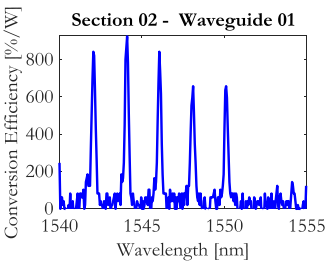

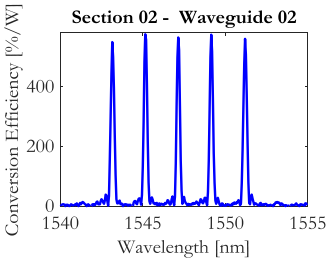

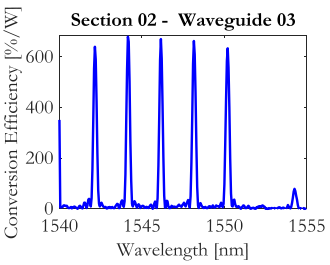

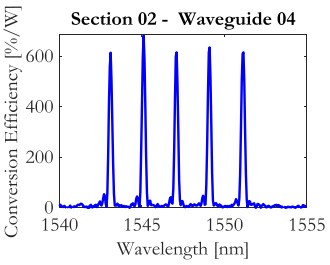

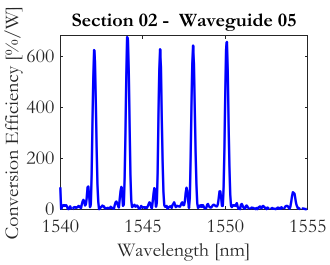

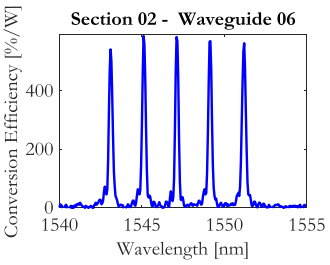

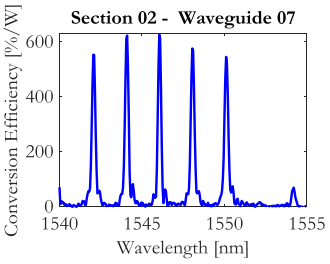

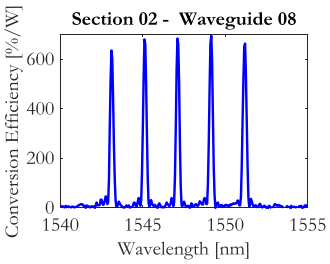

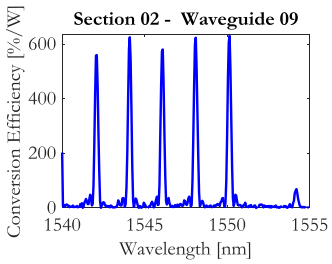

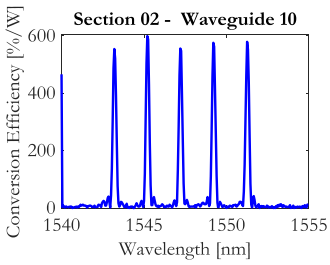

CHIP 6 – SECTION 3

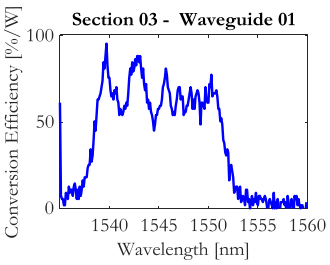

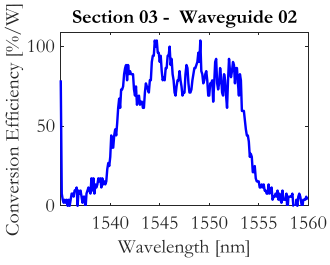

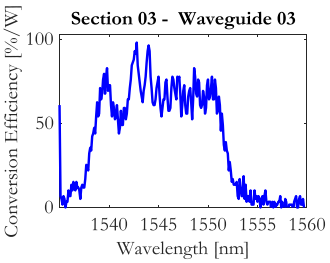

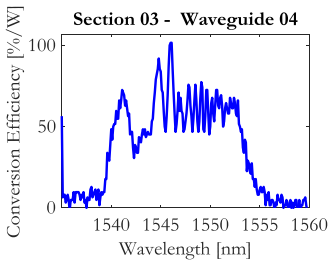

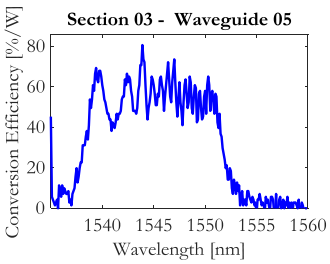

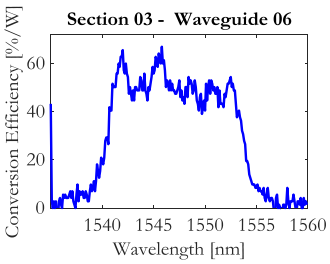

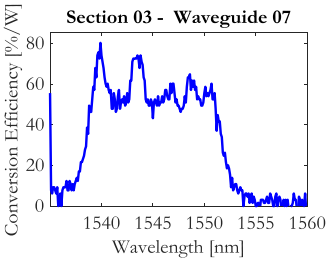

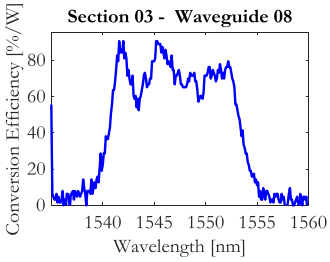

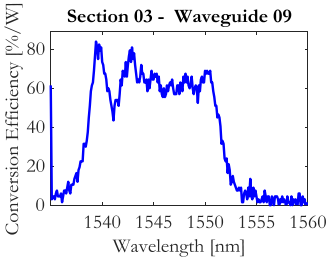

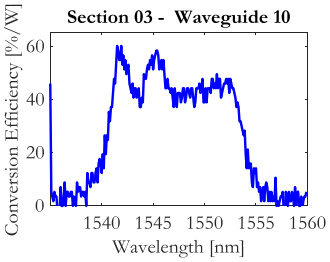

CHIP 6 – SECTION 4

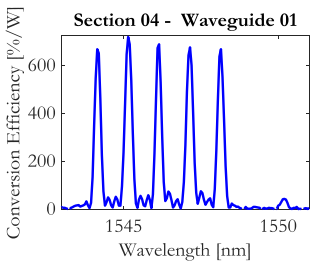

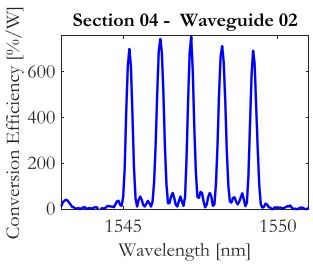

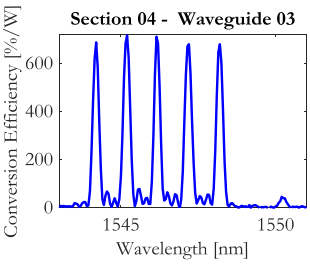

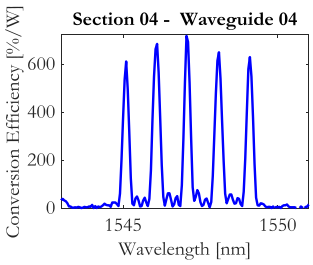

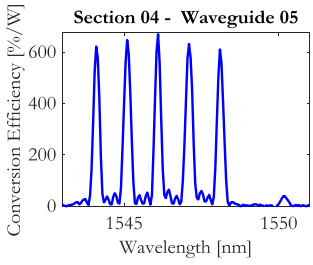

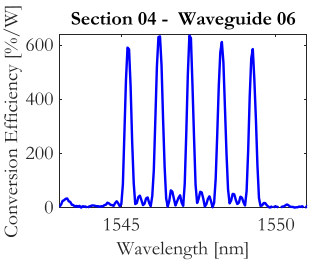

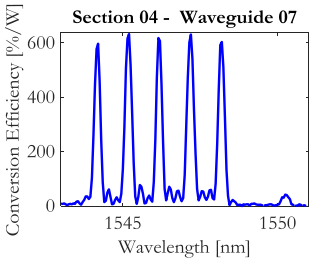

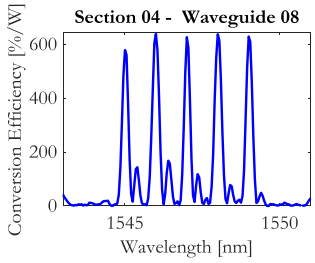

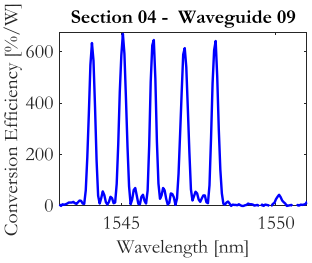

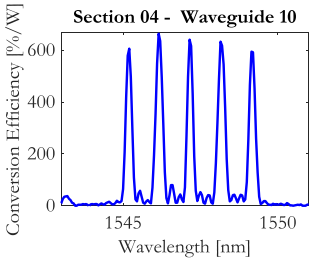

CHIP 6 – SECTION 5

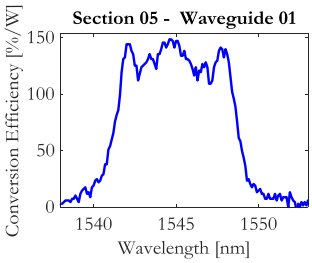

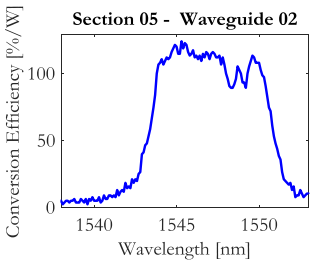

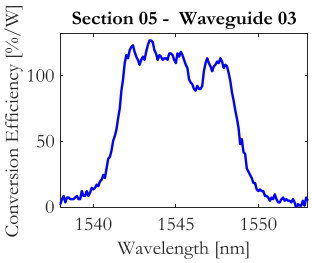

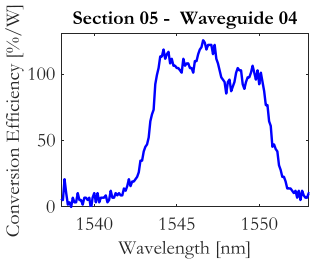

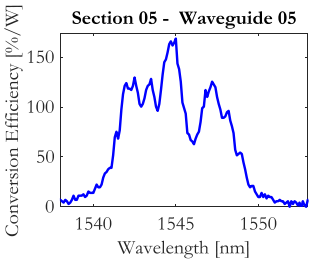

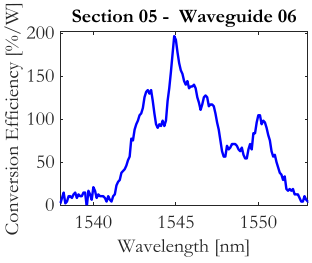

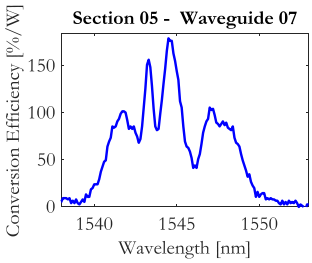

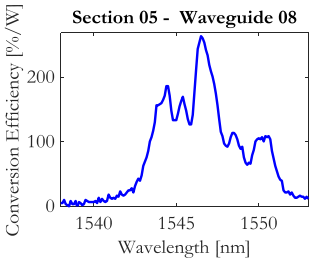

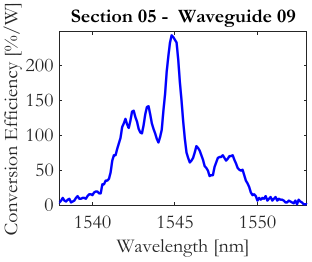

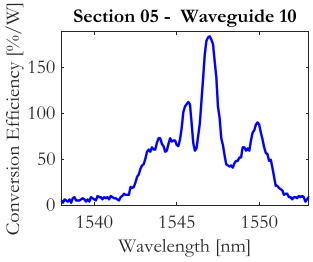

VITA

VITA

Ogaga D. Odele graduated with a B. S. in Electrical Engineering from Purdue University, West Lafayette, IN, USA in 2013. He is currently a Ph.D. candidate in the School of Electrical and Computer Engineering at Purdue University. His research interests include ultrafast optics, pulse shaping and signal processing of quantum states of light. Ogaga's work has led to his co-authorship of nine journal publications and several conference presentations. He has received a few notable recognitions in the course of his post-graduate career, including being selected as a Finalist in the Emil Wolf Outstanding Student Paper Competition (2014), and a 2nd place award in the Siegman International School on Lasers poster competition (2017). In addition to his research activities, Ogaga is a student member of The Optical Society (OSA) and currently serves as the vice-president of the Purdue student chapter of SPIE, the international society for optics and photonics.